o

PHOTOMETRIC AND POLARIMETRIC MAPPING OF WATER TURBIDITY AND WATER DEPTH

FINAL TECHNICAL REPORT

Prepared for

NATIONAL AERONAUTICS AND SPACE ADMINISTRATION
JOHNSON SPACE CENTER
EARTH OBSERVATION DIVISION
HOUSTON, TEXAS

UNDER CONTRACT NAS 9-12963

GRUMMAN

GRUMMAN AEROSPACE CORPORATION

BETHPAGE, N.Y.

PHOTOMETRIC AND POLARIMETRIC MAPPING

OF WATER TURBIDITY

AND WATER DEPTH

BY

JOHN HALAJIAN

AND

HERBERT HALLOCK

AUGUST, 1973

FINAL REPORT

NASA CONTRACT NAS9-12963

"I often say that when you can measure
what you are speaking about and express
it in numbers you know something about
it; but when you cannot measure it, when
you cannot express it in numbers, your
knowledge is of a meagre and unsatis-
factory kind: it may be the beginning
of knowledge, but you have scarcely, in
your thoughts, advanced to the stage of
science..."

Lord Kelvin

FOREWORD

This is the Final Report on the "Photometric and Polarimetric Mapping of Water Turbidity and Water Depth" for the National Aeronautics and Space Administration, Lyndon B. Johnson Space Center, Houston, Texas, under Contract NAS 9-12963 to the Grumman Aerospace Corporation, Bethpage, New York.

The study called for the development of quantitative data reduction techniques directed towards bathymetric and ecological investigation of coastal waters. It was conducted under the cognizance of the Applied Physics Branch, Earth Observation Office of NASA/JSC, with Dr. A. E. Potter as Technical Representative.

TABLE OF CONTENTS

v

TABLE OF CONTENTS (CONT'D)

LIST OF FIGURES

SUMMARY

A " Digital Photometric Mapper" (DPM) was used in the Fall of 1971 in an airborne survey of New York and Boston area waters to acquire photometric, spectral and polarimetric data. The object of this study is to analyze these data with quantitative computer processing techniques to assess the potential of the DPM in the measurement and regional mapping of water turbidity and depth. These techniques have been developed and an operational potential has been demonstrated.

The report discusses sensing requirements dictated by water physics; lays down the theoretical basis for analyzing photometric, spectral and polarimetric signatures of water; presents typical case studies, computer reduction of field data and results on water depth, surface roughness and sub-surface turbidity in numerical or graphical map forms; compares the results with available ground truth, and estimates accuracies achieved and those that potentially could be achieved.

Specific outputs include: a water depth and surface roughness map off Fire Island, N.Y.; surface and sub-surface turbidity profiles of Boston Harbor; and a turbidimetric map of Long Island Sound. It is shown that the DPM has a capability to resolve depth increments as small as one foot in 35 ft. of typical coastal water and water turbidity with an accuracy of better than one Jackson Unit.

More emphasis is placed at this time on the methodology of data acquisition, analysis and display than on the quantity of data. The results illustrate the type, quantity and format of information that could be generated operationally with a DPM-type sensor characterized by high photometric stability and fast, accurate digital output. The prototype, single-channel DPM is suggested as a unique research tool for a number of new applications. For the operational mapping of water turbidity and depth, the merits of a multi-channel DPM coupled with a laser system are stressed.

INTRODUCTION

This report deals with the quantitative refinement of airborne remote sensing techniques in the measurement and mapping of water related phenomena as originally introduced in a previous report entitled "Digital Photometric and Polarimetric Surveys of Water and Land Areas" (1). Its purpose is to evolve a practical approach to the problem of mapping the depth, turbidity and surface roughness of coastal waters. The primary sensor used in this investigation is the Grumman "Digital Photometric Mapper" (DPM). The DPM is a line-scanning imaging system designed for the precision measurement of optical signatures in computer-compatible form. (2)

The report begins with the descriptions of the sensor system, sensing techniques and data acquired over Boston and New York metropolitan waters aboard the Grumman Ecosystems A-26 sensor aircraft. This is followed with a theoretical analysis of the observed phenomena, and computer reduction of the data leading to information on water depth, sub-surface turbidity and surface roughness. Calculations of water depth are based on the spectrophotmetric approach in which differential attenuation of sunlight at various wavelengths reflected from the bottom is used as a measure of depth. Calculations of turbidity or water clarity, are based on several independent approaches including single-color (where depth is known), two-color and polarimetric measurements. Typical case studies are discussed based on semi-automated computer processing of the data. The results are displayed in graphical, pictorial or numerical map form and interpreted in terms of available ground truth information.

The report also includes a discussion of problem areas and sources of error encountered in this approach to remote sensing. Recommendations are made for an improved sensor system that would simplify the operations both in the air and on the computer, would be capable of achieving higher accuracy and be less dependent on airborne controls and ground truth measurement.

SENSOR SYSTEM AND SENSING TECHNIQUE

The sensor system used in this experiment consists of the Digital Photometric Mapper (DPM), a second non-scanning photometer boresighted to the DPM, and a Hasselblad camera used for tracking purposes.

The DPM is a calibrated, electro-optical scanner based on the image dissector television camera tube having an S-20 photosurface. It is used in a line scan mode along an axis perpendicular to the flight path while the forward motion of the aircraft generates the scan along the other axis as shown in Figure 1. During scan discrete measurements are made at a typical rate of 3000 per second, each being represented by an 8 bit recording (0 through 255). There are 226 elements per scan line, about 26 of which are used in "black level" reference at the beginning of each scan line for photometric stabilization. The measurements are accurate to within 1% under adequate illumination. This is actually better than can be done with most commercial laboratory instruments where each reading may require one minute or more. Because of the large number of accurate readings available at such short exposure, it becomes possible to screen out much of the environmental noise. By environmental noise we mean the effect of water surface features such as waves, swells and whitecaps.

The construction and the unique features of the DPM may best be described by referring to the block diagram in Figure 2.

(a) The image tube is the ITT 4011 Vidissector utilizing a .004 inch square aperture. This rather coarse resolution was chosen to optimize the aperture response and thus the photometric fidelity. The tube is provided with very low hysteresis deflection coils and and Netic-Conetic magnetic shielding.

(b) Both the sweep and the photometric output are digitized with control exercised by a common oscillator pulse generator whose stabilized rate can be varied over a range desirable for various conditions of use. The sweep circuitry includes a precision miniaturized D-A Converter, and the photometric output circuitry includes a comparable module of the A-D category, both having 8 bit capability.

(c) The input to the 8 bit D-A converter for sweep control is an 8 stage counter with an added fly-back pulse generator which is adjusted

to cause the counter to reset at the conclusion of 226 pulses. This number was chosen to suit the coverage of the tube photosurface by deflection of the aperture. Faceplate masking by opaque tape is used beyond 200 counts for reference black level.

(d) The coil driver amplifiers controlled by the D-A converter furnish deflection current in very linear proportion to the coils. The control is a "staircase" function providing about 1/3 millisecond of stationary "staring" photometry at each increment.

(e) The image dissector dynode high voltage power supply (1800 volts) is especially well regulated and is the base for a ten step gain control (0.1 to 1.0 full gain). This added control seemed to be necessary at the time of original design to cope with the dynamic range limitations of key components available at that time.

(f) The preamplifier is a low-noise dual FET circuit of excellent stability and good temperature characteristics.

(g) The output of the preamplifier and succeeding IC amplifiers is fed to a driven clamp which preserves the d.c. stability and photometric fidelity by clamping to ground level when triggered by the fly-back pulse once every sweep (approximately 1/15 sec interval).

(h) The output of the amplifier is furnished to a current integrator which functions by the controlled charging and discharging of the integrating capacitor. This integration proceeds for the exact interval of the sweep staircase element and is controlled by the regulatory master pulse generator. The output of the integrator is a series of pulses, the height of which represent the charged value of the capacitor in accurate proportion to the number of photoelectrons passing through the tube aperture during the sweep interval. A typical integrator output is shown in Figure 3.

(i) The photometric value digitizing is based upon conventional modular components involving a sample-and-hold system regulated by the master pulse generator. For each sweep interval an 8 bit binary number representing a radiance value is formed and recorded on 8 tracks of a 16 track digital tape recorder.

(j) The digital tape recorder is used to record the master control pulses,

the flyback pulses, selected counter stages of the sweep, and the output of accessories such as a digital time generator. The recording is NRZ (non-return-to-zero) which is the least susceptible to ambiguities derived from noise.

(k) The DPM was originally designed to be used in the focal plane of a 61-inch aperture f/13.5 telescope objective for mapping the optical properties of the lunar surface. When adapted for aircraft use it was fitted with a Super-Farron 76 mm EEL f/0.87 objective lens which is an excellent light collector of good resolution. Thus the signal-to-noise ratio is adequate down to luminous levels of a few foot lamberts. Spectral bandpass filters and polarizers of high optical quality have been used to cover the full aperture of this objective lens.

(l) Calibration in the aircraft is achieved by inserting a diffuse light source of good uniformity over the aperture. In the laboratory an even better controlled and measured diffuse source can be used for periodic calibration, including the recording of the scan line function. The scan line function represents the response function of the tube over a line on its face as modified by the characteristics of the lens, aperture control and optical filters. It is found necessary to record line functions for each operational combination.

A serious limitation of the DPM is its single channel configuration. This necessitates two or more flights over the same area in order to acquire imagery in more than one spectral band or polarization orientation. It is possible to accomplish simultaneous scanning of multi-component imagery but at the cost of a major redesign of the DPM. Instead, it was decided to resort to the simpler alternative of supplementing the existing DPM with a fixed, non-scanning photometer which would secure simultaneously a trace along the centerline of the swath scanned by the DPM. The optical signatures of water are not as varied as those of land areas. Therefore, the combination of one scanning head which generates a matrix of data points, and a non-scanning head (NSH) (which generates one line of data points down the center of the matrix) would be adequate. These data would represent a calibration of the remainder of the data in the complete swath so that one could finally generate a map.

The second head consists of a phototube with an S-20 photosurface, lens, filter holder and supporting electronics. Its signals are recorded digitally on one of the 26 elements of the DPM scan line reserved for dark level reference. As shown in Fig. 2 an electronic switch is used to record the data from both sensors on the same digital magnetic tape. The installation of the sensor system on the Grumman Ecosystem A-26 Survey Aircraft is shown in Fig. 4.

Polarizing filters and numerous spectral bandpass filters are used in both heads in a complementary fashion in order to generate simultaneous H and V polarimetric data or two-color photometric data. The spectral response functions of the S-20 image tube with and without spectral filters are shown in Fig. 5.

These improvements are not the state-of-the-art ultimate in operational efficiency but they are a practical intermediate step for generating optical signatures in the field in order to determine whether there is an advantage in pushing further the DPM approach to remote sensing in which tonal accuracy and computer-compatibility are stressed.
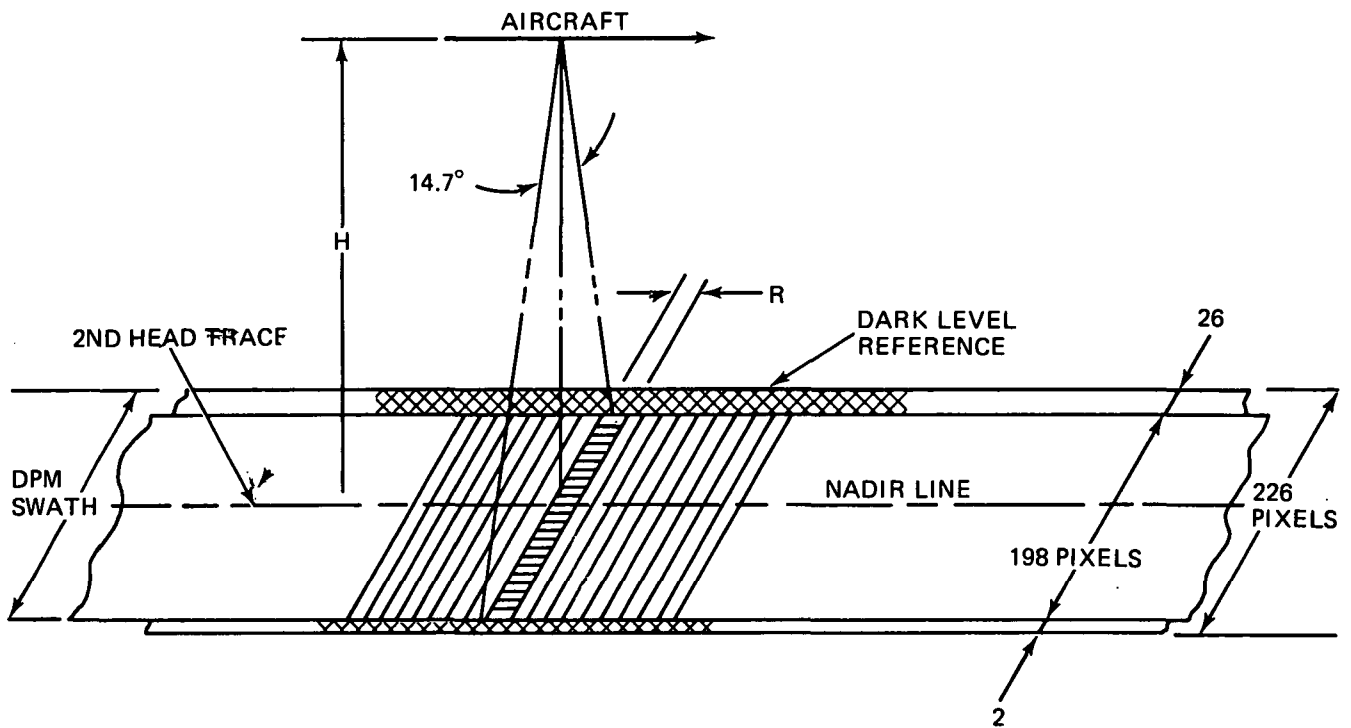
Fig. 1 Aircraft — Imagery Geometry
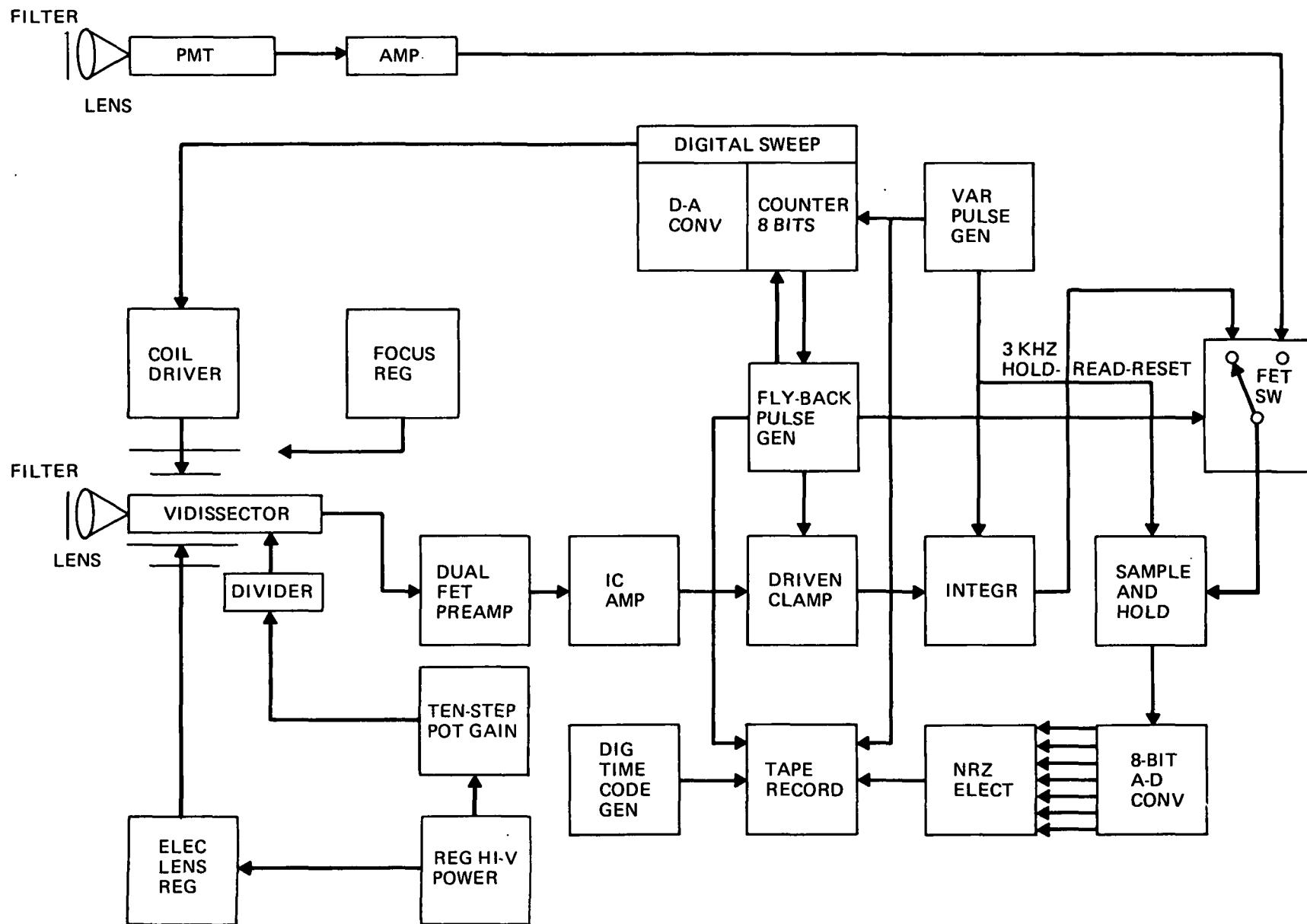
Fig. 2 Digital Photometric Mapper and Non-Scanning Head Schematic Diagram

CLAMPED VALUE
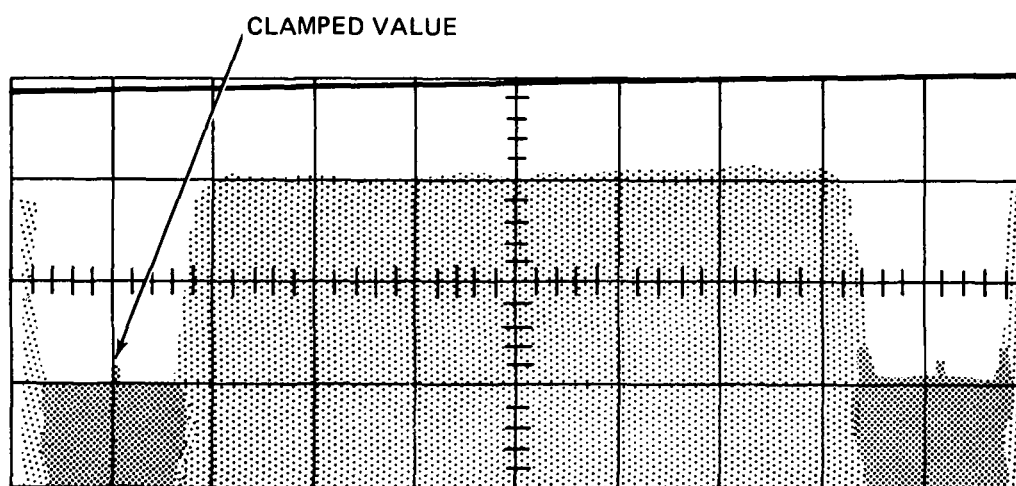
Fig. 3 Typical Integrator Output
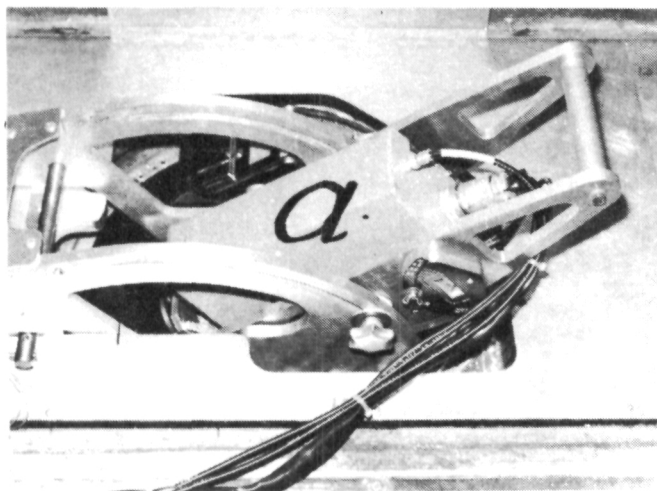
a DPM
b 2ND HEAD (NSH)
c TRACKING CAMERA
d TAPE RECORDER
e ELECT. CONSOLE
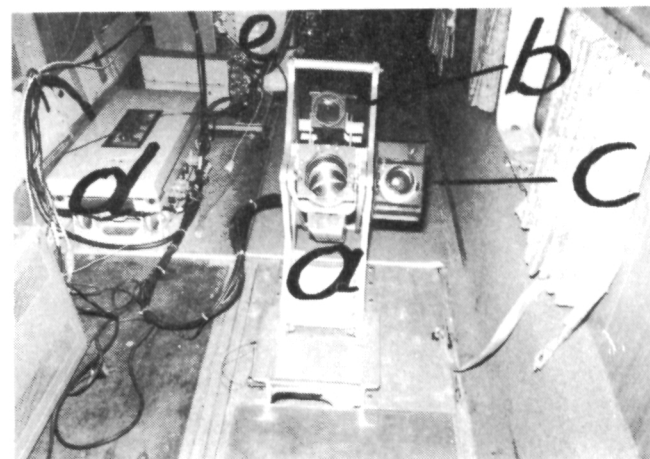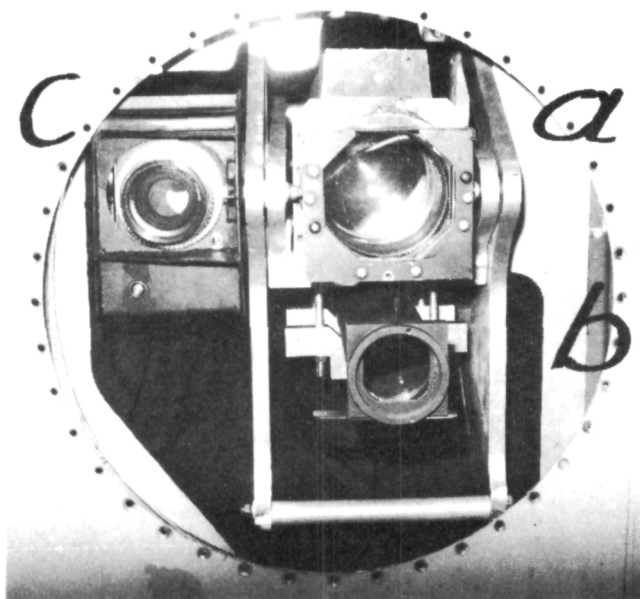
Fig. 4 Sensor System Installation on Grumman Ecosystems A-26 Sensor Aircraft
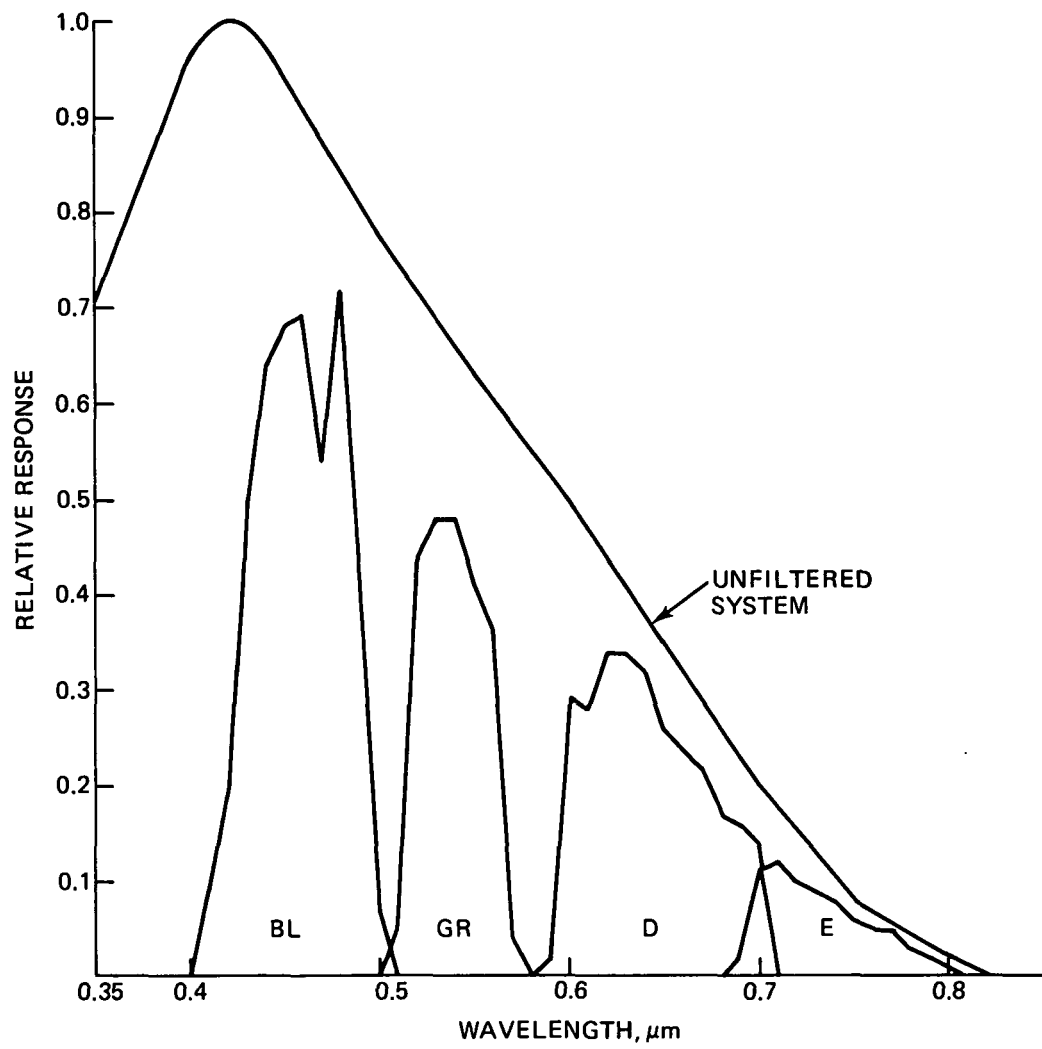
Fig. 5 Spectral Response Functions of DPM With and Without Color Filters

THEORETICAL ANALYSIS

1. Introduction

An accurate photometer-polarimeter for aerial survey of water areas has been described. This device makes it possible to examine the reflected sunlight quantitatively and to record the data in digital computer-compatible form. However, the data does not represent the influence of one isolated factor, but rather the integration of the effects of many complex factors such as bottom reflectance, water reflectance, reflectance by particulates, sky reflectance, water attenuation, turbidity-induced attenuation, polarization, etc. The interpretation is so complex that no single adequate reference has been found in the literature, although many valuable separate contributions are used from various sources. Therefore, it has been necessary to devote a considerable portion of this report to theoretical analysis and to the evolution of the analytic techniques we shall apply. The theoretical treatment is but introductory in nature since there are large gaps in theoretical and practical background for the best analysis possible. However, a unification of various points of view is attempted.

In the second part of this section we begin our treatment of the subject by describing a rather simplified multi-color photometric water depth model. Assumption of uniform water properties is made which, although usually unrealistic, presents a picture of the water-depth-by-attenuation approach which can be readily grasped.

In the third part a unification of the various concepts is presented in the form of more general equations relating the various factors. As far as turbidity-induced radiance is concerned, however, this part treats the so-called single-scatter albedo.

In the fourth part an attempt is made to introduce the effects of anomalous water parameters for a more realistic analysis of the complex areas. These anomalies include variations in water transparency, bottom reflectance, and turbidity-induced reflectance.

In the fifth part the theory is modified to include recent models (or theories) for multiple scatter treatment of turbidity-induced radiance. This is shown to be most probably the best approach to accurately evaluate effluents and areas of high turbidity.

Finally a polarimetric turbidity model is discussed based upon reference 1, and including the multiple scatter photometric model in an attempt to relate polarimetric signature to turbidity in Jackson Units.

2. The Multi-Color Photometric Water Depth Model

Determination of the thickness of a uniform medium through which radiation is transmitted can be made by measuring the attenuation and applying known mathematical expressions of the attenuation law. Using this principle the depth of water covering a sunlight-reflecting bottom can be measured remotely by accurate photometric survey of the area of interest. The radiance of the water may be dominated by the reflection of sunlight from the bottom if the water is shallow, but is negligibly influenced by the bottom reflection at large depths. There remains a substantial radiance at large depths which is made up of various surface and sub-surface light-scattering combinations by the water. For an evaluation of the attenuation approach it is usually assumed that the radiance at large depths is present also, as a constant value, added to the bottom reflection at shallow depths. This assumption may be questioned for very shallow depths, but experience can be cited to show that it may be a practical approach.

Mathematically the situation may be expressed as follows:

$$N = N_b + K \qquad . \qquad (1)$$

Where N is the total radiance observed, N_b is that part of the radiance contributed by the bottom reflection and K is a constant.

The attenuation law for transmission of monochromatic light through water may be applied to the case by noting that vertically incident sunlight is attenuated by passage through twice the water depth, d, if the photometric survey is conducted by vertical observation. In the process of transmission various reflectance factors are brought to bear upon the incident sunlight of flux density, H_s, including that of the bottom which directly affects the bottom signature. Other reflectance factors at the water surface contribute losses of signature value. Of course the reflections such as by particulate matter and molecules which contribute background have been lumped together in the radiance value, K, which is considered constant.

If the reflectance factor affecting bottom signature itself is called ρ_b,

the attenuation law may be expressed as follows:

$$N_b = (1 - \rho_w) H_s \rho_b e^{-2d(\alpha + \beta)} . \qquad (2)$$

$(\alpha + \beta)$ is the sum of absorption and scattering attenuation coefficients which may be called the extinction coefficient, or the volume attenuation coefficient. ρ_w is the reflectance factor of the water surface which varies with geometric factors, but is rather constant for a set of data.

When the total radiometric signature, N is examined, it consists of N_b + K. To calculate the depth, d, for any one small radiometrically surveyed area one must know the values of ρ_w, Hs, ρ_b, $(\alpha + \beta)$ and K. The value of Hs, can be measured from an airborne platform, and the value of K can be determined quite closely by measuring deep-water radiance, if available farther from the shore line. The values of $(\alpha + \beta)$ and (ρ_b), however, involve physical characteristics which depend upon local conditions of "ground truth". ρ_w can be calculated for smooth water.

However, it has been shown (4) that it is possible to derive reasonably accurate depth from airborne observations only, using multi-color photometry. As described in Appendix A and shown in Figure 6, the coefficient $(\alpha + \beta)$ varies with wavelength and with turbidity. If measurements are made over spectral bands, for example, in the green, and in the red portions of the visual spectrum, values of N in the green which may be called G, and values of K which may be called K_G will be obtained. Likewise analogous values in the red may be called R and K_R. Using subscripts, 1, 2, etc to designate depths d_1, d_2, etc. the attenuation equations can be applied to each set of values. In common logarithmic form, designating bottom reflectances in the green and red as ρ_{bG} and ρ_{bR} respectively,

$$\log (G_1 - K_G) = \log \left[\left(1-\rho_w\right) H_s \rho_{bG} \right] - 2d (\alpha + \beta)_G \qquad (3)$$

$$\log (R_1 - K_R) = \log \left[\left(1-\rho_w\right) H_s \rho_{bR} \right] - 2d (\alpha + \beta)_R \qquad (4)$$

This two-color photometry can be extended to three-color (or multicolor) photometry by use of additional band (s). The essence of the multicolor photometric approach is to deduce values of the important parameters such as $(\alpha + \beta)_G$ and $(\alpha + \beta)_R$ which will yield the same values of d_1, d_2, etc. from each equation. Since obviously these values are unique, systematizing this process involves the use of empirical data based upon the relationships between $(\alpha + \beta)_R$, and $(\alpha + \beta)_G$ for example at various degrees of turbidity. Using data typified by Figure 6, Figure 7 has been prepared showing a relationship between the volume attenuation coefficients $(\alpha + \beta)_G$ and $(\alpha + \beta)_R$ and the ratio of these values, namely $\dfrac{(\alpha + \beta)_R}{(\alpha + \beta)_G}$ which we define as the coefficient ratio, $\gamma_{R/G}$. The procedure is covered in Appendix D.

If equations are set up between areas 1 and 2, which can be assumed to have the same reflectance properties, $\log\left[(1-\rho_w) H_s \rho_b\right]$ can be eliminated to leave relationships such as the following:

$$\log \frac{R_1 - K_R}{R_2 - K_R} = 2\,(d_2 - d_1)\,(\alpha + \beta)_R \qquad (5)$$

and

$$\log \frac{G_1 - K_G}{G_2 - K_G} = 2\,(d_2 - d_1)\,(\alpha + \beta)_G \qquad (6)$$

Of course it follows that the ratio $\gamma R/G$ between red and green absorption coefficients can be expressed as follows:

$$\gamma\,R/G = \frac{(\alpha + \beta)_R}{(\alpha + \beta)_G} = \frac{\log \dfrac{R_1 - K_R}{R_2 - K_R}}{\log \dfrac{G_1 - K_G}{G_2 - K_G}} \qquad (7)$$

A typical case of survey would include data taken normal to a shoreline with increasing depth values d_1, d_2, d_3 etc. farther from the shore. By plotting the values $\log (G - K_G)$ and $\log (R - K_R)$ vs. distance from shore it is possible to ascertain $\gamma_{R/G}$ values from the slope ratios of the red profile to the green profile.

The accuracy with which $\gamma_{R/G}$ can be determined depends upon the accuracy of the input data. It is very important to use an observational device with a

high degree of photometric accuracy. If the observations are made over rough water it is also very important to smooth out the surface wave effects. Also it is important to avoid the confusion caused by changes in water transparency (turbidity-induced) between the points analyzed. Again it also has to be remembered that the derivation was based upon the assumption of spatially uniform bottom reflectance (although not uniform between colors). Reference (4) describes a rather elaborate graphical analysis by which the symptoms of various anomalous conditions can be recognized for the purpose of making allowances. The computerization of much of this diagnosis is probably possible, if necessary.

Another mathematical generalization about accuracy can be made from the shape of the curve shown in Figure 7. It is obviously advantageous to work on a portion of the curve where the slope, $(\alpha + \beta)/\gamma$ is at a minimum for large values of γ (i.e. for the clearest water). This slope is also considerably less in the far red (FR), centered, for example, at 6800 A than in the middle red (R), centered at about 6300 A. Use of the γ ratio to determine $(\alpha + \beta)$ is more accurate where the ratio between far red (FR) and green (G) is used instead of the ratio between R and G. As indicated in Figure (8) it is still better to use the FR to R ratio for anomalous conditions in spite of steeper slope.

These generalizations are but a somewhat more quantitative expression of the observation made in ref 5 (page 667) that the use of the .60 or .65 μm bands in a multispectral scanner resulted in constant relative attenuation over large changes in water depth. In other words the results are less ambiguous in the red than in the lesser wavelengths because the anomalies created by turbidity changes are less.

However, the penetration achievable in clear water is much better in the green part of the spectrum than in the red. In terms of a depth profile extending from a shore line out into deep water, the penetration achieved in the red is adequate, and the accuracy is excellent near the shoreline where the transparency is apt to be poor, or anomalous by reason of turbidity. In the very shallow regions an FR/R ratio will enable the least ambiguous determination of $(\alpha + \beta)_R$ and $(\alpha + \beta)_{FR}$ and the best accuracy in the ultimate water depth calibration of scale. For the deeper and clearer water it is necessary to use the $(\alpha + \beta)_R/(\alpha + \beta)_G$ ratio which should facilitate determination of $(\alpha + \beta)_R$ and $(\alpha + \beta)_G$ where the γ-ratio is greater than 2, for example.

Noting that the exponent in equation (2) is the product $2(\alpha + \beta)d$, it is clear that for a given empirically determined product value, if the numerical value of $(\alpha + \beta)$ is assumed to be 20% too high the value of d computed will be $\frac{1}{1.2}$ x 100 or 83% of true depth. There are many other factors which affect accuracy, but this sometimes major uncertainty sets an obvious limit on the fidelity without use of some other means of scale calibration.

Looking at very shallow water FR/R relationships it seems conceivable that 5% accuracy could be obtained. Then if these shallow water data (at the deepest practical level) were used for calibrating the R/G relationship for water down to, let us say, 50 ft., it appears possible that something like 10% might be achieved. This approach can be called three-color photometry.

The reliability of the method also depends upon knowing the relationships such as illustrated in Figure 8 quite accurately. Presumably the relationship between turbidity and spectral attenuation coefficients depends on the nature of the particulate matter which is responsible for the turbidity. Consequently the data represented by Figure 8 may not represent the case for the Long Island coastal areas with the utmost fidelity. Local data on spectral attenuation would be preferable. In many treatments of approach, such, for example, as ref 5, it has been assumed that a certain amount of "ground truth" data could be acquired for the purpose of calibrating the airborne data. The best input for calibration might be some "control point" depth measurements (e.g. by water-borne fathometer). Another valuable input would be transparency measurements made by actual water sampling, as by the electronic Secchi disk or turbidimeter. Transparency readings can readily be converted to $(\alpha + \beta)$ values.

One of the most intriguing, and potentially most practical calibration methods would consist in the use of a laser rangefinder or depth sounder from the same aircraft platform. This is suggested in references (5), (6) and (7). It is also the principal subject of the NRL-NAVOCEANO program PLADS (Pulsed Light Airborne Depth Sounder) (8).

Throughout this discussion it has been assumed for the purpose of simplifying the expressions that sunlight was incident vertically on the water and that the viewing geometry was normal to the water. If these conditions are not met and sunlight is incident at an angle θ from the vertical becoming an angle θ'

by refraction, while the viewing is at an angle ϕ from the normal (ϕ' before refraction by the water) then the distance traversed by sunlight is theoretically d ($\sec\theta' + \sec\phi'$). However, the light scattering at, and below the surface of natural bodies of water tends to reduce the value of ($\sec\theta' + \sec\phi'$) toward the value of 2. We shall replace d ($\sec\theta' + \sec\phi'$) by the expression 2 d f where f is a factor slightly in excess of unity, realistically representing the apparent multiplication of true depth due to geometry. Hereafter, the factor f will be understood to be included in all appropriate equations.

The transport of bottom material due to water dynamics tends to assure a reasonably constant value of ρ_b in beach areas. However, in other areas of shallow water it is quite possible to encounter substantial changes of reflectance of the bottom within an area of interest. The effect of such a change from station 1 to a station 2 of greater depth may be expressed in terms of a modification of equations (5) and (6) as follows:

$$\log \frac{G_1 - K_G}{G_2 - K_G} = 2f\,(d_2 - d_1)\,(\alpha + \beta)_G + \log \frac{\rho_{bG_1}}{\rho_b G_2} \qquad (8)$$

$$\log \frac{R_1 - K_R}{R_2 - K_R} = 2f\,(d_2 - d_1)\,(\alpha + \beta)_R + \log \frac{\rho_{bR_1}}{\rho_b R_2} \qquad (9)$$

in which ρ_{bG_1} and ρ_{bR_1} refer to bottom reflectances in the green and red, respectively, at station 1. Subscripts 1 and 2 refer to stations 1 and 2. Constancy of K_G, K_R, $(\alpha + \beta)_R$ and H_s are assumed.

Thus it is seen that a change in bottom reflectance will create a change in the slope of $\log (G-K_G)$, or $\log (R-K_R)$ plotted against distance from shore. Unfortunately changes in some other of the presumed "constants" may have a somewhat similar effect.
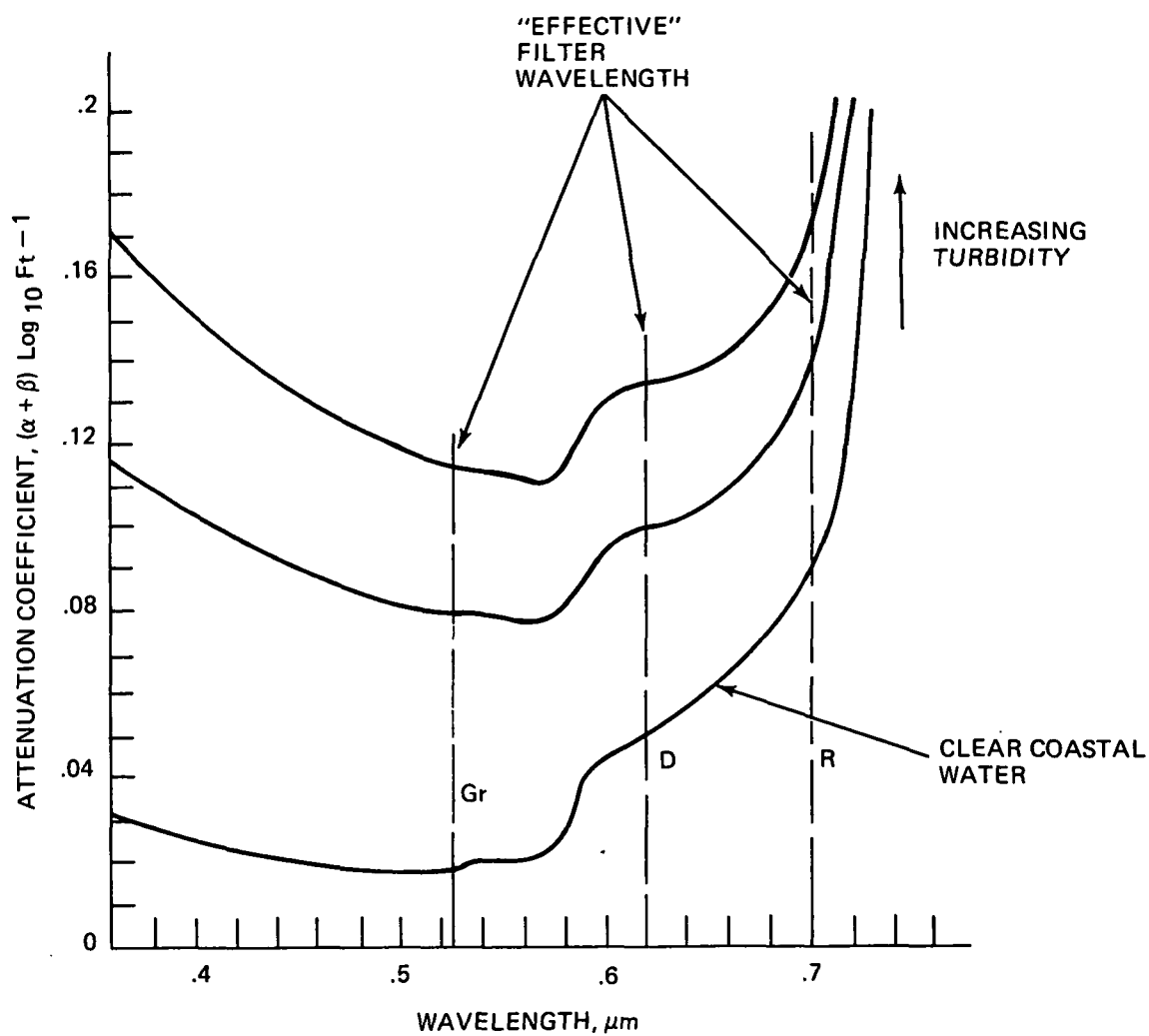
Fig. 6 Spectral and Turbidity Dependence of Extinction Coefficient
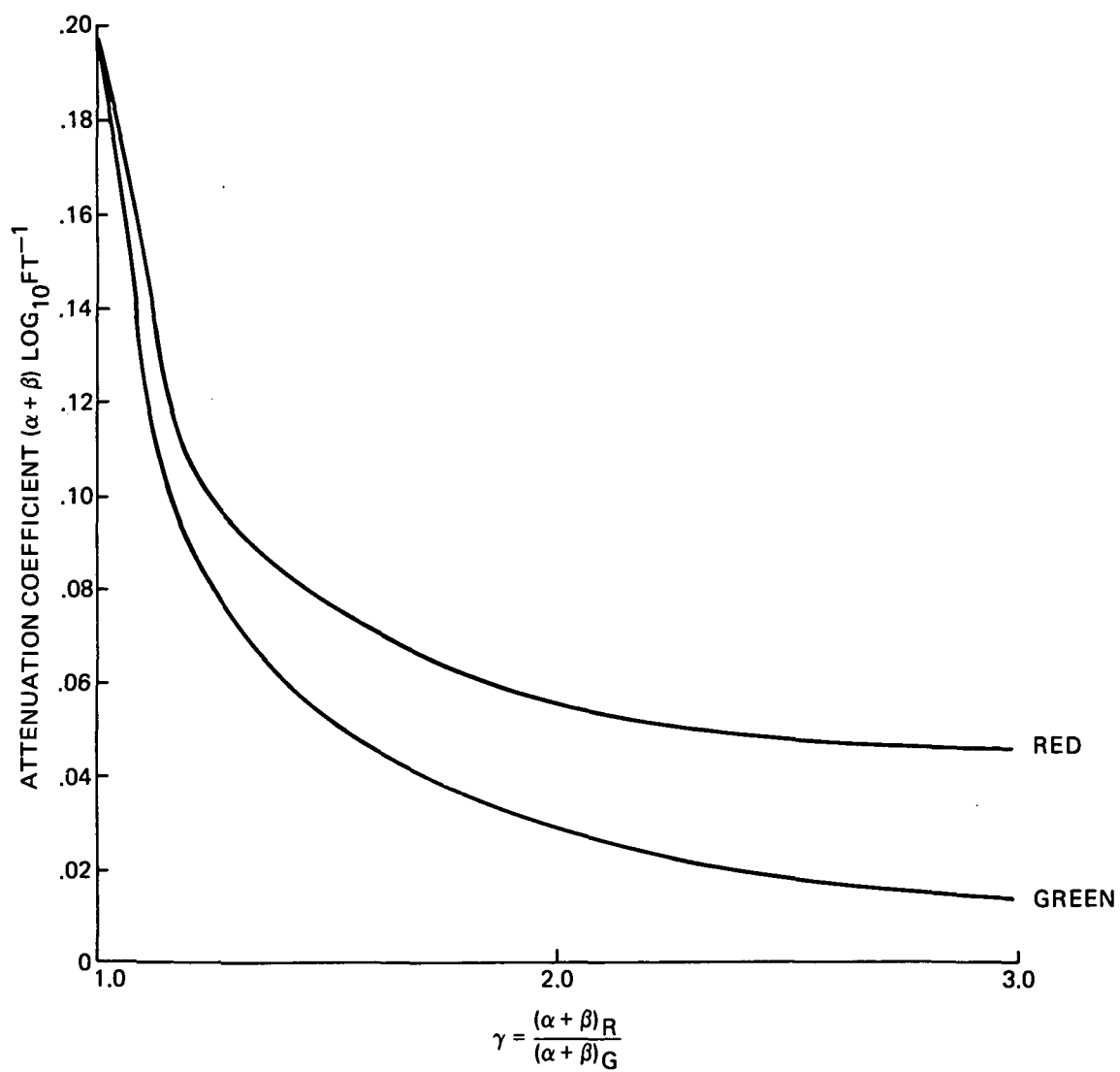
Fig. 7 $(\alpha + \beta)$ as a Function of γ for Shallow Water (10 Ft Depth)
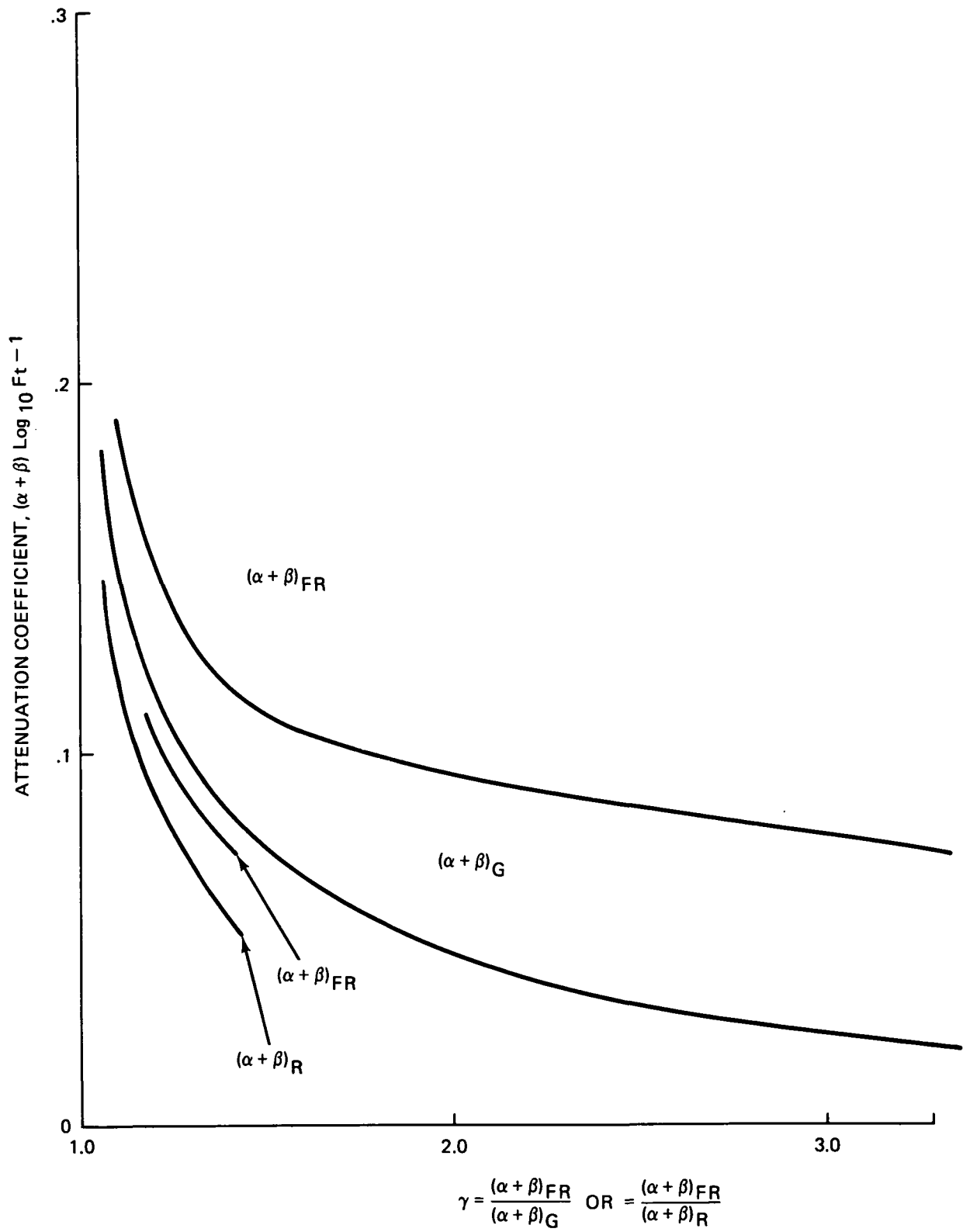
Fig. 8 $(\alpha + \beta)$ As a Function of γ for Shallow Water (10 Ft Water) Using FR (Far Red) (6800A) Data

3. More General Formulation For Water Depth

And Turbidity

The optical signature of water in sunlight is the summation of some very complex phenomena including, as will be discussed in another section of this report, the polarimetric aspect. So far we have discussed a much simplified version of this signature appropriate for preliminary analysis of water depth mapping in the less turbid waters. This signature is dominated by reflection of the bottom in shallow depths. Without going to the ultimate mathematical expression, it is, nevertheless, desirable to examine a more complete formulation of the signature which will include allowance for anomalous turbidity.

The complete signature can be considered as being made up of a number of parts, some of which are functions of water depth and others not. For example the radiance of the water in sunlight, called G in the green, R in the red, etc. may be expressed as follows:

$$G = \phi_G (h) \left[g_b (d) + g_u (d) + g_{sp} + g_{rsk} \right] + g_a (h) \quad (10)$$

$$R = \phi_R (h) \left[r_b (d) + r_u (d) + r_{sp} + r_{rsk} \right] + r_a (h) \quad (11)$$

g_b, the signature component resulting from reflection of the bottom, is a function of depth (d).

g_u, the component due to backscattering from sub-surface molecules and particles, is actually a function of depth, although the previous section of this report assumed that this variation is negligible compared to factors much larger for relatively clear shallow water.

g_{sp}, the component due to back-scattering from surface particles, is the diffuse rather than specular portion of surface reflection that assumes importance for scum, or shallow-depth layers of buoyant particulates in the water.

g_{rsk}, the component due to specular reflection of the sky (at times including the sun) is an important factor which is not depth-dependent.

g_a, the component due to backscattering from the atmosphere, is not water signature, but appears in any observation from an airborne platform. It is a function of the altitude, h, of observation.

ϕ_R and ϕ_G are atmospheric attenuation factors which are functions of the altitude, h, of observation. The proper treatment of these factors, as well as g_a and r_a is a complex subject by itself, and is deserving of very careful consideration for the high altitude case. In order to bring out the principal features of the water variables it is elected to assume that ϕ_G, ϕ_R, g_a and r_a are constants for the time of surveillance which is justifiable for low altitude observation in clear weather. In the calculation of radiance ratios between elemental areas the values of ϕ_G and ϕ_R tend to cancel out, and the effects of g_a and r_a for any one set of observations may be considered to be absorbed into a "deep-water" radiance constant.

The deep-water radiance constants have been called K_G and K_R previously. The N of equation (1) can be considered to be equal to G/ϕ_G, R/ϕ_R, etc., depending on the spectral band.

Therefore,

$$K_G = g_u + g_{sp} + g_{rsk} + g_a/\phi_G \qquad (12)$$

$$K_R = r_u + r_{sp} + r_{rsk} + r_a/\phi_R \qquad (13)$$

In which g_u and r_u are not considered depth-dependent and are constant over the area of water being surveyed.

An assumption of constancy for these terms must first of all be based on an assumption of constancy in the value of H_s, the solar irradiance. Each of the terms, such as g_u. can be considered to be the product of H_s and an effective reflectance factor, let us say ρ_{uG} for g_u, and possibly a factor including water surface reflectance which is not necessarily the same for all terms.

Thus
$$g_u = H_s \, \rho_{uG} \, (1-\rho_w)$$

$$g_{sp} = H_s \, \rho_{spG}$$

$$g_{rsk} = H_s \, \rho_{sk} \, \rho'_w$$

$$g_a = H_s \, \rho_{aG}$$

ρ_w and ρ'_w are two water reflectance factors which differ because of geometric factors. It should be remembered also that equation (2) shows that g_b

(or N_b) is proportional also to H_s. If we are fortunate enough to have a really constant value of solar irradiance throughout the few minutes required for a set of observations, the exact value of H_s does not affect our comparisons of elemental areas 1, 2, 3 etc. However, if by reason of cloud shadows there is a variation, then adjustment, or normalization for sunlight fluctuations must be made.

H_s is the value of solar irradiance at the water surface. ρ_{sk} is a factor by which this must be multiplied to yield sky radiance. Unfortunately H_s may itself be a function of ρ_{sk}. Therefore, if H_s does change, the value of g_{rsk} may not change in linear proportion.

Neglecting solar irradiance fluctuations an examination of the terms of equation (12) for physical basis of constancy indicates that the last two terms $\left(g_{rsk} \text{ and } \dfrac{g_a}{\overline{\phi}_g} \right)$ are quite unlikely to exhibit change during a few minutes of time and over a few miles of flight. Even these terms, however, are variable from hour to hour.

The first two terms of each of equations (12) and (13) involve physical quantities which can be associated with anomalous contamination, particularly the turbidity of effluents or discharges into water. Also we may include within these quantities the effects of whitecaps and breaker phenomena in surf. Occasionally there is a disturbance of the water bottom by water dynamics which is sufficiently large to affect g_u through muddiness. These effects are bothersome with respect to photometric measurement of water depth, and, for the most part, must be screened out of the data before computing depth profiles. However, these same anomalous values are frequently the potential source of information on water quality parameters such as turbidity.

In using the solar irradiance value, H_s, we have not distinguished between direct solar irradiance and indirect irradiance from sky-light which is scattered solar flux. The distinction is of secondary importance for most of our treatment and will be ignored, but it is recognized that conditions such as high altitude demand recognition of this physical effect.

It is conceivable that differentiation between g_u and g_{sp} might be accom-

plished by polarimetric means, but for the present discussion it will be assumed that a purely photometric assessment of effluents will not separate them. Therefore the sum of g_u and g_{sp}, in which g_u will usually predominate, will be considered the photometric evidence of "apparent turbidity". It is convenient to consider the sum, $\left(g_{rsk} + \dfrac{g_a}{\phi_G} \right)$ to be represented by a constant, K_G', a temporal

and spatial invariant over the "few minutes and few miles" of airborne measurement. For low altitude observation in clear weather K_G' is comprised chiefly of the value of g_{rsk}.

Equations (10) and (11), slightly modified in form to show resulting net radiance or N-values, and variable turbidity, but constant sky and atmospheric conditions yield the following expressions:

$$N_G = \frac{G}{\phi_G} = g_b (d) + K_G' + \left[g_u (d) + g_{sp} \right] \qquad (14)$$

$$N_R = \frac{R}{\phi_R} = r_b (d) + K_G' + \left[r_u (d) + r_{sp} \right] \qquad (15)$$

If bottom signature is appreciable in the effluent it must be accounted for in arriving at value of $\left[g_u (d) + g_{sp} \right]$, for example, from measured values such as N_G. Usually a strong effluent signature will overwhelm the bottom signature so that $g_b (d)$ and $r_b (d)$ can be neglected. Under these likely conditions, then:

$$g_u (d) + g_{sp} = N_G - K_G' \qquad (16)$$

$$r_u (d) + r_{sp} = N_R - K_R' \qquad (17)$$

As has been pointed out, K_G' and K_R' are chiefly reflected sky radiances for low altitude observation and can be calculated fairly accurately from measured sky radiance values.

If a way can be found to relate net photometric values (e.g. $N_R - K_R'$) to turbidity values in Jackson Units, then it would be possible to convert the results of photometric survey into a turbidity map. More will be said about the physical model for this translation in later discussion. However, one of the

simpler approaches is to assume that the turbidity-induced radiance is directly proportional to the single scatter albedo (9) which may be represented by the symbol, $\widetilde{\omega}_o$. This quantity is defined as follows:

$$\widetilde{\omega}_o = \frac{\beta}{\alpha + \beta}$$ (18)

To further simplify the introduction of this quantity another assumption will be made that the scattering coefficient, β, is entirely attributable to the particulate content. This assumption is reasonable in the red end of the spectrum where the influence of molecular scattering is at a minimum as can be seen in Figure 9 taken from Feinstein and Piech (11). Using the value of .035 $\log_{10}$ ft $^{-1}$ for the absorption coefficient of pure water in the red,

$$\widetilde{\omega}_o = \frac{\beta_R}{.035 + \beta_R}$$ (19)

where β_R is the scattering coefficient in the red. For clear coastal water it may be assumed that $(\alpha + \beta)_R = .049$ and that the turbidity is 1.0 Jackson Unit. Then

$$\widetilde{\omega}_{oR} \text{ (for clear coastal water)} = \frac{.014}{.049} = .286$$

In accordance with the assumption of linearity,

$$\frac{N_{R1} - K'_R}{N_{R2} - K_R} = \frac{\widetilde{\omega}_{oR1}}{\widetilde{\omega}_{oR2}} \qquad \text{(Subscripts 1, 2 refer to sampling locations)}$$

If $\widetilde{\omega}_{oR1}$ is taken to be the known value (e.g. for clear coastal water),

$$\widetilde{\omega}_{oR2} = \frac{N_{R2} - K'_R}{N_{R1} - K'_R} \times .286$$

It may also be assumed that the turbidity, T, is proportional to β.

Therefore,

$$\frac{\beta_{R2}}{.035 + \beta_{R2}} = \frac{N_{R2} - K'_R}{N_{R1} - K'_R} \times .286$$

$$\text{Let } \frac{N_{R2} - K_R'}{N_{R1} - K_R'} = \rho_p$$

$$\beta_{R2} = .01 \, \rho_p + .286 \, \rho_p \, \beta_{R2}$$

$$= \frac{.01 \, \rho_p}{1 - .286 \, \rho_p} \qquad\qquad (20)$$

For $\beta = .014$, $T = 1.0$ Jackson Unit

$$\text{Thus, } T_{R2} = \frac{.01 \, \rho_p}{(1 - .285 \, \rho_p)\,(.014)}$$

For example, if $\rho_p = 3$

$$T_{R2} = \frac{.03}{(1 - .86)\,(.014)} = 15 \text{ Jackson Units}$$

Obviously the validity of the relationship is limited to significantly below a value of 3.5 for ρ_p since the value of β_{R2} would rise rapidly toward infinity.
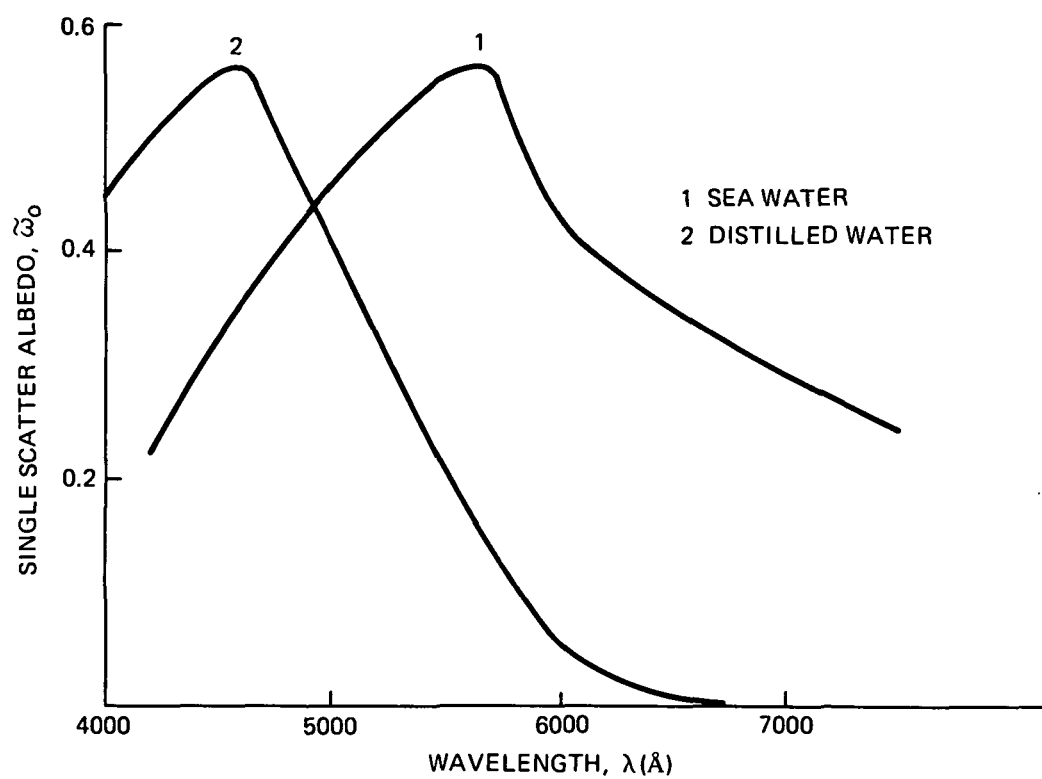
Fig. 9 Single Scatter Albedo as a Function of Wavelength, Feinstein and Piech, Ref. (11)

4. The Influence of Non-Effluent Turbidity

Or Lower Concentrations Of Particulates

The first-order approach to the determination of water depth photometrically involves the assumption of the constancy of several parameters which may not actually remain constant over the few square miles covered in the survey of a given area. One of the prinicpal parameters which may be somewhat variable is the transparency of the water.

In terms of equation (3) repeated as follows for convenience,

$$\log (G_1 - K_G) = \log \left[(1-\rho_w) H_s \rho_{bG} \right] - 2df (\alpha + \beta)_G \qquad (3)$$

it is obvious that, if $(\alpha + \beta)_G$ is variable between area 1 and area 2, equations (5) and (6) derived from it cannot hold true. The same comment applies as regards the bottom reflectance variability. Furthermore, if the value of $(\alpha + \beta)_G$ changes materially, the constancy of the term, K_G is questionable.

In shallow water where the bottom reflection dominates the radiance function of the area it may be assumed that the variation of K_G is less significant than the attenuation of bottom signature through the $(\alpha + \beta)_G$ factor. Therefore, it is useful to develop an approximation under assumption of constant K_G for the correction of $(G_1 - K_G)$ for a known change in $(\alpha + \beta)_G$.

Assume that $(\alpha + \beta)_{G1} = (\alpha + \beta)_{G2} + \Delta$, where Δ is a symbol for the change in attenuation coefficient between stations. It can be shown that the following relationship holds if bottom reflectance and H_s are constant,

$$\log_{10} \frac{G_1 - K_G}{G_2 - K_G} = 2f (\alpha + \beta)_{G2} (d_2 - d_1) - 2f d_1 \Delta \qquad (21)$$

Comparing th_s relationship with equations (8) and (9) it is seen that allowance for a change in slope of a plot of $\log (G - K_G)$ vs. distance from shore due to a change in turbidity (or attenuation coefficient) must take into account the depth at which the change occurs. A change in slope due to a change in bottom reflectance alone has been shown to be independent of depth.

Experience shows also that there is frequent layering of turbidity in natural waters so that the vertical gradients of $(\alpha + \beta)_G$ must be taken into

account in arriving at a value for Δ.

In water of sufficient depth, or turbidity where the radiance function is not strongly dominated by bottom reflection it may be useful to consider radiance changes as a manifestation of variation in the otherwise-assumed constants, K_G, and K_R. Out of the whole area under surveillance, if it is possible to select sections which should be of uniform water properties, a value of K_G (or K_R, etc) can be computed to fulfill equations (5) and (6) if the attenuation coefficient, $(\alpha + \beta)$, and the difference in depth, $(d_2 - d_1)$ are known. If G_2 and G_1 are the observed radiance values corresponding to depths 2 and 1, $(\alpha + \beta)_G$ is the attenuation coefficient, and Q is the value of antilog 2f $(\alpha + \beta)$ $(d_2 - d_1)$, then

$$K_G = \frac{G_2 Q - G_1}{Q - 1} \qquad (22)$$

Again, the assumptions of constancy in bottom reflectances and solar irradiance apply.

Using this relationship it is possible to fit K-values along with $(\alpha + \beta)$ values to various portions of the area. It remains, of course, to interpret these localizations. The computations may serve to locate and quantify areas of buoyant particulates, or scum.

The analysis of a body of water which is complex (in the sense that there are sectional variations in water clarity and other parameters) can be facilitated by the examination of the radiance vs. depth function. This is not a new concept. It has been suggested, for example by Brown, et al, of the University of Michigan[5] that if the radiance vs. depth is plotted on a semi-logarithmic scale the slope will be proportional to the volume attenuation coefficient, $(\alpha + \beta)$ and the intercept (at depth = zero) will be the apparent bottom reflectance, defined in our terminology as $(\rho_b - \rho_\mu - \rho_{sp} - \rho_{rsk} - \rho_a)$

By application of equation (6) to the comparison of zero depth radiance, G_0 with radiance at some depth, G_d, the following equation is formed:

$$\log_e (G_d - K_G) = \log_e (G_0 - K_G) - 2f (\alpha + \beta)_m d \qquad (23)$$

For convenience in differentiating this expression natural logarithms and

$(\alpha + \beta)_m$ in meters $^{-1}\log_e$ have been used.

By differentiation, assuming that within a restricted section K_G and $(\alpha + \beta)_m$ are constants,

$$(\alpha + \beta)_m = - \frac{\partial G_d}{\partial d} \times \frac{1}{2f \, (G_d - K_G)} \qquad (24)$$

An alternate two-color method of analysis has been suggested by Brown, et al (5). Using our terminology, equation 2.13 of this reference, involving differentiation with respect to depth can be expressed as follows:

$$(\alpha + \beta)_R - (\alpha + \beta)_G = \frac{\dfrac{G_2 - G_1}{R_2 - R_1} \Big/ (d_2 - d_1)}{2f \left[\dfrac{G_2 - G_1}{R_2 - R_1}\right]} \qquad (25)$$

If the difference $(\alpha + \beta)_R - (\alpha + \beta)_G$ is known it can be associated closely with actual values of $(\alpha + \beta)_R$ and $(\alpha + \beta)_G$ typical of the water in the area.

In accordance with the treatment by Moore (4) it is possible to analyze uniform water characteristic sections of a total area of interest without the necessity of using the deep-water radiance values, K_G, K_R, etc. Then, of course, using equation (22) these K-values can be computed in order to fit the attenuation equations to the observed facts. The resulting K-values are indicative of the state of turbidity, or water transparency.

Moore's derivation, not shown in detail in reference (4), is given here in terms of our nomenclature:

Re-stating equation (14) in the exponential form of eq. (2), re-arranging terms, and introducing the geometric factor, f

$$\frac{G_1}{\phi_G} = K_G + H_s \, (1-\rho_w) \, \rho_{bG} \, e^{-2d_1 \, f \, (\alpha + \beta)_G} \qquad (26)$$

However, it has also been stated that K_G, K_R, etc. are made up of components g_u, g_{sp}, etc., each of which can be considered the product of H_s and an effective reflectance (e.g. ρ_{uG}, ρ_{rsk}, ρ_{aG} etc). Therefore, if the sum of the constituent

reflectances, $(\rho_{uG} + \rho_{spG} + \rho_{rskG} + \rho_{aG})$, can be considered to be ρ_{TG} then

$$\frac{G_1}{\phi_G} = H_s\, \rho_{TG} + H_s(1-\rho_w)\rho_{bG}\, e^{-2\, d_1\, f\, (\alpha + \beta)\, G}$$

or $\quad G_1 = H_s\, \phi_G\, \rho_{TG} \left[1 + (1 - \rho_w)\, \frac{\rho_{bG}}{\rho_{TG}}\, e^{-2\, d_1\, f\, (\alpha + \beta)_G} \right]$ (27)

Applying the same treatment to G_2 and G_3

$$G_1 - G_2 = H_s\, (1 - \rho_w)\, \rho_{bG}\, \varphi_G \left[e^{-2\, d_1 f\, (\alpha + \beta)_G} - e^{-2\, d_2 f\, (\alpha + \beta)_G} \right]$$

$$G_1 - G_3 = H_s\, (1 - \rho_w)\, \rho_{bG}\, \varphi_G \left[e^{-2\, d_1 f\, (\alpha + \beta)_G} - e^{-2\, d_3 f\, (\alpha + \beta)_G} \right]$$

and $\quad \dfrac{G_1 - G_2}{G_1 - G_3} = \dfrac{e^{-2\, d_1\, f\, (\alpha + \beta)_G} - e^{-2\, d_2\, f\, (\alpha + \beta)_G}}{e^{-2\, d_1\, f\, (\alpha + \beta)_G} - e^{-2\, d_3\, f\, (\alpha + \beta)_G}}$

or $\quad \dfrac{G_1 - G_2}{G_1 - G_3} = \dfrac{1 - e^{-2\, (d_2 - d_1)\, f\, (\alpha + \beta)_G}}{1 - e^{-2\, (d_3 - d_1)\, f\, (\alpha + \beta)_G}}$ (28)

A pragmatic step is introduced at this point in the analysis to indicate the examination of G-values at equal depth intervals (i.e. $d_2 - d_1 = d_3 - d_2$). Thus $(d_3 - d_1) = 2\, (d_2 - d_1)$.

Under these conditions,

$$\frac{G_1 - G_2}{G_1 - G_3} = \frac{1 - e^{-2f(d_2 - d_1)\, (\alpha + \beta)_G}}{1 - e^{-4f(d_2 - d_1)\, (\alpha + \beta)_G}}$$ (29)

By taking on each side of this last equation the ratio of the numerator to the quantity, (denominator - numerator),

$$\frac{G_1 - G_2}{G_2 - G_3} = \frac{1 - e^{-2\, f\, (d_2 - d_1)\, (\alpha + \beta)_G}}{e^{-2f\, (d_2 - d_1)\, (\alpha + \beta)_G} - e^{-4f\, (d_2 - d_1)\, (\alpha + \beta)_G}}$$ (30)

Dividing numerator and denominator of the right-hand side of this equation

by $1 - e^{-2f(d_2 - d_1)(\alpha + \beta)_G}$

$$\frac{G_1 - G_2}{G_2 - G_3} = \frac{1}{e^{-2f(d_2 - d_1)(\alpha + \beta)_G}}$$

or

$$\frac{G_1 - G_2}{G_2 - G_3} = e^{2f(d_2 - d_1)(\alpha + \beta)_G} \qquad (31)$$

Providing the attenuation coefficient is expressed in $ft^{-1} \log_{10}$ units this equation has the alternate form:

$$\frac{G_1 - G_2}{G_2 - G_3} = 10^{2f(d_2 - d_1)(\alpha + \beta)_{G\,(FT)}} \qquad (32)$$

In logarithmic form

$$\log_{10} \frac{G_1 - G_2}{G_2 - G_3} = 2f(d_2 - d_1)(\alpha + \beta)_{G\,(FT)} \qquad (33)$$

The use of this relationship permits the analysis in homogeneous zones of water properties where the bottom reflection is sufficiently strong that it is a predominant influence on the radiant signature. In our case, in order to determine $(\alpha + \beta)$ values it is necessary to have a fathometer trace from which points of equal separation in depth can be determined. The corresponding radiance values may be ratioed and the known depth differential, $(d_2 - d_1)$ can be used to substitute in equation (33) for the calculation of $(\alpha + \beta)_G$. If the radiance values are R_1, R_2, R_3, then $(\alpha + \beta)_R$ is calculated.

It should be noted that the calculation applies only to the layer of water between the depths d_1 and d_3. There is no guarantee that the layers, above or below these points will be characterized by the same attenuation characteristics.

If the total body of water contains anomalous regions of turbidity, selection of widely separated points for radiance comparisons will not yield meaningful results. For the analysis of any one uniform region a depth change of significant slope value must be found.

5. <u>The Multiple Scatter Photometric Turbidity Model</u>

The presence of particulates in natural waters affects the reflection of sunlight, and the measurement of this effect could presumably be used to determine the concentration of the particulates. The physical situation is very complex involving detail characteristics such as the scattering pattern of the particles (e.g. Rayleigh and Mie types), the presence of contaminant with molecular absorption, the spectral pass band of the measuring device, and other factors. Depending upon the scattering model chosen, and the assumptions made, it can be concluded, on the one hand, that the turbidity will lower the effective reflectance, (10) or, on the other hand, that it will raise it (11). It is probably true that large bodies of deep contaminated water containing typically balanced absorbing and scattering constituents will appear darker than clear water. However, as has frequently been observed, effluents carrying a larger proportion of scattering particles as a fresh discharge into a large body of water will usually appear lighter than the surrounding water (1), (11). The wavelength of observation is very important as is shown in curves generated by Plass, et al (10). There is a strong likelihood that particulate contamination may darken the sunlit water as observed in the blue. There is a much improved chance for the lightening action in the red. Obviously, in order to evaluate particulate contamination photometrically, a measureable effect, in either direction, must be present.

The efforts of the Cornell Aeronautical Laboratory under "Project Aquamap" seem to have been based on the case of increased reflectance by the particulate light-scattering contaminant (11). It would appear that this is the practical case usually for the evaluation of contaminating effluents, or discharges into rivers, lakes, harbors, etc. One may call this the case of the anomalous turbidity where the effluent is still localized. Among other factors affecting the appearance of a localized effluent is the penetration of oblique and scattered sunlight into the effluent from below and from the sides where the scattering pattern may be much closer to the isotropic case.

It has been pointed out by several investigators (10) (12) that calculation of the relationship between particulate contamination and turbidity must be based upon multiple scattering rather than single scattering. Plass, et al (10) have performed extensive calculations using Monte Carlo techniques based upon

certain assumptions which these authors believe to represent typical contam-
ination conditions. It is our opinion that there may be rather extensive
exceptions to these assumed conditions, and that the case of anomalous localized
turbidity from effluents (such as sewage outfalls) almost always falls within
the category of exceptions. It is believed that this may serve to explain the
apparent contradiction where the assumption is made, almost unquestioningly,
that the effluent area will appear to have higher reflectance.

As we have done also Piech, et al (9) and Silvestro (13) of Cornell
Aeronautical Laboratory begin with empirical data (photoelectric in our case,
photographic in the CAL case) which show heavier concentrations as relatively
bright areas. In both cases the effluent plume can be termed buoyant, and in
this respect forms an exception to the cases treated by Plass et al.

In the absence of a good mathematical model optical photometric data can
be used for linear extrapolation of data from laboratory analysis of in situ
water samples. In other words if radiance values can be measured for two
concentrations of contaminant then interpolation (or extrapolation) can be
based upon the assumption that the concentration of pollutant will be a linear
function of radiance. This can be done whether the trend of radiance may be
positive, or negative with respect to concentration. Recently, Granatstein,
Rhinewine, Levine, Feinstein, Mazurouski, and Piech (12), representing both
Bell Telephone Laboratories and Cornell Aeronautical Laboratory have published
the results of a combined analytic and experimental program directed toward
application of multiple scattering theory to the quantitative remote sensing
of turbidity in water. Again, the status of this body of theory is such that
it is best applied to practice presently only in the restricted form of a
non-linear (as opposed to a simpler linear) interpolation of data obtained
from actual water samples. It is very difficult, due to the lack of adequate
physical model data, to apply multiple scattering analysis. However, in
recognition of the fact that this is the correct direction in which to proceed,
we have made an attempt to use the limited model data presented by Granatstein
et al (12).

It should be noted that this model is set up in such a way as to explain
cases where the turbid areas are brighter than the non-turbid areas. Turbidity
is a term associated with the presence of particulate matter which predominately

scatters rather than absorbs radiant flux. The presence of non-turbid molecularly absorbing contaminant liquids is presumably not the subject of investigation, although ecologically important. In comparison to physical models used by Plass et al (10), which almost never predict higher radiance for greater turbidity, the following differences seem to exist:

1. Plass, et al, assume a distribution of particle sizes which emphasizes those larger in diameter than one μm (modal radius of 3 μm) whereas the BTL-CAL model assumes a distribution emphasizing particles smaller than the wavelength of observation. Both models assume Mie scattering by these particles against a background of Rayleigh scattering by water molecules.

2. Plass, et al tend to emphasize the effects at the blue and of the spectrum whereas the other model emphasizes the effects in the red end. This affects the analysis through particle size relative to the wavelength.

3. The assumed index of refraction for the Plass model is 1.15 relative to water whereas the Teflon used experimentally by the other group has an index of refraction only 1.03 relative to water. This assumption would seem to downgrade the reflectance signature of the BTL-CAL model relative to the Plass model.

Because of the predominance of forward scatter over back-scatter the Mie-type models favor downward radiant transport, only to have the flux lost by absorption in the water depths. This effect is more extreme for the larger particles, and becomes mild for the smaller particles which scatter in a more isotropic-type pattern as they become of light-wavelength size and smaller. It appears that this is the chief difference between the models. It is not known at this time whether the particles to be found in sewer outfalls, for example, resemble more closely the Plass assumption or the BTL-CAL assumption. However, because of the fact that there is presently little model information available it was decided to interpret our data in terms of the BTL-CAL model. At least this model does fit the case of increased radiance effluents which we observe in our data. While our approach shows the factors which must be considered we cannot claim that it is exact. Accuracy can be achieved, it is

believed, if realistic models are generated experimentally and analytically.

Our water-sampling analysis for turbidity is based upon reduction to Jackson Units which are explained elsewhere in this report. In this way we avoid the question of concentration of the contaminant in weight per unit volume, although the correlation between concentration of the standard (Jackson Unit) particulate and the unknown can be determined by laboratory comparisons. We establish the relationship between the extinction coefficient of the contaminated water and the turbidity in Jackson Units by calculation since our laboratory turbidimeter measures transparency of a one inch thickness of the sample. As in most of the analysis of this report an underlying assumption is that the increase in attenuation over that of clear water is entirely due to scattering by particulate matter. This is an assumption which would not be justifiable under some circumstances. Other measurements can, and should be made to satisfy the requirements of future realistic models.

The correlation of transparency (one inch), turbidity in Jackson Units and extinction coefficient is shown in Figure 10, first of all for the green 5300A-centered band, and then (by computation) for the red 6250A -centered band. Fitting the correlation function to a straight line assumption we obtain the equation:

$$T = 60 \ (\alpha + \beta)_R - 1.9 \qquad (34)$$

where T is the turbidity in Jackson Units

For example at $(\alpha + \beta)_R = .05$

$T = 60 \times .05 - 1.9 = 1.1$ Jackson Units and at

$$(\alpha + \beta)_R = .4$$

$T = 60 \times .4 - 1.9 = 22.1$ Jackson Units

Having established a relationship between the extinction coefficient $(\alpha + \beta)$ and turbidity it remains to establish a relationship between changes in this extinction coefficient and changes in the radiance of the water which is what we directly measure with our airborne photometer. For the purpose of setting up this relationship, we make use of the BTL-CAL model in spite of the probable variation from an accurate fit to our data. Figure 11 shows the

fitting of a straight line function to a semi-logarithmic plot of the model (reflectance vs. single scatter albedo, $\tilde{\omega}_o$). The equation of the function in terms of a slope S is as follows:

$$\text{Log}_{10} \frac{I}{I_o} = S\, \tilde{\omega}_o - D$$

or

$$\text{Log}_{10}\, I = S\, \tilde{\omega}_o - D + \text{Log}\, I_o \tag{35}$$

In order to avoid the use of I_o values comparisons are made between elemental areas 1, 2, 3, ... with radiances I_1, I_2, I_3, ..., obtaining the relationship

$$\text{Log}_{10} \frac{I_1}{I_2} = S\, (\tilde{\omega}_{o_1} - \tilde{\omega}_{o_2}) \tag{36}$$

We have evidence that the value of S which fits our red (R) data is .75.

In order to incorporate $(\alpha + \beta)$ the definition of $\tilde{\omega}_o$ is used:

$$\tilde{\omega}_o = \frac{\beta_R}{(\alpha + \beta)_R} \tag{37}$$

in which $(\alpha + \beta)_R$ represents the total extinction coefficient and β_R the scattering coefficient in the R spectral band.

The assumption is made that the pollutant contributes no additional molecular absorption, thus

$$\beta_R = (\alpha + \beta)_R - \alpha_R \tag{38}$$

In which α_R is the absorption coefficient of pure water in the same spectral band.

Thus

$$\tilde{\omega}_o = \frac{(\alpha + \beta)_R - \alpha_R}{(\alpha + \beta)_R}$$

$$\tilde{\omega}_o = 1 - \frac{\alpha_R}{(\alpha + \beta)_R} \tag{39}$$

and

$$\tilde{\omega}_{o_1} - \tilde{\omega}_{o_2} = \alpha_R \left[\frac{1}{(\alpha + \beta)_{R_2}} - \frac{1}{(\alpha + \beta)_{R_1}} \right] \qquad (40)$$

where subscripts 1 and 2 refer to the characteristics of sampled areas 1 and 2.

Substituting equation (40) into equation (36) and using a value of $S = .75$ the following relation is obtained:

$$\log_{10} \frac{I_1}{I_2} = .75 \ \alpha_R \left[\frac{1}{(\alpha + \beta)_{R_2}} - \frac{1}{(\alpha + \beta)_{R_1}} \right] \qquad (41)$$

This last equation provides a means of extrapolating from a measured value of $(\alpha + \beta)_R$, such as $(\alpha + \beta)_{R_1}$, to another unknown value, $(\alpha + \beta)_{R_2}$ based upon the ratio of the radiances, I_1 and I_2, which are measured from the air.

Granatstein, et al (12) do not enter into detail as to the application of the model to actual remote measurement of turbidity, but it is obvious that radiances measured from the air contain extraneous light contributions reflected from the atmosphere and from the surface of the water (sky reflection mostly). One of the authors, K. R. Piech, treats this matter in some detail elsewhere (13).

As far as we are concerned the values I_1 and I_2 are obtained by subtracting from actual measured radiances the sky reflection and atmospheric reflection radiances, as well as other extraneous radiances which may occasionally become significant. In many cases residual attenuated bottom reflection may be important.

Having obtained a value of $(\alpha + \beta)_{R_2}$ it is then possible to substitute in equation (34) to calculate the finally desired value of turbidity in Jackson Units.

If the pollutant does contribute significant molecular absorption, the application of the above equations will result in an under-estimation of the turbidity. Equations can be developed which include all factors of importance. In the present instance we are handicapped by a lack of information as to the characteristics of the effluent and therefore, treat the case in a simplified

fashion.

As further evidence for our contention that the presence of some particulates actually enhances reflectance, particularly in the longer wavelengths of the visual spectrum we offer Figure 12 which is taken from Clarke, Ewing and Lorenzen (14). These data were taken at the Brewster angle of observation, directed away from the sun, and with a polarizing filter oriented to screen out the horizontally polarized sky reflection. The curves were taken at different locations and times, but since reflected values were reduced to percentages of incident light, it seems proper to conclude that the presence of the chlorphyll in the form of phytoplankton particulates does actually increase the reflectance in the green and red parts of the spectrum. However, in good accordance with the Plass model the reflectance is depressed in the blue by this same concentration of particulates.
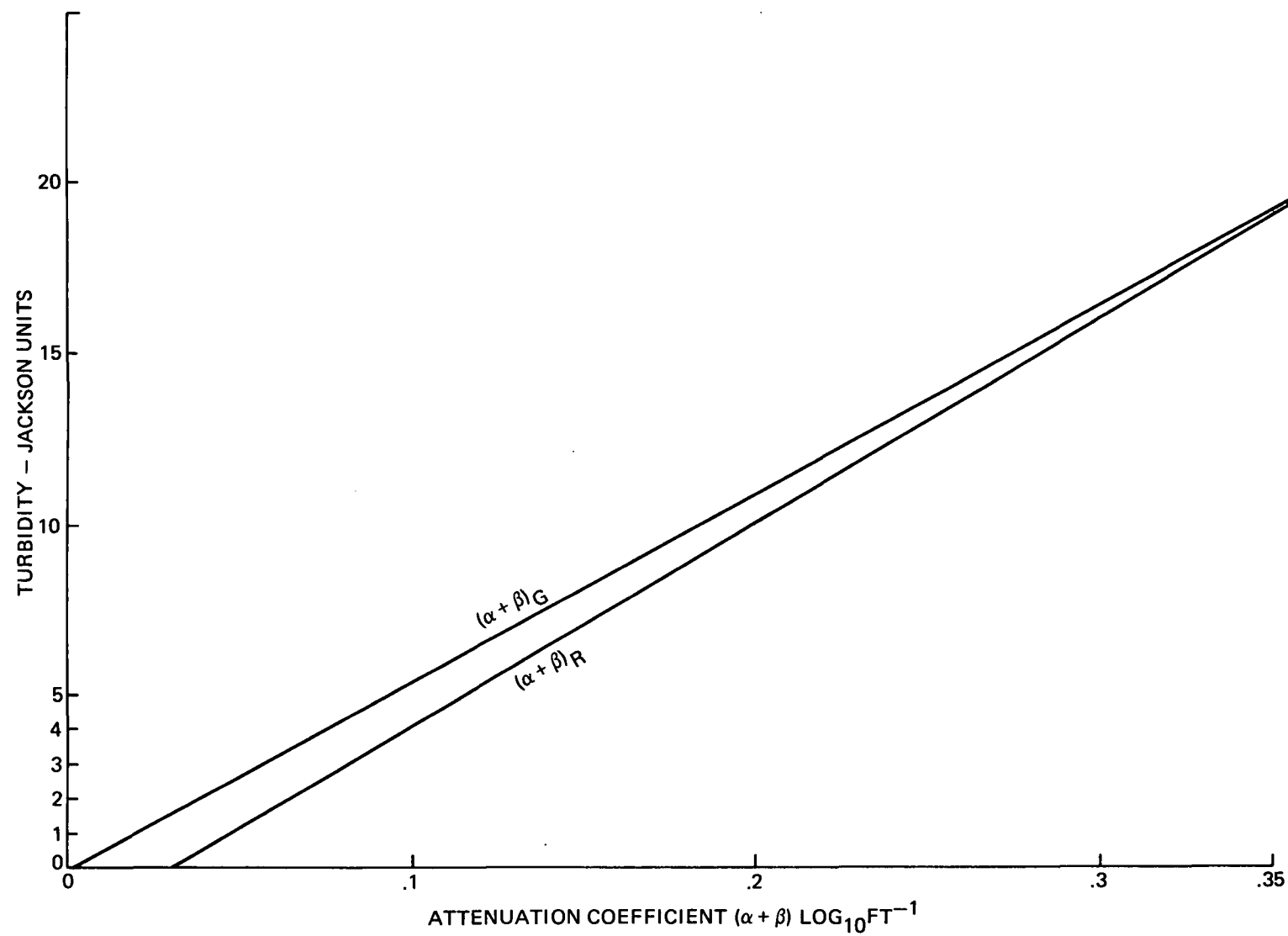
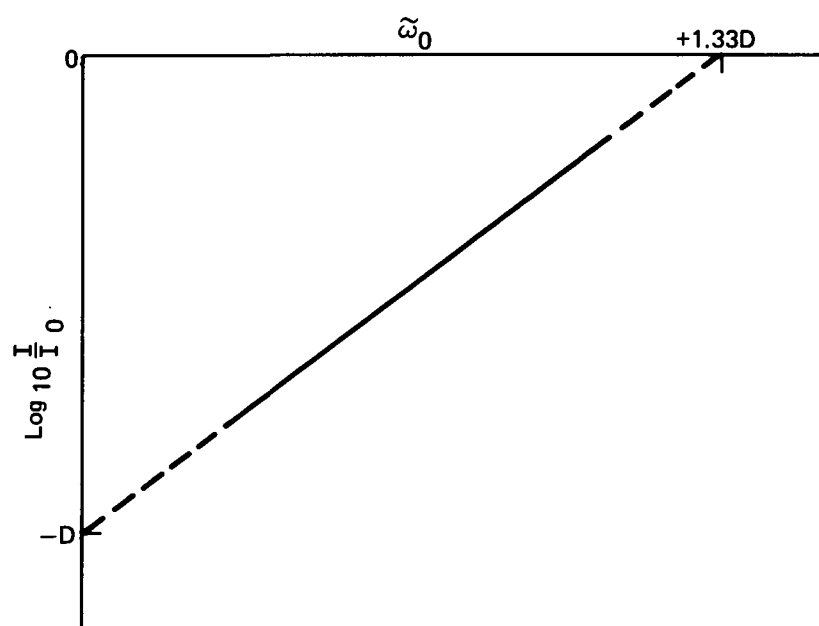Fig. 10 Relationship Between Turbidity and Volume Attenuation Coefficient

Fig. 11 Log $_{10}$ Relative Radiance Vs Single Scatter Albedo, $\widetilde{\omega}_0$
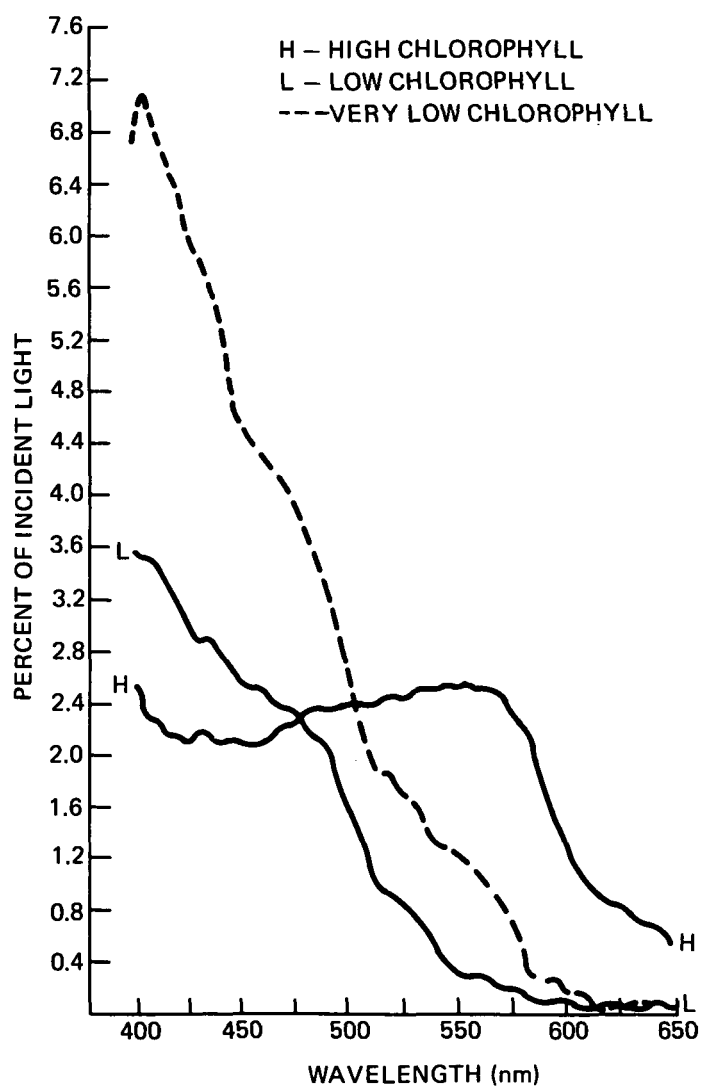
Fig. 12 Effect of Chlorophyll on Sea Water Reflectance, Clarke et al Ref. (14)

6. The Polarimetric Turbidity Model

In the preceding treatment of the optical signature of water we have ignored the differences in reflectance which may arise between different vectorial components of the reflected light. Analytically it can be shown that differences will arise, and experimentally these differences have been shown to exist (1).

One of the important factors in water signature is the Fresnel reflection of the water surface as summarized in Fig. 13 for smooth water. These data refer to a principal plane containing the normal to the surface, the direction of incidence of collimated light, and the viewing direction. Therefore, the values apply to observational geometry controlled with respect to the solar incidence direction in such a way as to maintain a principal plane relationship.

When the natural water surface is examined by a directional viewing system the sky radiance is specularly reflected in accordance with the Fresnel relationships. Thus the value of ρ'_w can be computed from the Fresnel equations with due allowance for water surface irregularities, if they exist. Since the value of ρ'_w varies with the vector chosen and the angle of viewing, polarization can be introduced.

Sunlight incident obliquely upon the water is affected by the same relationships. In this case we are more concerned with the transmitted portion, which is also polarized in accordance with Fresnel equations, again varying in degree depending on the obliquity. In terms of the principal plane s and p references the p-component is favored over the s-component. After back-scattering from sub-surface particles the light transmitted upward through the water boundary is again affected by the consequences of the Fresnel relationships in refraction. Again, the p-component is favored if the viewing is oblique. These generalizations apply to g_u and to g_b, both of which involve ρ'_w in a similar way.

The multiple scattering which occurs in a volume of water through which polarized light may be transmitted tends to degrade the polarization. This depolarization is a function of path length. There are very few data on the quantitative aspects of de-polarization in water, although it can be surmised that it is much more pronounced than that which occurs as a result of multiple scattering in air (15). We are concerned with the polarization characteristics of the g_b (d) and g_u (d) components of the total signature which

originate below the water surface. The scattering laws and the empirical evidence point to a principal plane polarimetric signature for clear deep water which emphasizes the s-component in the reflection signature as shown in Fig. (14). There is ample evidence that the bottom signature, measured immediately over the bottom, would also inherently emphasize the s-component. If the water is deep, it is assumed that the polarimetric s-emphasis contributed by the bottom would be markedly degraded before reaching the surface. If anything, the presence of particulate matter in the water would degrade this s-component emphasis through multiple scattering.

Because of the severe attenuation of light by water the optical signature is weighted heavily in favor of contributions by back-scattering near the surface. If this back-scattering is of such a nature that the net effect of added contaminants is to increase the reflectance of the body of water, the probable effect on polarization (under oblique directional viewing and/or illumination) is to add substantial emphasis to the p-component relative to the s-component. In other words, in terms of the conventional description of principal plane measurements a trend in the negative polarization direction will be induced. If the net effect of the added contaminants is to decrease the reflectance of the water, the effect on polarization will probably be much milder. The confidence of prediction breaks down partly due to a lack of knowledge of how much the "skin effect" of reflection from water contributes to the clear water polarimetric signature shown in Fig. 14.

It is not too difficult to perform laboratory simulation to determine the optical effects of adding contaminant to water which increases the reflectance. Simulation where the effect of adding contaminant is to decrease the reflectance is much more difficult, because the effect comes about by reason of an integration of light up-welling from depth. Probably the answer can best be developed by field experimentation combined with computer simulation. Multispectral analysis should be useful because it should be possible to find contamination in natural bodies of water which enhances the reflectance in the red at the same time that it depresses the reflectance in the blue.

In designing field experiments in polarization to detect and measure the turbidity of coastal or harbor waters, the bottom signature becomes important.

In very shallow water the bottom signature is dominant regardless of the turbidity. Of course the influence on bottom signature is a means of evaluating water transparency in these areas. However, it is important to have means of determining whether an apparent change of reflectance is due to bottom effects, or to water parameters. It is believed that polarimetry can be a very useful means toward correct interpretation. We have designed the experiments reported in this study in the red end of the visual specturm. This in itself tends to minimize the bottom signature relative to prominent back-scattering by the water in the red because of the greater attenuation of the water. We believe also that evaluation of effluent and harbor contamination of particles of organic origin may best be done in the red because there is evidence that the reflectance of the water is usually increased by their presence. In order to still further minimize the effect of bottom signature on polarization signature we examine the water by near normal viewing rather than oblique viewing (such as Brewster angle). It is our belief that the sunlight reaching the bottom will be completely depolarized even if the sunlight strikes the water quite obliquely. The probability of residual polarization in the bottom signature reflected up through the water and viewed normal to the water appears low. On the other hand obliquely incident sunlight should be an influence toward a p-component emphasis in the normally viewed back-scatter from particulates below the surface of the water. Admittedly we are placing an emphasis on the particulates at shallow depth in the water.

It should be noted that viewing at an angle-off-normal sufficiently large to noticeably affect the difference between Fresnel s and p reflectance factors for up-welling light will inevitably make the bottom reflection look somewhat negative in polarization as well as further enhancing the negative trend in the particulate back-scatter polarization. Thus, for oblique viewing the negative trend becomes a means of differentiating between sub-surface and surface effects because the refraction of the water boundary is the responsible factor. However, to minimize bottom reflection ambiguity it would be desirable to eliminate by use of normal viewing the negative trend in bottom signature by refraction.

We have previously reported the preliminary development of a mathematical model for the polarimetric signature of turbid water (1). This model was based upon laboratory measurements in which the broad visual spectrum was used (16). It

has not been possible to conduct appropriate laboratory simulation to develop a modification of the original model. After a certain amount of study of our Long Island Sound field data it was concluded that the original model would probably suffice for an explanation of the trends.

The expression for percent polarization, P, as a function of turbidity-induced radiance, L, is extracted from reference (1) as follows:

$$P = \frac{2.5\ K_n + .07\ L}{5.0\ K_n + 1.89\ L} \tag{42}$$

In this expression K_n is the radiance due to molecular scattering and other non-turbidity related effects in pure water. It is realized that these small effects have been previously neglected in this study where photometric analysis of effluent plumes and similar strongly-reflecting features has been discussed. We find, however, that the polarimetric signature is quite dependent upon this phenomenon. The largest numerical values of polarization are those for the clearest water, and the positive bias which is responsible derives from this type of scattering largely.

Another effect which is included in equation (42) is that of specular reflection of the sky. This has been merged with K_n by use of the assumption that it is 25% of K_n.

The characteristic curve of polarimetric signature resulting from plotting P as a function of L measured in units of K_n is shown in Fig. 15. The term "L" has been substituted for our original "T" because we have used "T" to denote turbidity measured in Jackson Units in this report. This relationship allows us to proceed to convert to Jackson Units in accordance with equations (34) and (41) already presented in connection with the evaluation of effluents. Radiance which can be ascribed to turbidity alone is exactly in the form required for the ratio $\frac{I_1}{I_2}$ from equation (41) which is repeated as follows:

$$\log_{10} \frac{I_1}{I_2} = .75\ \alpha_R \left[\frac{1}{(\alpha + \beta)_{R_2}} - \frac{1}{(\alpha + \beta)_{R_1}} \right] \tag{41}$$

By introduction of relationships,

$$\alpha_R = .035$$

$$(\alpha + \beta)_{R_2} = .049 \text{ (for 1 Jackson Unit)}$$

the expression becomes

$$\log_{10} \frac{I_1}{I_2} = \frac{.75 \times .035}{.049} - \frac{.75 \times .035}{(\alpha + \beta)_{R_1}}$$

$$(\alpha + \beta)_{R_1} = \frac{.026}{.53 - \log_{10} \frac{I_1}{I_2}}$$

(42)

In order to be able to calculate $(\alpha + \beta)_{R_1}$ it is necessary to determine the ratio, $\frac{I_1}{I_2}$, between the values of L_1 and L_2. L_2 is the radiance where the turbidity is 1 Jackson Unit. In terms of our model (Fig 15) it is quite possible to obtain the ratio from values of L in multiples of K_n since the latter will cancel out of the fractional value. It is necessary to decide what value of L corresponds to water of clarity corresponding to 1 Jackson Unit. The method can be clarified by an example from our "Throg's Neck" flight data (see section on Polarimetry Data) As in the case of Boston Harbor we made this decision by examination of the actual field data. It corresponds to about the highest positive polarization percentage measured during the flight which was in the region of 25%. Therefore the point corresponding to $L = 3 K_n$ was chosen. Its indicated percent polarization is 24.3%. Naturally one could be more certain if more extensive water sampling had been performed.

After calculating the value of $(\alpha + \beta)_{R_1}$ it is substituted in equation (34) to determine the turbidity in Jackson Units.

A numerical example may serve to clarify the procedure. Near the beginning of our flight path the percent polarization was determined to be 17%. From Fig. 15 it is ascertained that $L = 6.7 K_n$.

Therefore,

$$\frac{I_1}{I_2} = \frac{6.7\ K_n}{3.0\ K_n} = 2.23$$

$$\log_{10} \frac{I_1}{I_2} = 0.348$$

$$(\alpha + \beta)_{R_1} = .143$$

$$T = 60\ (\alpha + \beta)_{R_1} - 1.9$$

$$= 8.6 - 1.9 = 6.7\ \text{Jackson Units}$$

Obviously a method such as this for reduction of percent polarization to Jackson Units of turbidity enables the preparation by computer of a turbidity map from a polarization map. An example will be shown in the reduction of the data.

At this point it is opportune to review what advantages may be realized from polarimetric analysis in spite of uncertainties which have been discussed.

First is the degree of relief in polarimetry from purely photometric ambiguities due to cloud shadows and uncertainties about solar irradiance levels due to other causes. A photometric approach must be based upon radiance relative to solar irradiance, or the reflectance in quantitative terms. Knowledge of the irradiance at the surface of the water is required. If solar values are measured at an aircraft it must be assumed that the values at the water surface can be computed, but this assumption is very questionable for prevalent cloud shadows, even if the clouds are thin. The uncertainty increases with altitude bringing in questions of atmospheric variables as well as clouds. Also for exact measurement of reflectance under real conditions some account must be taken of sky contributions to irradiance. Sky reflectance is one of the variables which also generates uncertainty in the interpretation of polarization, but to a lesser degree. Percent polarization is a quantity relatively independent of the transient variability of irradiance.

Second is the factor which we have just discussed, the possible capability of distinguishing water turbidity from changes in bottom signature under appropriate viewing conditions where shallow coastal or inland waters are being examined.

Third is the potentiality of distinguishing between purely surface scum and particulates under the water surface. Presumably, the surface scum would contribute more s-component than p-component when illuminated and/or viewed obliquely. This differentiation may be very difficult even polarimetrically, but seems virtually impossible by non-vectorial photometry.

One of the principal disadvantages of the polarimetric approach may be that its effectiveness is confined to layers of water near the surface. If the first few feet of depth are quite turbid, but overlay a much clearer body of water, it is probably not to be expected that polarimetry will reveal the deep clear condition. Non-vectorial photometry may be used in a multispectral mode to clarify the interpretation. It is true any form of photometry will yield more response from the top layers, but there are non-polarimetric effects, such as, for example, the measurement of residual bottom signature, which may help to solve the puzzle.

Based upon analysis and experience to date it appears that there is no invariable relationship between percent polarization and turbidity. The same comment can be made about over-all radiance and turbidity. In both cases local "ground truth" data must be used for an accurate interpretation. However, it also appears that it is much easier to approximate the measurement of turbidity by polarization than by straight photometry. Less accessory data and less exacting calculation are characteristic features of the polarimetric approach.

Obviously the best answers are provided by a number of measurements - polarimetric, multispectral, in situ sampling, sky measurements, solar measurements, etc. The use of a computer-compatible sensor makes it possible to process these many inputs by digital techniques.
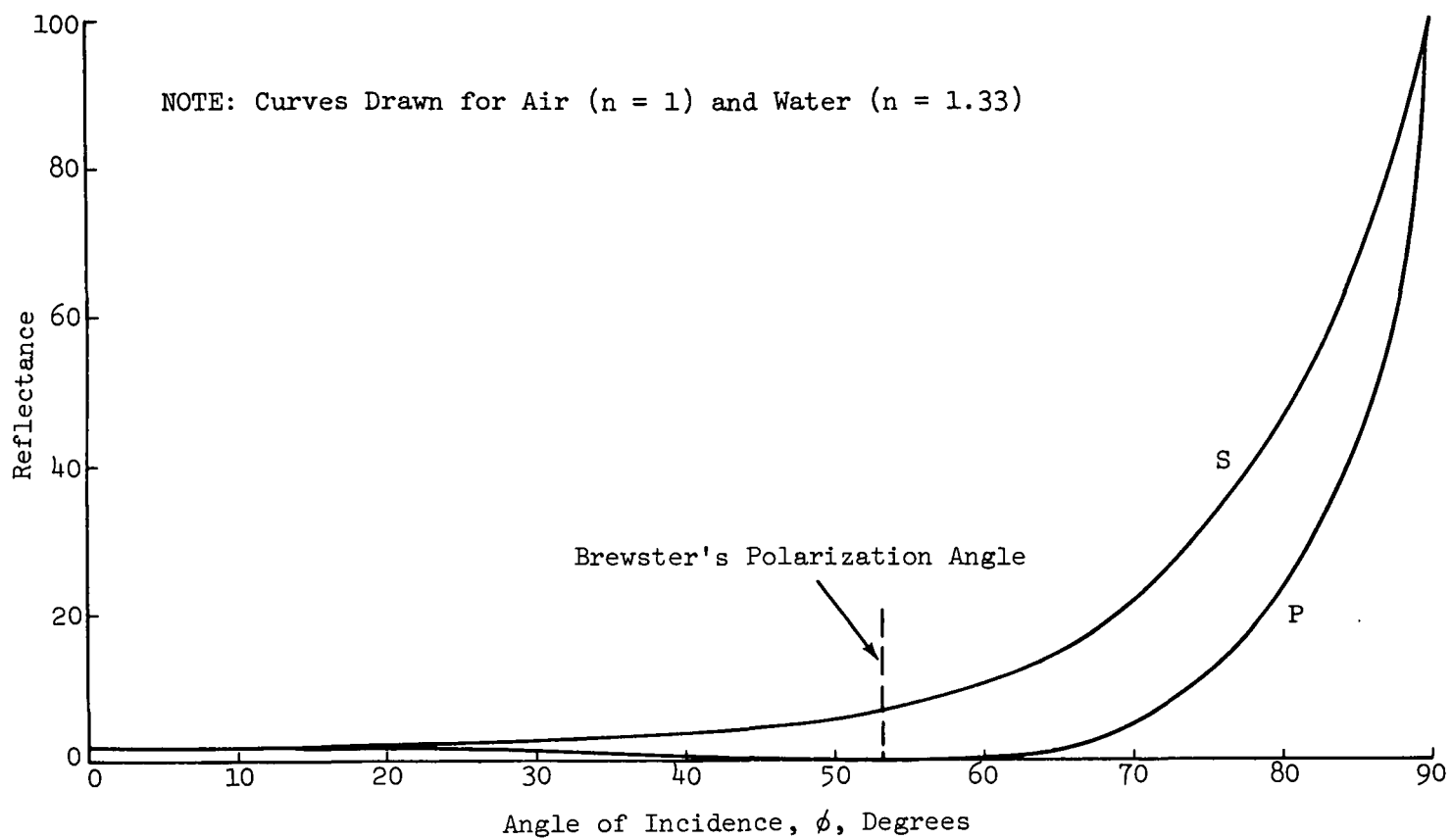
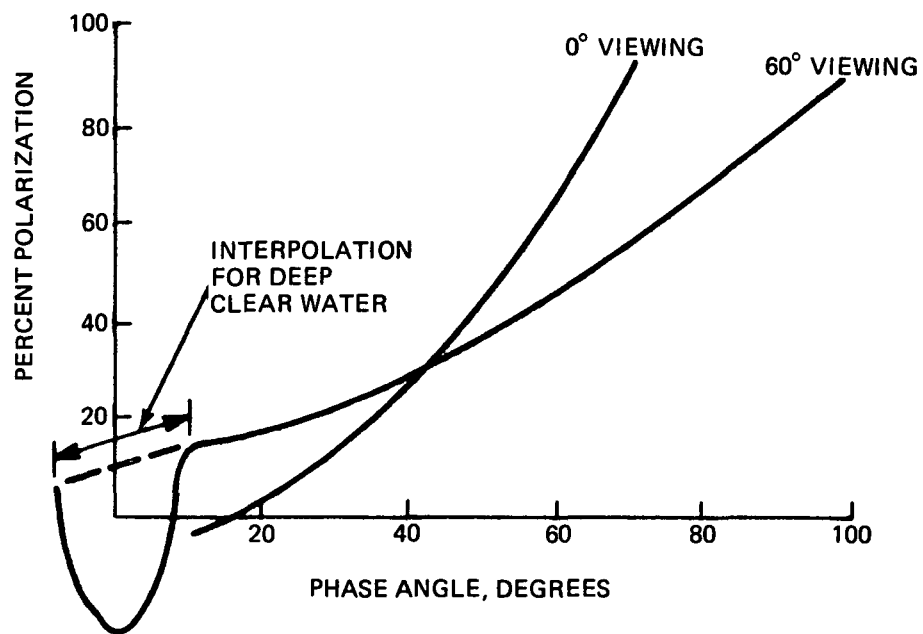Fig. 13 Reflectances of Polarized Components of Water as Functions of ϕ

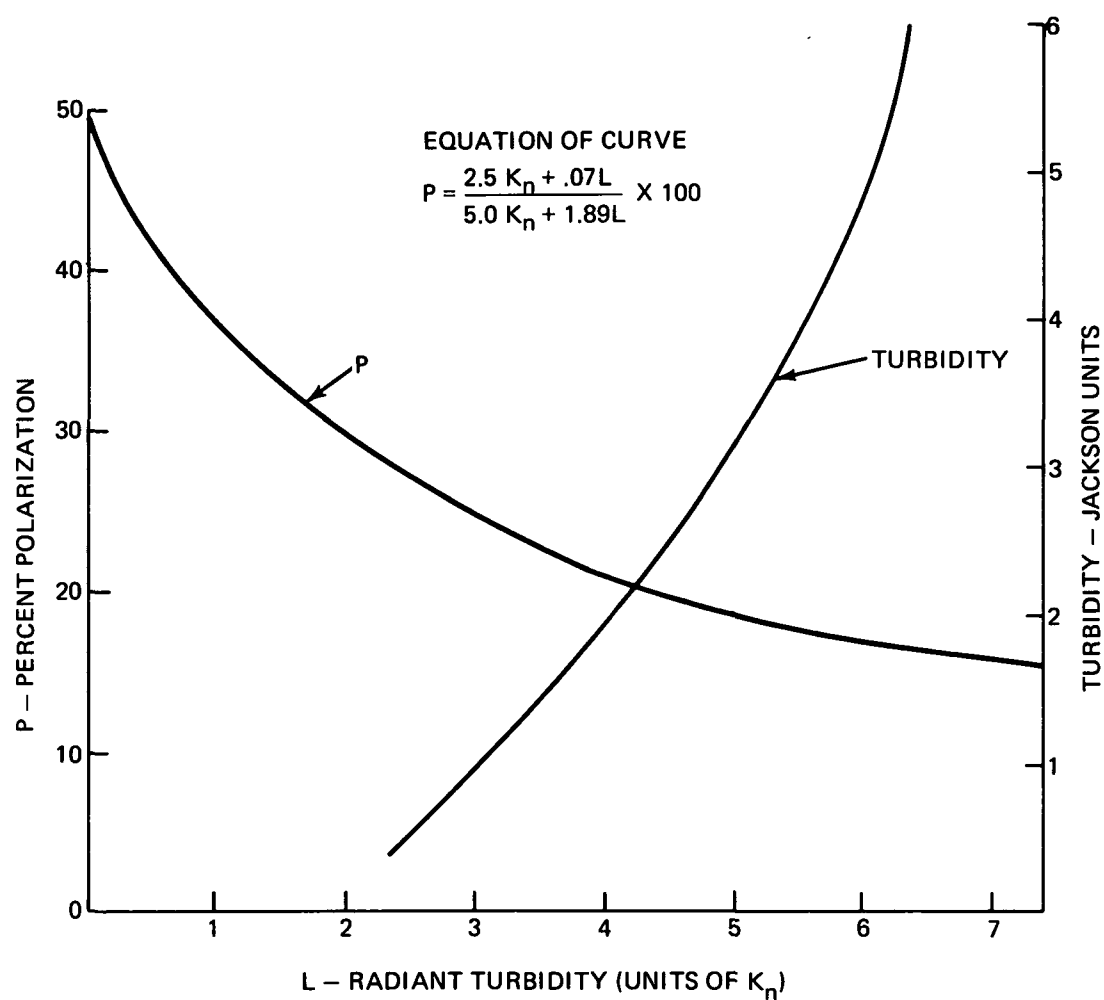Fig. 14 Laboratory Polarimetric Signatures of Clear Water, Hallock et al Ref. (16)

Fig. 15 Polarization — Turbidity Model

DATA ACQUISITION AND PREPROCESSING

1. Airborne Data

The data in this report were acquired during two missions flown with the Grumman Ecosystems A-26 sensor aircraft under an Advanced Development Program. The first mission was flown over Boston area waters on October 8, 1971 and the second mission was flown over New York Metropolitan waters on October 19, 1971.

The Boston flights were part of a week-long experiment staged by the National Ocean Survey Group of NOAA to chart the currents and water quality parameters of the Harbor (Ref. 3). Grumman participation in the experiment consisted of flying the DPM sensor system described in a previous section. The same sensor system was also flown subsequently over New York under more favorable weather conditions to augment the Boston data. A total of five sites was surveyed by the DPM, two in Boston and three in New York as shown in Figure 16. The Boston Sites include the Nantasket Beach area, and a North-South strip across the Harbor over the effluents. The New York Sites include Hempstead Harbor, a heavily polluted body of water on the North shore of Long Island, Fire Island Inlet on the South shore and a strip across Long Island Sound from Throgs Neck Bridge to the Connecticut Shore.

The number and sequence of flights made over the five test sites and the sensor-filter combination used during each overflight is listed in Table I. Not shown in Table I, are preflight and post-flight calibration recordings on dark level output and scan line functions for all combinations of polarizing and special filters used in the field. All flights were made in a "down sun" direction and at a viewing angle of 15° off the normal (away from the sun) in order to minimize solar glare.

In view of the necessity for deriving analytical procedures only a sufficient amount of data is analyzed in this report to illustrate the nature of these and quantitative techniques of data processing and information display. Sites B and E (in Boston Harbor and Long Island Sound) are investigated for turbidity and Site D off Fire Island, N.Y. is investigated for water depth and surface roughness.

The source data stored on digital magnetic tapes were preprocessed as the first step in preparing them for analysis. "Preprocessing" includes: (1) for-

matting the field tapes (for complete computer compatibility). (2) subtracting the dark level output from each data point, (3) correcting each file (representing a flight pass) for tube response non-uniformity according to the appropriate scan line function previously recorded on the calibration tape, and (4) microfilming and hard copy dumping of the corrected numerical data. This step in preparing the data for analysis also includes the development of the rolls of film from the tracking camera as listed in Table I. The landmarks contained in these photographs were used to plot the actual flight path on the USGS or Corps of Engineers maps for each of the flight passes made over the investigated Sites B, D and E.

Fig. 17 shows a typical computer printout of preprocessed two-color data. The data acquired by the second head (NSH) are shown on the first row. They represent in this particular instance the NSH green signature of the water (.49 to .58 μm) along the centerline of the swath scanned by the DPM through a red filter (.58 to .7 μm). The first row represents the first of 226 elements of the scan line. Elements 2 to 26 occupy the masked portion of the image tube and serve as dark level reference. The rest of the elements, 27 to 226 are used by the DPM itself. The data up to element 55 only are shown in Fig. 17. Both color data are expressed in numbers representing radiance values on a scale of 0 to 255, increasing in order of increasing brightness. The theory and procedure for converting these numbers into water depth and turbidity are discussed in following sections.

2. Ground Truth Data

Direct information on solar illumination and sky brightness; and water turbidity and depth was acquired to support or verify the airborne data.

Measurements of solar illumination and sky luminance were made with a ground-based photometer at the South Weymouth Naval Station during the Boston Flights and on the Grumman premises in Bethpage during the New York Flights. The Boston light level records and the timing of five flights over the harbor (Site B, Tape 25) are shown in Fig. 18. As can be seen, these flights took place during the early stages of patchy cloud foundation. In this report we analyze Flight Pass No. 3 data only. According to the record in Fig. 18 solar illumination during this flight corresponds nearly to a cloudless condition

and is fairly steady. Sky luminance shows a 15% increase from the beginning
to the end of the flight. However, this increase is not of great consequence
to our data. The New York records, not shown in this report, were taken under
clear sky conditions.

Information on turbidity was obtained from water samples secured in the
field during or shortly before the flights and analyzed in our laboratory. The
Boston samples were taken by an MIT crew working under NOAA auspices and deliver-
ed to Grumman by NOAA for analysis. Of the three Sites in New York, only Hemp-
stead Harbor was sampled. A total of about one hundred samples of water was
analyzed, one third of which came from Hempstead Harbor and the rest from
Boston. Since only Boston Harbor data are analyzed in this report, the results
of the analysis of water samples coming from that area are shown in Table II.
These samples were analyzed for turbidity and color. Turbidity is expressed in
Jackson Units (J.U.), and color is expressed in Chloroplatinate Units (C.P.U.)
according to standards described in Appendix B.

Correlation of our depth computations for the waters off Fire Island (Site
D) are based on published Coast and Geodetic Survey maps and the latest (1969)
unpublished sounding data supplied by the U.S. Army Corps. of Engineers. In
the case of Boston Harbor the depth information (taken from C.&.G.S. map No. 246)
is used as a known input to solve the appropriate equations for the parameters
of water quality.

TABLE I

AIRBORNE DATA

DPM Tape No. and Date	Survey Site	Flight Pass	Filters DPM	Filters 2nd Head	Hasselblad B&W Photos Roll No.	Hasselblad B&W Photos Frame No.	Local Time From	Local Time To	Altitude Ft	DPM Resolution Ft x Ft	Weather
24	A	1	HD	HR_2	61-1	19-29	1027	1028	3000	4 x 4	
		2	VD	HR_2		30-41	1035	1036			
10-8-71		3	VD	VGr		42-56	1045	1047			Clear
		4	VBL_1	VGr_2		57-71	1054	1055			
		5	VGr_1	VGr_2		72-85	1102	1104			
25	B	1	HD	HR_2	62-1	1-20	1300	1303	3000	4 x 4	
		2	VD	HR_2		21-38	1310	1312			Light
10-8-71	B	3	VD	VGr_2		39-54	1320	1323			Clouds
		4	VBL_1	VGr_2		55-69	1330	1332			
		5	VGr_1	VGr_2		70-88	1342	1346			
28	C	1	VBL_1	VGr_2	64-1	1-13	1133	1135	2500	3.4 x 3.4	
		2	VGr_1	VGr_2		14-27	1141	1143			
10-19-71		3	VD	VGr_2		28-47	1151	1153			Clear
		4	VD	HR_2		48-62	1201	1205			
		5	HD	HR_2		63-83	1213	1217			
29	D	1	HD	HR_2	62-2	1-9	1241	1244	1500	2 x 2	
		2	VD	HR_2		10-17	1247	1249	1249		
		3	VD	VGr_2		18-29	1254	1256			Clear
10-19-71		4	VBL_1	VGr_2		30-39	1300	1301			
		5	VGr_1	VGr_2		40-47	1305	1307			
		6	VR_1	VGr_2		48-58	1311	1312			
29	E	1	HD	HR_2	64-2	59-79			2500	3.4 x 3.4	Clear
		2	VD	HR_2		80-93					

NOTES:

- Aircraft ground speed = 125 knots

- H and V are polarizing filters. Bl, Gr, D and R are spectral bandpass filters as defined in Fig. 5. Filters VD, for example, mean filter V plus filter D

TABLE II

BOSTON HARBOR WATER SAMPLE ANALYSIS

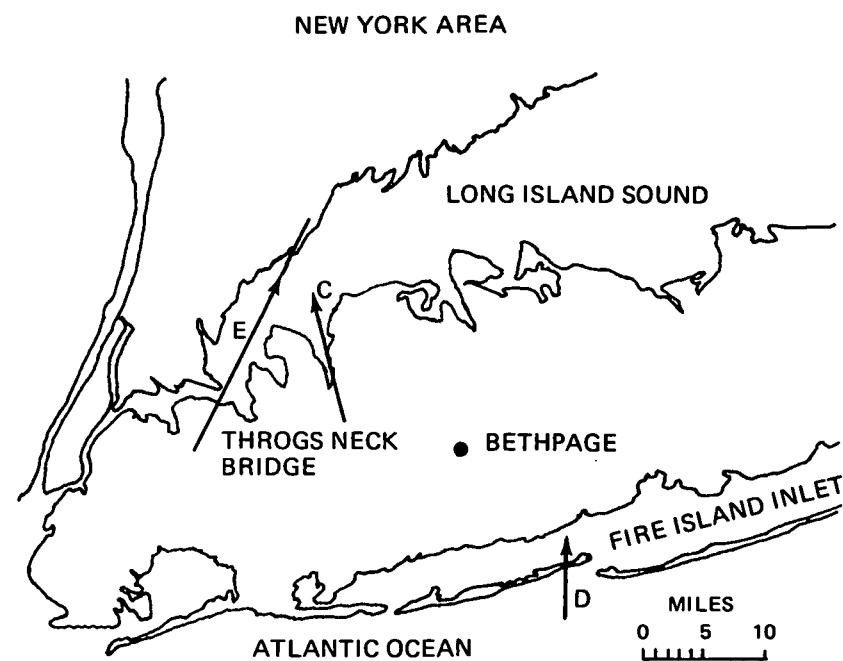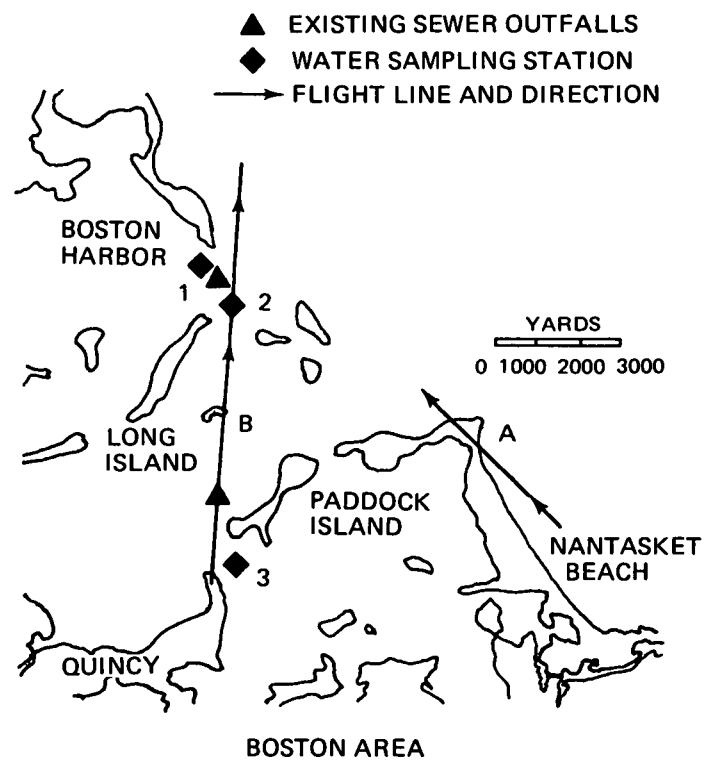| Sample No	Turbidity J.U.	Color C.P.U.	Dept ft	Time	Location
273	7	1.0	2		
274	7	1.0	2		Station 1
275	10	1.5	2	9 to	
276	7	1.0	2		
277	4	.2	10	12:30	
278	4	.5	20		
279	7	.5	2		
280	4	.5	10		President
281	4	.5	20		Roads
282	4	.5	20		
283	7	.5	2		
649	13	1.5	2		North
651	14.5	7.5	2	12:30	
652	30	4.5	2		
653	40	2.5	2	to	
654	4	4.5	10		
656	2.5	2.5	20	13:30	
657	2.5	4.5	20		
658	0	4.5	20		
670	4	.5	10		
423	10	1.5	2	10:30	Station 2
424	10	2	2		
425	10	1.5	2		
426	10	2.0	2	to	President
427	13	1.5	2		
428	10	1.5	2		Roads
429	8.5	1.5	2		
430	13	1.5	2	14:00	South
308	10	1.5	2		
309	10	1.5	2	9:00	Station 3
310	10	1.5	2		
311	10	1.5	2	to	
312	8.5	1.5	2		Between
529	7	1.5	2	11:00	
530	7	1.5	2		Peddocks
531	4	1.5	10		
532	4	1.5	20		and
444	5.5	1.0	2	11:00	
445	5.5	1.0	2	11:30	Nut
446	5.5	1.0	2	12:0	
447	5.5	1.0	2	12:30	Islands
448	5.5	0.5	2	13:00	
449	4.0	0.5	2	13:30	

NOTE: See Fig. 29 for location of Stations

Fig. 16 Survey Sites

SCAN LINE NO.

NON-SCANNING
HEAD DATA
(GREEN FILTER)

DARK LEVEL

SCANNING
HEAD
DATA
(RED FILTER)

SCANNED AREA

15°

Fig. 17 Typical Computer Print-Out of Preprocessed Two-Color Data

Fig. 18 Solar Illumination and Sky Luminance

DATA ANALYSIS

I. WATER DEPTH: SPECTROPHOTOMETRIC ANALYSIS OF FIRE ISLAND WATERS.

The first step in the analysis for water depth is to correct the data for surface effects. This includes 1) the determination and subtraction from each data point of the reflection of the surface, and 2) indentification and smoothing of transient surface perturbations due to random waves and long-period swells.

Molecular, particulate and surface derived radiances constitute the parameter K in equation (1). In this analysis it is assumed to be constant throughout the length of the survey site and equal to the radiance level of deep water. It is determined by extending the flight far enough offshore so that the bottom no longer contributes to the measurements.

Fig. 19 shows brightness profiles measured by the DPM along the entire flight path for five successive flights with varying spectral and polarizing filters (see Site D, Flights 2 to 6, Table I)* The radiance values are the average for a scan line consisting of 200 data points. The profiles taken at a few minutes interval from each other are quite similar except for transient surface features such as white caps represented by spikes. All profiles show a ditch and a shoal near the shore followed by two prominent humps between scan lines 600 and 800 (about 12,000 feet from the shore). A photograph of the shoal taken by the tracking camera is shown in Fig. 20. Towards the deep end of the profile the radiance values stabilize at about 50 and 100 binary units for the red and green data respectively. These values were tentatively adopted to represent K_R and K_G.

1. Screening Out Surface Effects

The screening out of environmental noise due to waves and swells is carried in two steps, one for smoothing small-scale random waves and other noise and the other for smoothing long-period swells.

For the first step a "statistical smoothing" technique is used. The 200 element wide swath is divided into 39 strips 5-element wide each, one strip along the centerline of the swath and 19 strips on each side of the center strip. As shown in Fig. 21, the highest two numbers out of 5 in each column are stricken out and the remaining three numbers are averaged. The same procedure is re-

* The trace from Flight 1 is not shown because it was slightly off-course.

FLIGHT PASS	DPM FILTER
2	VD
3	VD
4	VBP_1
5	VGr_1
6	VR_1

WHITE CAP

SHOAL SEE FIG 20

SHORE

SCAN LINE NO.

60   330   600   870   1140   1410

RADIANCE VALUES (TYPICAL FOR ALL TRACES)

250 –
200 –
150 –
100 –
50 –
0 –
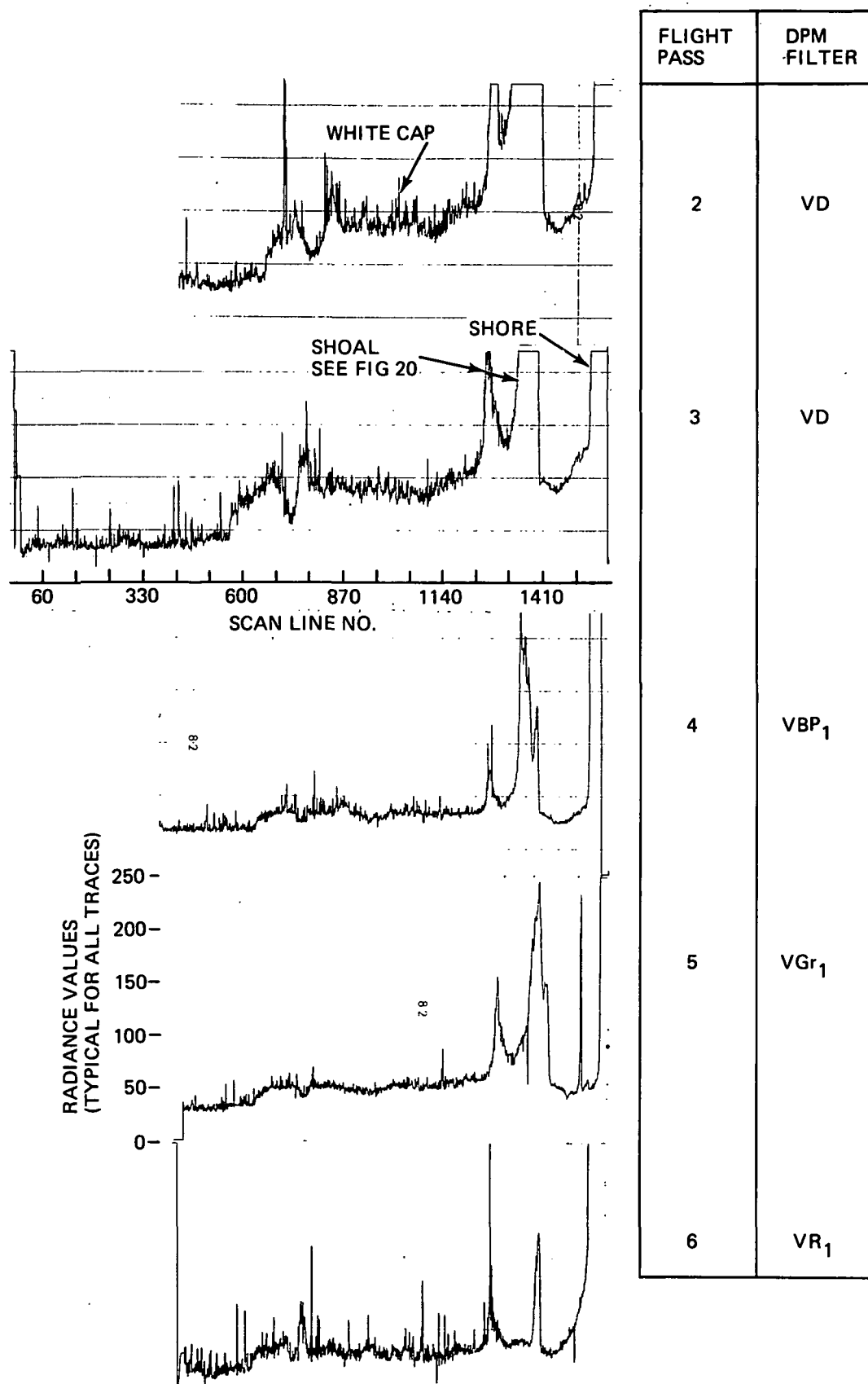
Fig. 19 Flight Path Radiance Profiles Site D, off Fire Island. Unsmoothed Data.

63

DITCH

DPM ₵
@ SHOAL
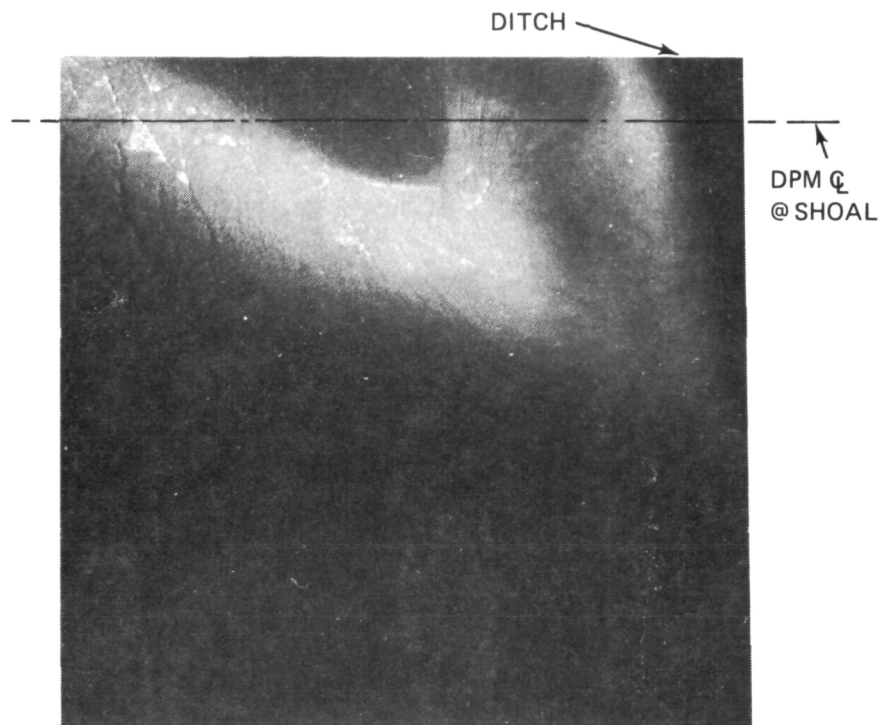
Fig. 20 Tracking Camera Photograph of Near-Shore Shoal (Site D)

peated for the next 5-element column. It is reasoned that the high numbers may be spurious being due to sky glint reflected by the wave facets, or by white caps and that in discarding them more weight is given to the low numbers which are more representative of the reflectance of smooth water.

Actually, the discarded high numbers rarely exceed 10% of the average. A typical example of the statistical smoothing process is illustrated in Fig. 21 in numerical and graphical form for the DPM center strip and the second head. In the numerical example shown the DPM averages of 114, 113 and 108 in the red correspond to the second head reading of 182, 171 and 176 in the green. The sensor-aircraft imagery parameters are such that the width of the swath of five DPM elements is approximately the same as covered by the 13 ft. diameter of the second head. The fact that the output of the two sensors track each other indicates that the random variations are due to an external input rather that to system noise. The registration of the two sensor outputs is more clearly evident along the profile of the entire flight path shown in Fig. 22.

In the second step a "logarithmic smoothing technique" is used to screen out the long-period swells which are identified by their periodicity. Fig. 22 shows the two-color logarithmic radiance profiles along the center strip, one in the red, measured by the DPM, and the other in the green measured by the second head. Both profiles have been smoothed according to the technique described above. The ordinate represents the radiance level on a logarithmic scale after the surface reflectance components, K_R and K_G, have been subtracted out. The abscissa represents distance from flight origin toward shore in terms of scan line numbers. Distance between scan lines is about 14 ft. The deep trench and the shoal near the shore featured originally in Fig. 19 are not shown in Fig. 22 due to space limitation.

The rationale for "logarithmic smoothing" is to balance the volume of water in the crest of the wave above mean level with the volume in the trough below. Since the actual ordinate distances on the semi-log plot in Fig. 22 are proportional to distances in feet, the smoothing is accomplished by equating the area under the peaks above the smoothed curve with the area in the valleys below. One graphical procedure for smoothing is illustrated on the upper left corner

of Fig. 22. The original profile is first enclosed between two envelopes joining the inflection points of the peaks and valleys. Then from points midway between the two envelopes the smoothed curve is drawn in such a manner as to make the plus areas equal to the minus areas.

Obviously the surface waves, or cycles, occur in various periodicities, many times quite intermingled. The smoothing of the periodic changes of relatively high spatial frequency leaves those of lower frequency more prominently displayed. It is logical to assume that the smoothing can be accomplished best by successive applications to screen out surface perturbations of lower and lower spatial frequency. Obviously, however, there must be a pragmatic rule for cutting off these successive smoothings in order to prevent the smoothing of bottom details, thus degrading the information which is to be extracted. Appropriate criteria can probably be developed from wave and swell statistics. For the purposes of this study the following somewhat arbitrary assumptions were made:

1. In shallow water (i.e. less than 30 ft. depth) cycles whose wavelength exceeds 400 ft are not to be smoothed.

2. In intermediate depths (i.e. 30 ft. to 45 ft.) cycles whose wavelength exceeds 600 ft. are not to be smoothed.

3. In deep water (i.e. deeper than 45 ft. all cyclic phenomena are to be smoothed)

This logarithmic smoothing is shown to be applied in two successive stages. The result of the first, shown in Fig. 22, brings out more clearly the periodicity and the amplitude of the swells which are particularly pronounced over the deep end before they reach the sharp rise of the sea-floor around scan line No. 550. Beyond this point the swells are more subdued as they approach the shore. The red and green profiles resulting from the second stage smoothing are shown in Fig. 23. They represent the residual radiance levels due to the reflectance of the bottom attenuated by the passage of light in traveling to and emerging from the bottom through water of depth d. The equations derived in a preceding section can now be applied to compute the attenuation coefficient $(\alpha + \beta)$ and depth d.

| SCAN LINE NO. | 2 4 6 8 10 12 14 16 18 20 22 24 26 28 30 | 23 | 24 | 25 |

200 — RAW DATA

NON-SCANNING **190**
HEAD, GREEN
FILTER — SMOOTHED DATA

| | 182 | 171 | 176 |

180

GREEN FILTER

AVERAGE 176

170

160

|← 400 FT. →|

120	118	109
116	113	110

130
SCANNING HEAD,
RED FILTER

| 114 | 113 | 112 |

120

| 111 | 116 | 109 |
| 122 | 113 | 107 |

110

| 114 | 113 | 108 |

100

AVERAGE 112
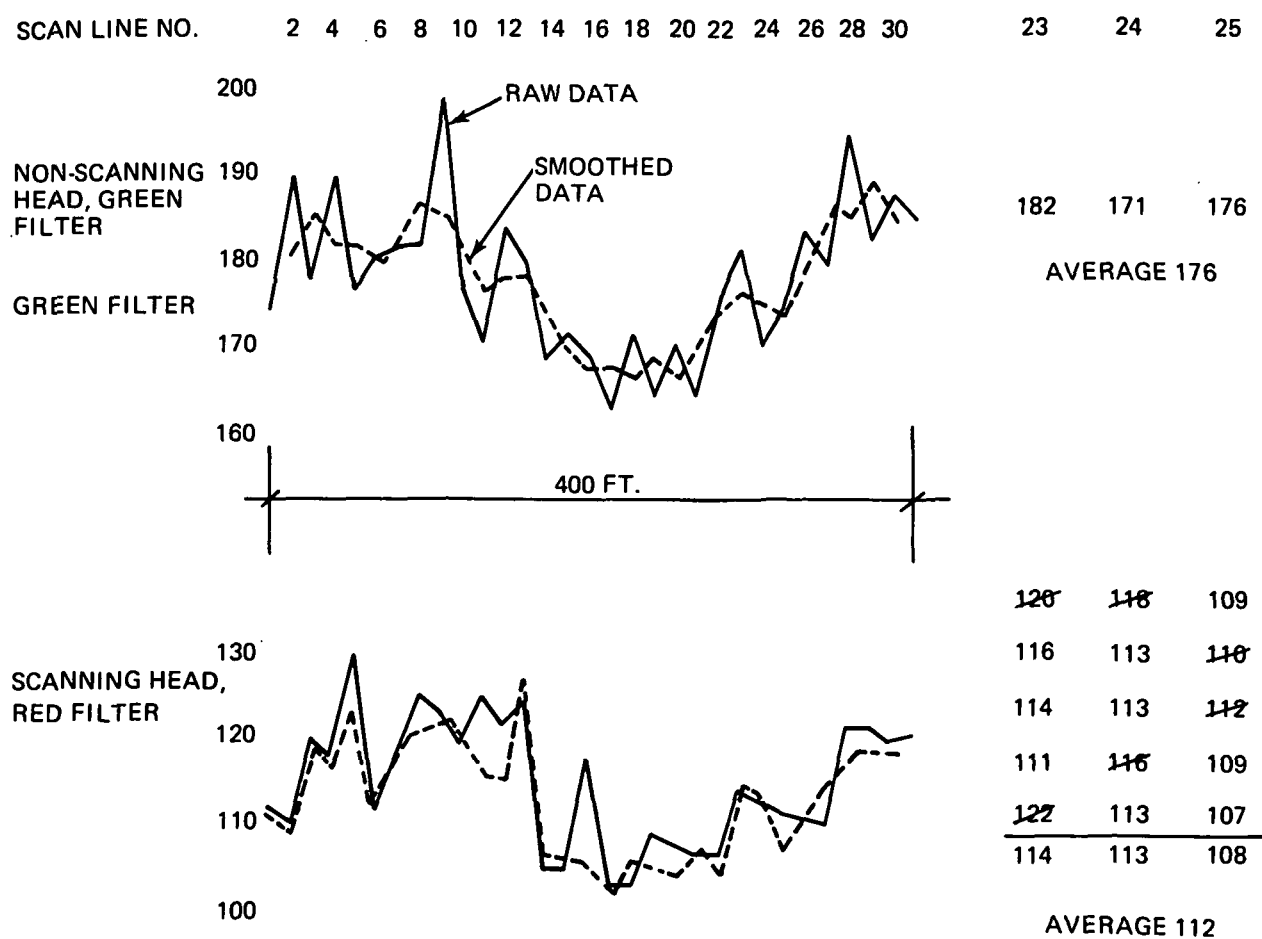
Fig. 21 Example of "Statistical Smoothing"
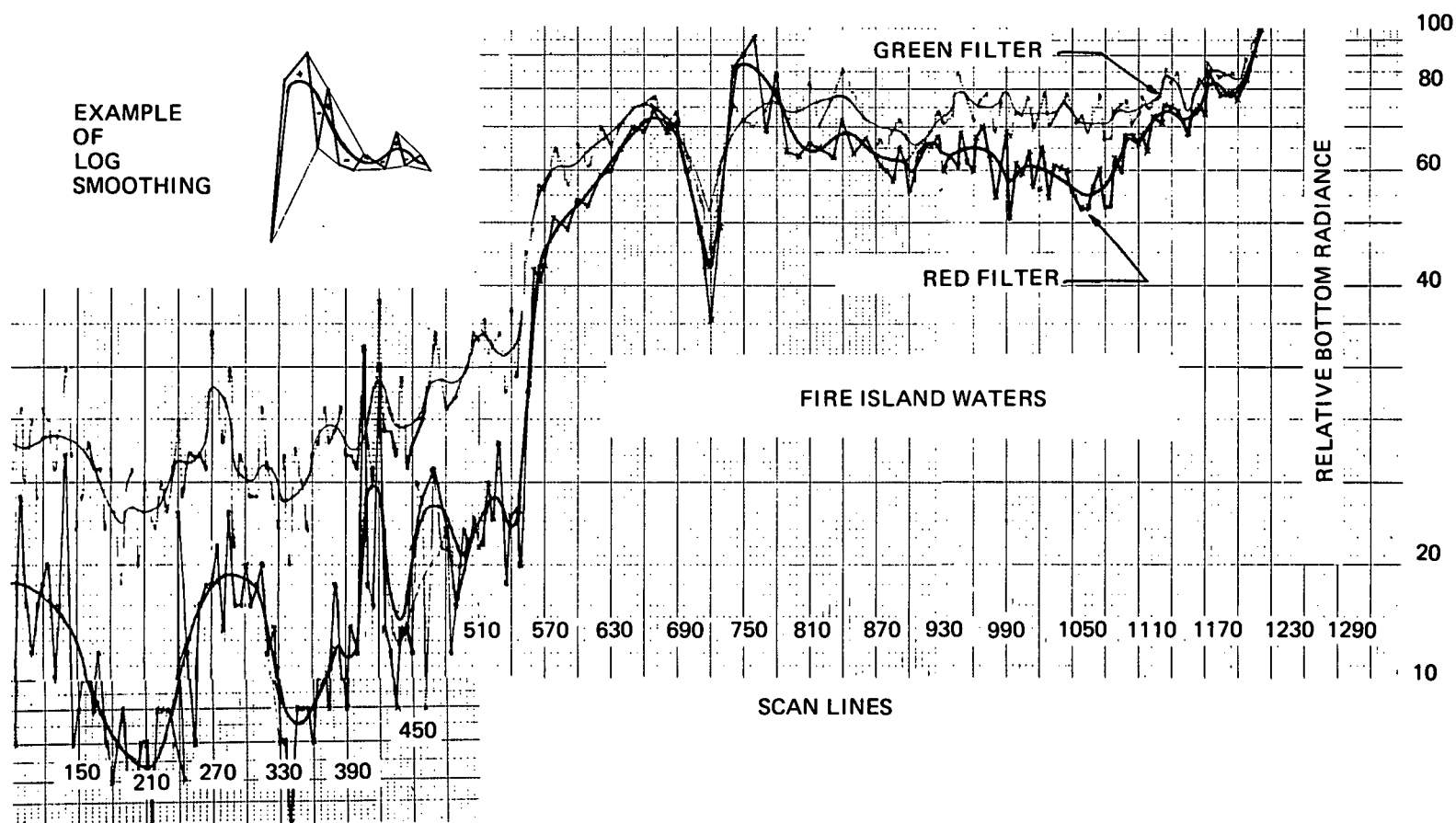
Fig. 22 Red and Green Radiance Profiles Along Swath ₵

EXAMPLE
OF
LOG
SMOOTHING

GREEN FILTER

RED FILTER

FIRE ISLAND WATERS

RELATIVE BOTTOM RADIANCE

100
80
60
40
20
10

SCAN LINES

510 570 630 690 750 810 870 930 990 1050 1110 1170 1230 1290

450

150 210 270 330 390
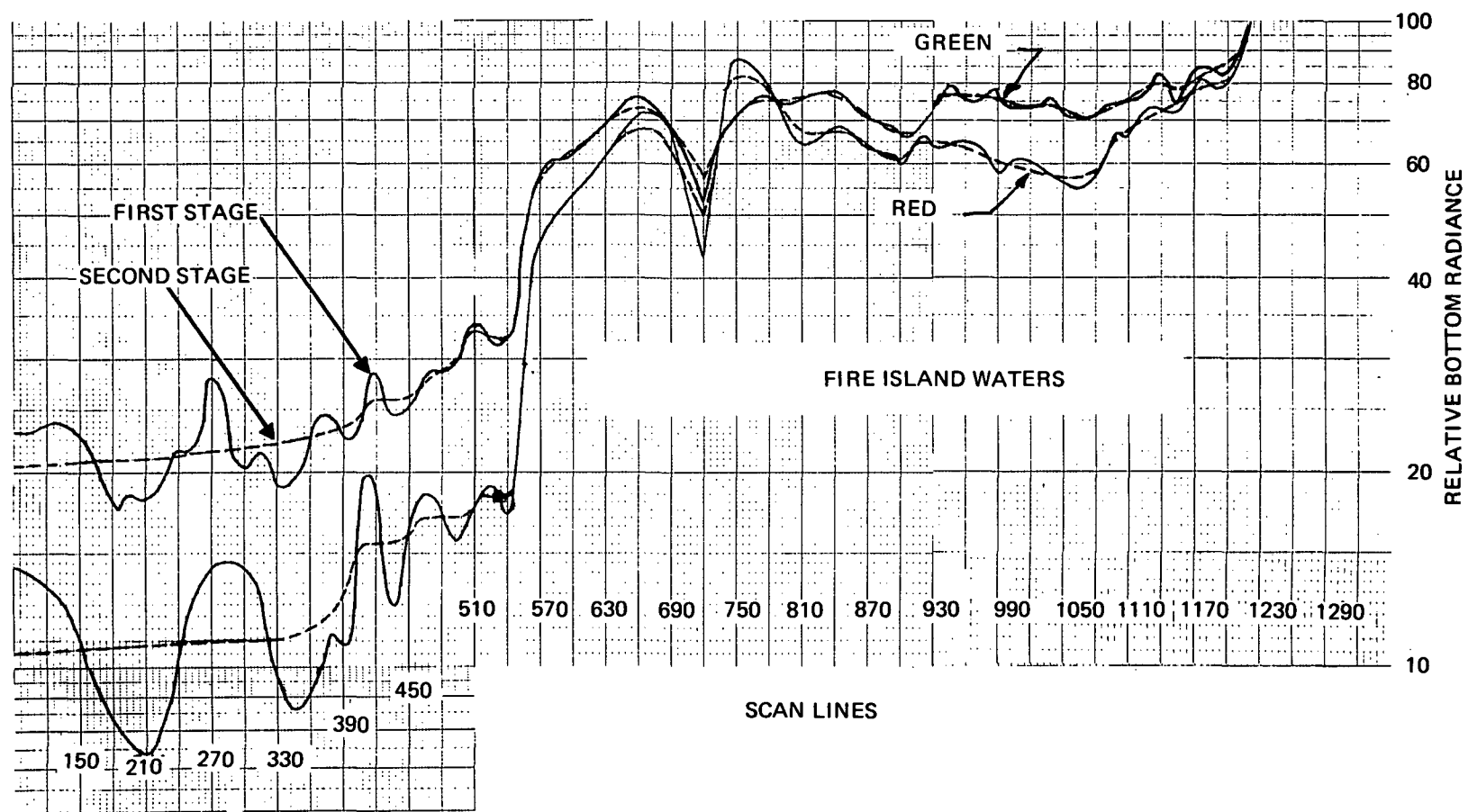
Fig. 23 First and Second Stage Logarithmically Smoothed Radiance Profiles

2. Two-Color Analysis of Water Turbidity and Corrected Logarithmic Scaling

In this section we apply the previously developed theory to reduce digital radiance data into water depth after the routine pre-processing and smoothing has been performed.

Figure 23 shows a major portion of the data in shape for analysis. The red (R) and green (G) radiance profiles are shown plotted in semi-logarithmic format. As will usually be the case a close "guess" has been made at K_R and K_G, and these values have been subtracted from the original measurements in order to get started with the analysis. A more precise determination of K_R and K_G needs yet to be made. One cannot ignore the possibility that fluctuations in these values over the area of surveillance may be serious enough so that a uniform substraction cannot be made. Over beach areas exposed to the dynamic influences of water in motion it appears possible in most cases to ignore the fluctuations. However, the increasing volume of waste and detritus in the coastal waters may make this generalization invalid.

Our experience with mapping depth in these coastal waters does point up the necessity of taking account of zonal variations in attenuation coefficient $(\alpha + \beta)$, even if we have seen fit to discount the K-value changes which may, in minor degree, be associated with these turbidity-related phenomena. One of the principal problems in putting an accurate depth scale on the data lies in the increasing attenuation of light by turbid water at shallow depths near the shore. Without correction the lowered radiance in these areas may be mistaken for a greater water depth. In our example, Figure 23, this effect must be compensated in the region from about scan line 1150 toward shore.

We find other examples of anomalously high attenuation in the flight strip which must be compensated. The most prominent example is the shoal-like feature beginning at about scan line 500 and extending to about scan line 700. The leeward exposure of this shoal appears to be covered with water of anomalous turbidity, probably sedimentary in origin, stirred up by the dynamic effects of the water. There are other lesser examples of anomalous turbidity in the strip which we will not discuss in detail.

Our method of analysis of the airborne data to extract values of $(\alpha + \beta)$ is that of multi-color photometry (two-color in this case). For the most part the

analysis consists of the application of equation (7) to the relative slopes of the R and G data plotted with a logarithmic ordinate scale.

We have found that several precautions must be observed. First the data must be properly smoothed to remove surface perturbations and similar extraneous fluctuations. Even after this smoothing there remain what seem to be inconsistencies. Some of these inconsistencies can be explained by variations in K-values. Since these variations are few and "spotty" they can be ignored in looking for trends. Similarly, bottom reflectance anomalies are not usually too troublesome in coastal beach areas. Of more serious consequence is the fact that when a "trend" is explored over several thousand feet, or over the whole strip, the anomalous behavior due to strong attenuation in turbid areas distorts the appearance of the trend. Therefore, the analysis must begin by examining relatively short (but not too short) sections of the profile (typically about 1000 feet). On the basis of these short-section analyses a tentative line-of-flight plot of $(\alpha + \beta)_G$, and $(\alpha + \beta)_R$, can be made. For "clear" coastal water a $\gamma_{R/G}$ value of 1.5 to 2 is indicated.

It is desirable to construct a first approximation of depth profile by use of equation (5) and (6) based upon extraction of K-values, and $(\alpha + \beta)$ values from the data. It is our experience that construction of such an initial estimate based upon the parameters of clear coastal water; i.e. $(\alpha + \beta)_G = .02$, $(\alpha + \beta)_R = .04$; is warranted for most beach areas beyond 15 ft. depth. Closer to shore it is preferable to use far red (FR) data. Use of this preliminary depth estimate allows sampling application of equation (7) and (24) to determine the general consistency of the trends in the data. Also, since the R and G bands are wide, monochromatic values of $(\alpha + \beta)$ do not apply and a general idea of depth must be used in order to employ the correct curves (see Figures 7 and 8).

The use of far red (FR) data for preliminary construction of a depth profile near shore may be a valuable technique since the percentage uncertainty is less than in shorter wavelength data.

The process of correcting a profile for anomalous attenuation coefficient can best be described by an example. First, it has to be decided what is the "norm" of values of $(\alpha + \beta)$ for the area. The profile will then be corrected to indicate radiance (or log radiance) values which would have been measured if the water were uniformly of this characteristic attenuation. As a general rule the

norm will be $(\alpha + \beta)_G = .02$ $\log_{10}$ ft^{-1}; $(\alpha + \beta)_R = .04$ $\log_{10}$ ft^{-1}.

Let it be assumed in the example that the profile between a point in clear water $(\alpha + \beta)_G = .02$ and a point closer to shore in more turbid water $(\alpha + \beta)_G = .04$ is to be corrected. The actual measured increase in $\log_{10}$ $(G-K_G)$ from point 2 to point 1 is .16. Also preliminary scaling of red (R) or far red (FR) data indicates a depth of approximately 8 ft for d_1. The value of Δ to be substituted in equation (21) is .04 - .02 = .02 $\log_{10}$ ft^{-1}. In accordance with equation (21) the correction to be added to .16 is 2 f (.02) x 8 = .32f. For f = 1, the re-scaled $\log_{10}$ $(G-K_G)$ increment from point 2 to point 1 is .32 + .16 = .48 which is actually three times the measured increment. Thus the scale is affected tremendously in areas such as this and it becomes easy to make large errors.

Fortunately there is a criterion of satisfactory fit which can be applied to the corrected multi-color profiles. The slope ratios, or γ-values, must be consistent. Until they show the necessary consistent quality the correction can be made in an iterative process using successive refinements of depth estimate and $(\alpha + \beta)$ to bring the multiple-color profiles into agreement. This type of refinement is illustrated in Figure 24 which shows our original data corrected and scaled between about 4000 feet and 6500 ft from shore. The γ-value between the G and the R slopes is 2, which would apply to uniform clear coastal water. The $(\alpha + \beta)$ vs. depth relationship shown in this Figure both in the green and the red was developed during the analysis in an attempt to reconcile the two-color data to the γ relationship shown in Figs. 7 and 8.

Obviously the validity of this correction depends strongly on the accuracy of the original data, and on a close attention to detail. The use of a computer for iterative correction processes like a "trial and error" approach would probably result in depth analysis of satisfactory accuracy and would have been eminently successful in satisfying naval-type requirements such as motivated Moore, et al (4).

Figure 25 shows the complete profile which was arrived at by the corrective and scaling processes described above. The K_R and K_G values originally subtracted from measured radiances were 50 and 100 respectively. Final analysis resulted in the subtraction of additional values of 11 for K_R and 19 for K_G making the total K-values 61 for K_R and 119 for K_G.

Figure 25 also shows the "ground truth" information on water depth based on published marine maps and more recent (1969) soundings by the US Army Corps of Engineers. The aerial measurements agree with the soundings in the shoal and trench area near the shore but depart significantly further offshore, indicating a higher sea floor. There is evidence in our data that the two prominences at about 14,000 and 11,000 feet from the shore are real. They are too large to be mistaken for swells. Furthermore, they were detected in all five successive flights that were made over the same area as shown in Fig. 19. The two humps are prominently featured in all profiles whereas the sharp spikes (due to white caps or swells) recorded during a given flight are not picked up during the other flights. The two-color analysis described in this section indicates a higher level of turbidity for this region than the norm for the area surveyed which is close to clear coastal water. A profile of the large swells on the offshore side of the humps is also shown in Fig. 25.
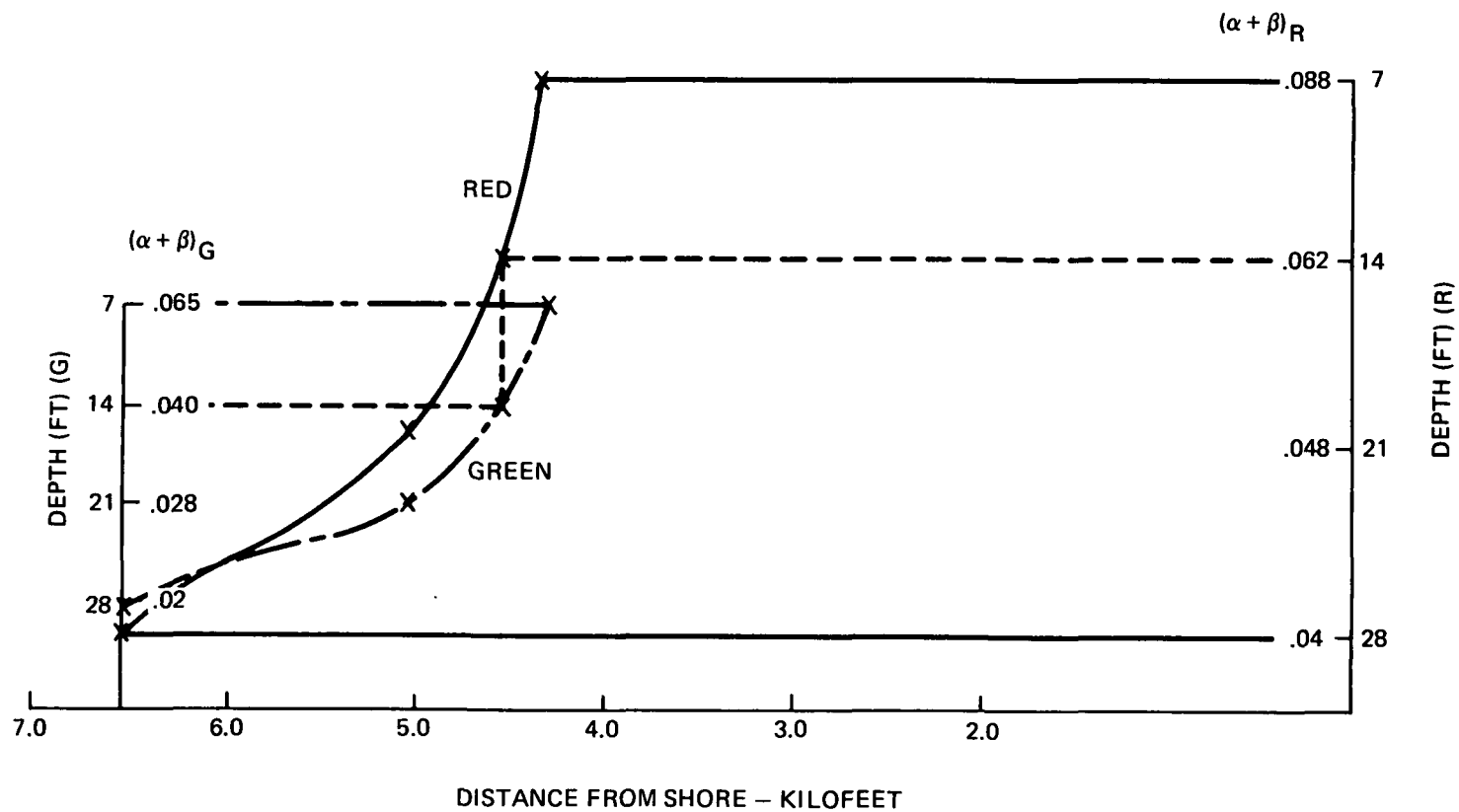
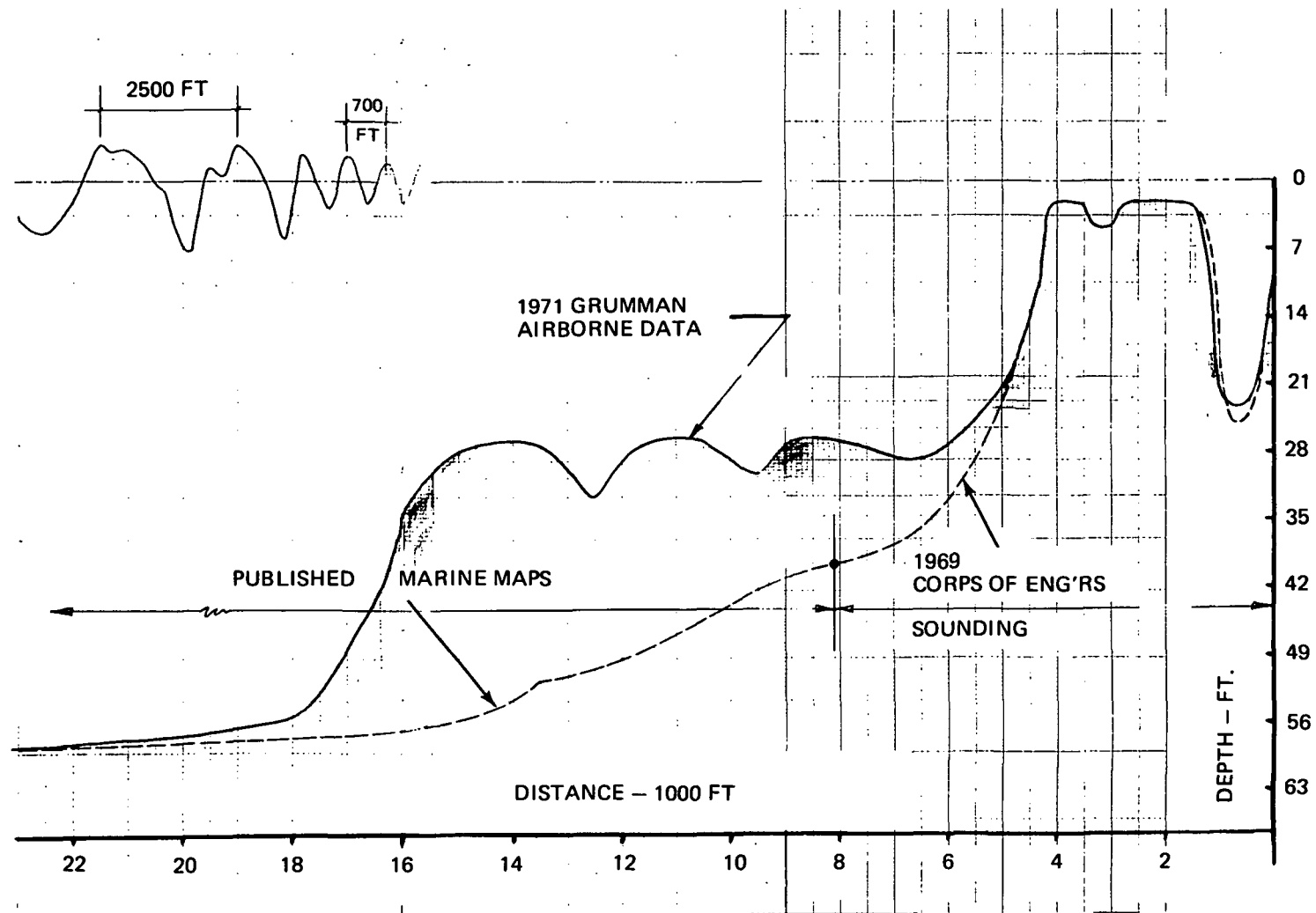**Fig. 24 Logarithmic Scaling Correction for Anomalous Turbidity**

Fig. 25 Surface Wave and Water Depth Profiles Along Swath C

74

3. Computer Generation Of A Water Depth Map

In order to generate a depth map with the DPM - approach it may be assumed that the extinction coefficient of water across the width of the swath is uniform and is equal to the value computed for the center strip according to the method described in the previous section. This assumption is reasonable in view of the fact that the extinction coefficient of typical coastal waters is not likely to vary much over a distance of a few hundred feet.

Complete automation of the compilation of water depth maps by the computer is feasible but would require more extensive software than can be justified at this time. However, a sample computer output of such a map is presented in this report based upon semi-automated techniques in which the "logarithmic smoothing" and the display of surface wave conditions are worked out manually.

The following procedure was used in order to simplify the manual phase of data reduction in preparing the bottom and surface maps illustrated in Figures 26 and 27. A portion of the swath between scan lines 500 to 600 was selected in an area about 16,000 ft. from the shore (see Figure 25 for location). The selected matrix consisting of 196 data points across track by 100 points along track was divided into 39 longitudinal strips of 5 x 100 submatrices, one strip along the center of the swath and 19 strips on each side of the center. A computer program was written to perform the following operations: 1) statistical smoothing, 2) subtracting the K_R constant from each data point and converting the results into logarithmic values, 3) applying the proper scaling factor to correct for changes in extinction coefficients derived in the previous section from the two-color signature of the center strip and, 4) outputting on microfilm and hard copy all 39 profiles. The manual part of the operation consisted of the logarithmic smoothing of 13 out of the 39 profiles. This was done by projecting the machine-plotted microfilmed profiles on the screen of a Benson-Lehner plot digitizer. The smoothing by hand was done in two cycles according to the technique illustrated in Figures 22 and 23. The 13 smoothed profiles were then digitized, stored on punch cards, fed back to the computer and printed out in numerical form where the numbers represent depth in feet as shown in Figure 26. The plotting of the four foot interval contours in this figure was done by hand but could also be automated and the results be displayed either as contour lines or gray shaded areas. This map does not do justice to the

amount of bottom details the the DPM is capable of showing since its spatial resolution was coarsened by a factor of 30 in order to simplify the data reduction.

An isometric view of the same bottom contours is shown in Figure 27 superposed with a similar view of the surface wave conditions. The amplitudes of these waves are numerically equal to the difference in the ordinates of the smoothed and unsmoothed profiles. Some of these amplitudes are probably exaggerated as they may be enhanced due to white caps of higher reflectivity. Notice however, that in Figure 27 most of the wave activity is taking place on the offshore side of the underwater bluff, suggesting that the bluff is acting as a breaker where ocean swells of large amplitude are damped. A photograph of the wave activity in this area taken by the tracking camera is shown in Fig. 28.

The illustration in Fig. 27 is hand drawn and is based on hand computation. However, computer graphic techniques could be applied to expedite the processing and display of the information. Examples of such displays (in shaded contour or in isometric form) may be found in Appendix D of Ref (1).

Fig. 26 Sample Water Depth Map Showing Numerical
Computer Print-Out and Hand-Drawn
Contours in Feet
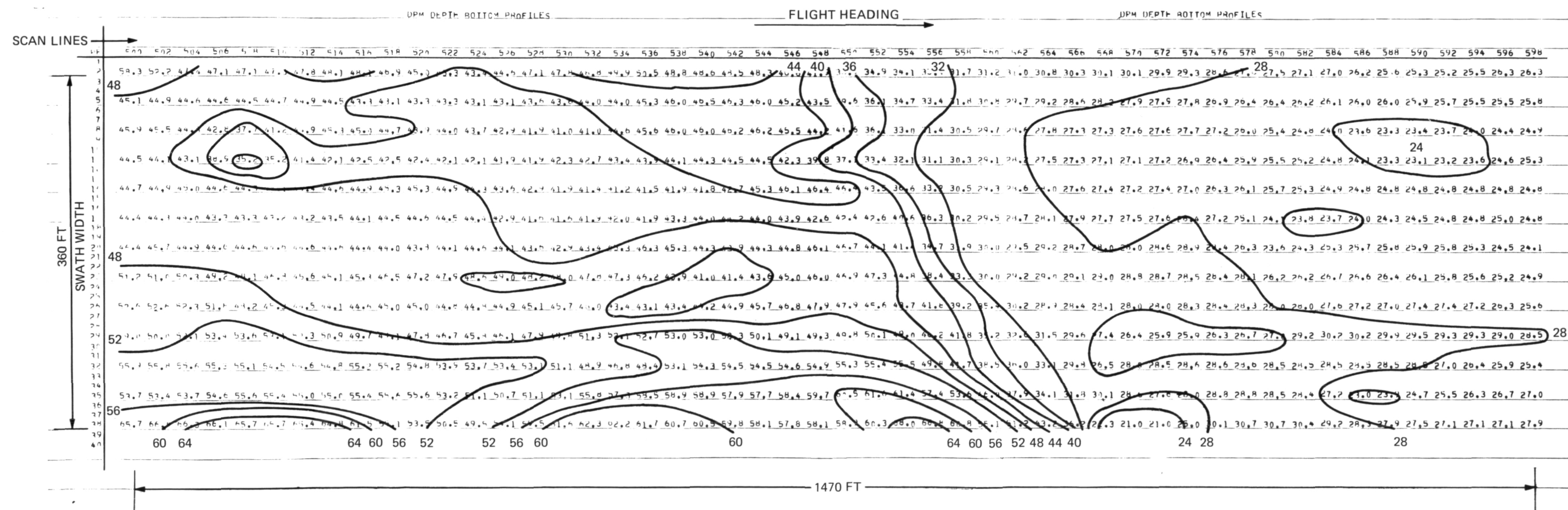
SPATIAL RESOLUTION = 30 FT x 30 FT
COARSENED FROM ORIGINAL RESOLUTION OF 2 FT x 14 FT

FLIGHT HEADING
TO SHORE

360 FT

SWATH WIDTH

1500 FT

SURFACE FEATURES

MEAN WATER LEVEL

32

40

DEPTH,
FT

48

56

BOTTOM TOPOGRAPHY

— — — CROSS SECTION
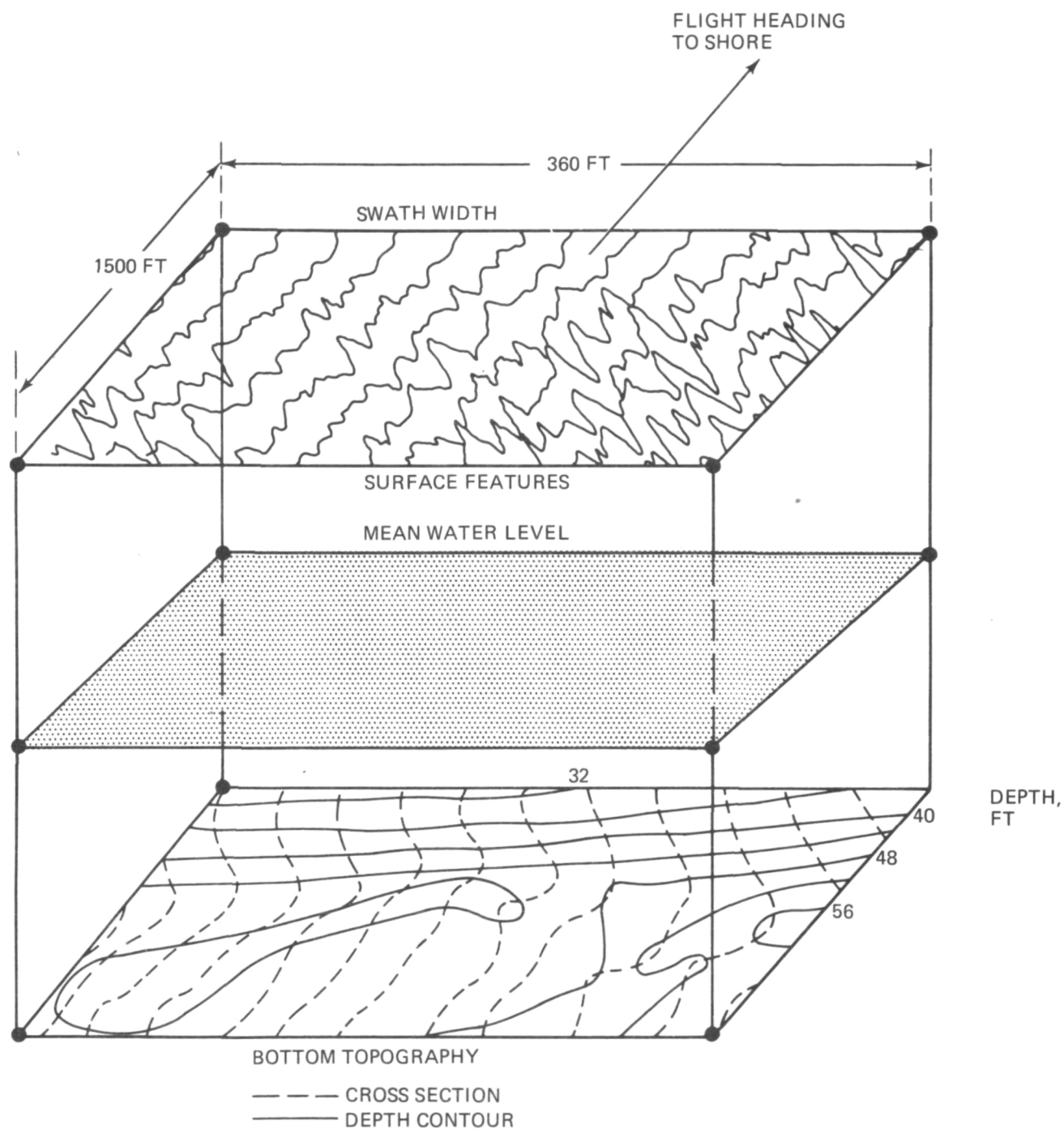——— DEPTH CONTOUR

Fig. 27 Isometric View of Bottom Topography and Surface Features
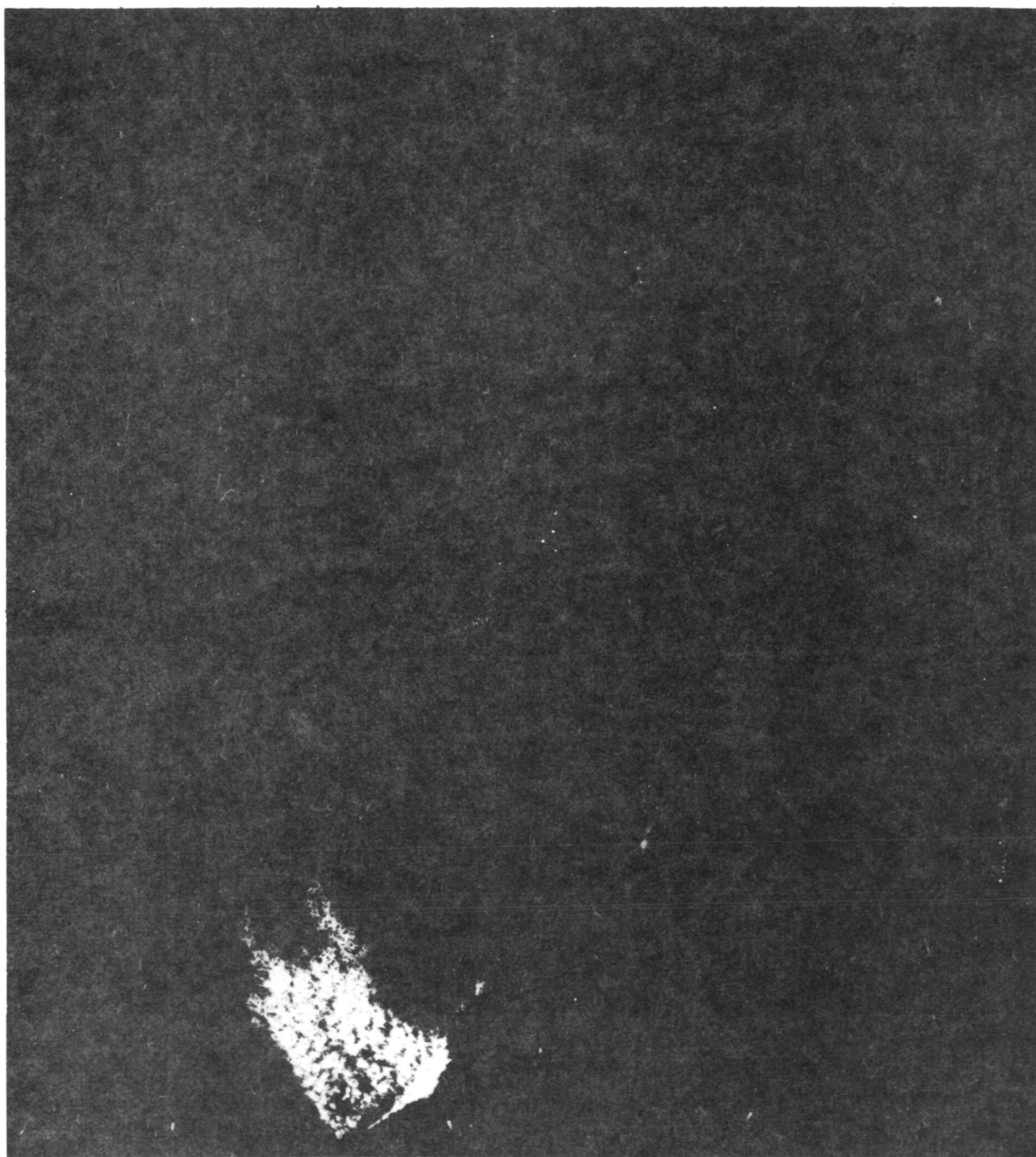
Fig. 28 Hasselblad Photograph of Swells and Whitecaps on Off-Shore Side of Underwater Bluff

II. WATER TURBIDITY

IIA.   PHOTOMETRIC ANALYSIS OF BOSTON HARBOR

1. Background

Originally it was our intention to perform a polarimetric survey of Boston Harbor for the purpose of analysis of water turbidity. We were prevented from accomplishing this goal by three circumstances: the development of cloudy conditions in early afternoon; the prominence of the bottom signature throughout most of the data; and the pronounced spatial variations of radiant signature near effluents and deep channels. These difficulties would not have prevented our acquiring good polarimetric data with a multi-channel scanner. However, since we perform "p" and "s" oriented polarimetric surveillance in successive overflights, the time delay between the two makes solar irradiance corrections necessary if values are changeable. Moreover the inability to duplicate the flight path exactly gives rise to the problem of spatial registration of points in succeeding overflights for computation of values from the same points. We have found it possible to perform registration sufficiently accurate for several cases of water analysis, but found that the spatial and temporal variation of Boston Harbor was too extreme.

These difficulties stem from lack of concurrence in channels to which the obvious answer is to proceed to multichannel sensing. Within the limits of our budget we endeavored to do this by the addition of a second, but non-scanning sensor head. This second head is boresighted to the center of the scanning head transverse sweep. The output is digitized by the same A to D converter which is used for the DPM sensor output. The eight bit digital values are recorded on the DPM magnetic tape once each sweep using blank space available by reason of DPM sweep fly-back.

It would have been possible by use of the second head to derive polarimetric data limited to the centerline of the DPM sweep. Unfortunately, we did not duplicate the spectral filters in the two heads with exactness. Thus while both heads might be measuring through "red" filters, the filter differences nevertheless caused confusing spectral response differences.

However, we had planned to use the second head for a "control" and for multispectral photometry. It served these purposes well. Another means of standardization and control for "bridging" successive overflights (and for the

purposes of absolute photometry) consisted in photometric measurement of solar irradiance values as shown in Figure 18. By a combination of these controls and persistent over-flights we probably could have achieved some polarimetric results. However, as can be seen from Figure 18 the cloudiness developed rapidly and we were forced to abandon the effort.

We have been able to use the centerline radiance trace in two spectral bands for the purpose of two-color photometric analysis of water transparency. This has been of primary importance in water depth mapping, and it has also been important in the analysis of Boston Harbor.

2.   Description of Data

Table I summarizes the data taken in Boston Harbor prior to the time the weather forced us to suspend overflights. The code letters for spectral bands can be understood by reference to Figures 5. The "V" designation for polarization stands for "vertical" and is the usual "p" component in terms of principal plane reference, while the "H" is "horizontal", corresponding to "s" component.

Although we took "H" and "V" data over Boston Harbor (Flight Passes No. 1 and 2) we are not able to extract percent polarization values from these data because of changing solar illumination and lack of imagery overlaps as explained above. Instead we will present a photometric analysis of overflight No. 3 data. The swath actually surveyed during this flight was determined from landmarks on the tracking camera photographs and is shown in Fig. 29. The following figure shows a Coast and Geodetic survey map of the same area, to the same scale, containing the most detailed depth information that is available to us without a special survey.

Figure 31, 32 and 33 show the data from overflight No. 3 in "D" (red) for the scanning DPM and in green (Gr) for the second head. The centerline data shown in Figure 32 are the only two-color data for this overflight. Figure 31 shows data to the right (east) of the centerline whereas Figure 33 shows data to the left (west) of the centerline. The original digital values have been corrected for dark level and for line function (relative response of the tube across the scan line). In addition the logarithm of each value has been taken by the computer. Each longitudinal trace of the overpass is a plot of this logarithmic value. In order to use the photometric data to best advantage in

the analysis of the Harbor we made use of the depth information contained in C&GS map in Fig. 30 and plotted this information in Figures 31, 32 and 33. The abscissa of the plot is actually a multiple of the number of scan lines, ignoring the admitted minor fluctuations in aircraft velocity. The scale was primarily set by concurrent photography of landmarks (see Figure 34 for example), but the bottom profile was adjusted locally to the minor degree required to compensate for variation in aircraft velocity. These are manifested mostly by along-flight shifting of features recorded in the optical signature in our data. The flight path resulting from the "fitting" is shown in Figure 29.

The reason for plotting the optical values in logarithmic form can be discerned by examination of equations (5) and (6). An extraction of depth readings from radiant values requires expression in logarithmic values. In order to place an exact scale on depth several other steps of data processing are required. One preliminary step is the subtraction of K-values corresponding to deep-water radiance. The K-values fluctuate in anomalous waters such as Boston Harbor. Therefore, the simplest expedient of logarithmic expression only is used in order to present a general picture of the situation for preliminary analysis. What this step enables the interpreter to do is to examine the data to select areas of sufficient homogeneity in water parameters to facilitate localized analyses. The criteria for these areas involve first-order comparisons between optical signature and corresponding bottom profiles, as well as certain other general characteristics. These criteria will be discussed and applied to the Boston Harbor data.

Because of the amount of theoretical investigation necessary in order to reduce these rather complex data we have not had the time available for reduction of more than that portion of the total data shown in Figures 31, 32 and 33. There is undoubtedly multispectral interpretation value in the remaining data. At this point we have a foundation for interpretation which we believe represents substantial progress.
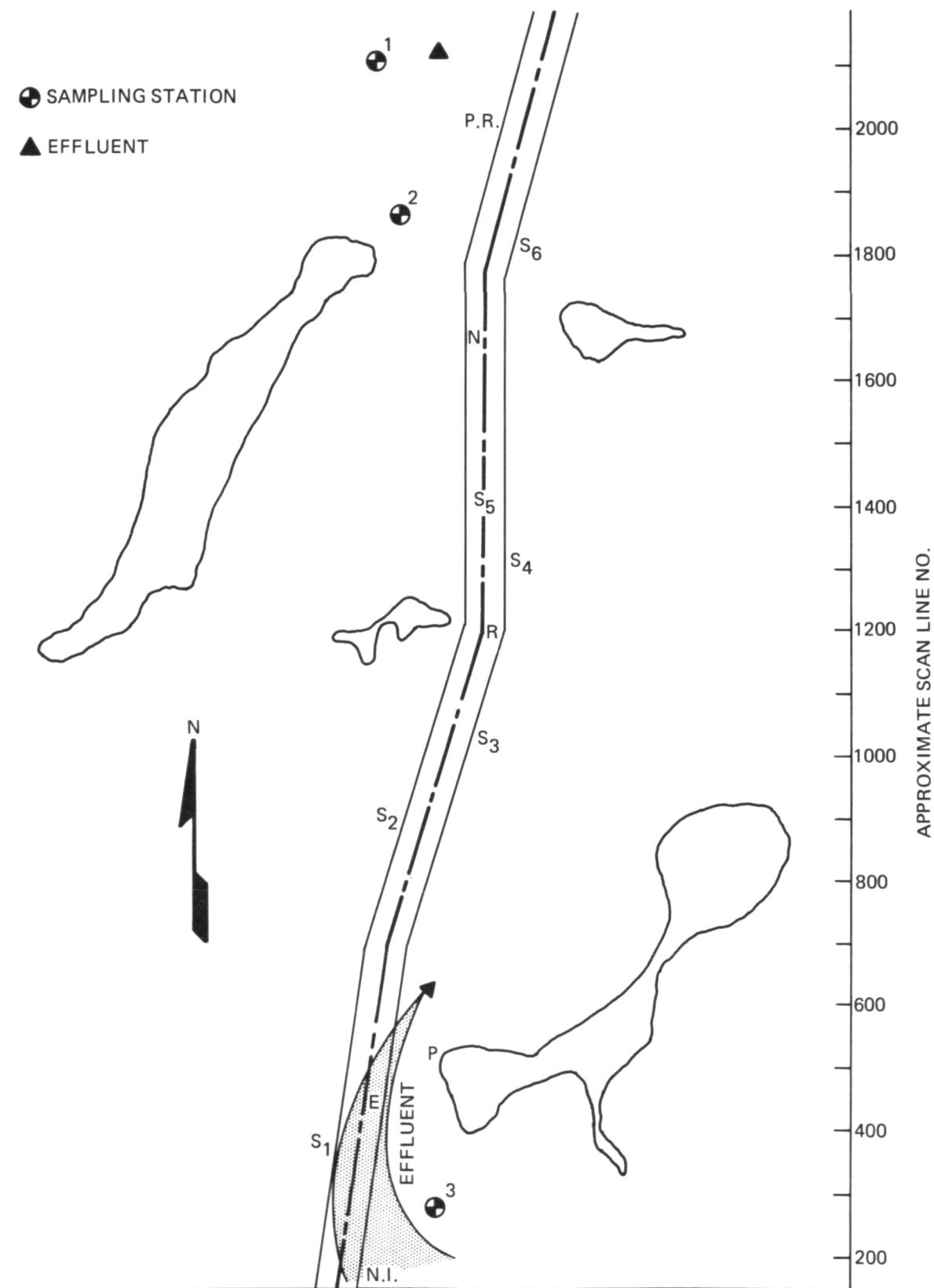
Fig. 29 Boston Harbor Survey Site — Flight Pass No. 3

Fig. 30 U.S. Coast and Geodedic Survey Map (No. 246) of Survey Site

3. Specific Analysis of Non-Effluent Areas

The first general deduction which we made from the data was that the reflectance in the red end of the spectrum was higher than we had anticipated. Because we are limited presently to 8 bits in digital recording it is necessary to use various gain settings to cope with the very large dynamic range. The water areas are much darker than the land areas, in general. However, where the water is shallow the radiance is also much greater than where the water is deep. In order to obtain as much information as possible, the highest possible gain setting was used for the DPM. This setting, consisting of a step-wise calibrated adjustment of the dynode voltage, was meant to cause a saturated digital value (255) near the shore line. Calibrated filters and apertures are used to ensure that the photocathode does not saturate.

Upon examination of the data we found that DPM digital saturation was taking place at about 16 ft. depth. This meant that the digital resolution of changes of radiance was excellent from 16 ft. down, but made interpretation difficult near shoals. The gain in the second head was, fortunately, not set correspondingly high and green data was available for places where the red (DPM) data was saturated. Also the depth profile transverse to the flight line was quite steep in the shoal area and it was usually possible (see Figure 33), to find unsaturated red data on the left (west) portion of the swath.

The second observation was that the sewage effluent areas were very highly reflective in the red and also quite reflective in the green compared to the average harbor reflectance.

The third general observation was that there were patches of "wash-out" in the deep channel areas (see President Roads, for example, Figure 31) where the high reflectance was sharply reduced and the water appeared quite dark.

The fourth general observation was that the bottom profile was followed rather consistently in most of the harbor if allowance was made for the highly anomalous areas of effluent and channels.

A detailed examination of the radiance values in relation to the bottom profile was made by trial application of equations (5) and (6) to the data with assumed values of K_R and K_G. The inconsistencies that were revealed pointed to

variability in all of the important parameters, namely, K-values, volume atten-uation coefficient $(\alpha + \beta)$, and bottom reflectance. It was decided to perform local analysis by "zones". In searching for criteria by which to identify areas of homogeneity use has been made first of all of the data calculated upon the basis of an assumed model (and presented in Appendix C) which shows the antici-pated relationship between photometric radiance changes and the change in depth of bottom to which they may be attributed. Figures 35, 36, and 37 present the "sensitivity analysis" for three spectral bands. Use can be made of these plots by converting the "present DPM capability - 1%" into actual binary values. The full binary radiant number shown in the data is multiplied by .01 to furnish a number which, in the plotting of depth against radiance, should represent an incremental depth resolution shown along the ordinate.

A precautionary note is necessary. The test should be applied as a measure of penetration to depth rather than sensitivity at shallow depths, because in-creased turbidity actually enhances the sensitivity at shallow depths as can be ascertained by comparing shallow values between Figures 35, 36, and 37. Thus in the green it is desirable to examine response at depths of 40 ft. or more, although we will make limited use of data from shallower water.

As the spectral pass band progresses into the red and near infrared portion of the spectrum decision becomes easier at shallow depths. Looking at Fig. 37 for 6800 A it is seen that, if there is any response remaining at 18 ft. depth, the water must be quite clear.

This "yardstick" of water clarity can be applied only very loosely, but does serve for a preliminary examination of data. Equation (24) shows, for example, that the actual photometric depth gradient is dependent not only upon the volume attenuation coefficient, but also upon the quantity, $(G-K_G)$, or $(R-K_R)$ involving substantial differences in gradient for large values of K_G or K_R.

Further, more quantitative characterization of zones of water parameter homogeneity can be made principally by use of equations (33), (22), and (7), repeated here as follows (changing G's to R's where appropriate):

$$\log_{10} \frac{R_1 - R_2}{R_2 - R_3} = 2f(d_2 - d_1)(\alpha + \beta)_R \qquad (33)$$

$$K_R = \frac{R_2 Q - R_1}{Q - 1} \qquad (22)$$

$$\gamma_{R/G} = \frac{\log_{10} \dfrac{R_1 - K_R}{R_2 - K_R}}{\log_{10} \dfrac{G_1 - K_G}{G_2 - K_G}} \qquad (7)$$

To illustrate the application of these equations Fig. 38 has been extracted from Fig. 32 to show the relationships. To apply the equations, first of all the radiance data points are smoothed to remove extraneous perturbations having no bearing on the relationships. Then the smoothed data are examined for regions which are of relatively uniform upward concavity corresponding to bottom slopes of lesser upward concavity (larger radius of curvature). The reason for this criterion becomes apparent by examination of the case chosen for illustration. Substituting the radiance values in equation (33):

$$R_1 = 234; \quad R_2 = 215: \quad R_3 = 209$$

$$G_1 = 165 \quad G_2 = 158.5 \quad G_3 = 155.5$$

$$d_2 - d_1 = 5 \text{ ft.}$$

Assuming $f = 1.1$

$$\log_{10} \frac{234 - 215}{215 - 209} = .505 = 2.2(\alpha + \beta)_R \times 5$$

$$(\alpha + \beta)_R = .046 \log_{10} \text{ ft}^{-1}$$

$$\log_{10} \frac{165 - 158.8}{158.5 - 155.5} = .34 = 2.2(\alpha + \beta)_G \times 5$$

$$(\alpha + \beta)_G = .03 \log_{10} \text{ ft}^{-1}$$

$$Q_R = 3.2$$

$$K_R = \frac{215 \times 3.2 - 234}{3.2 - 1} = \frac{688 - 234}{2.2} = 206$$

$$Q_G = 2.2$$

$$K_G = \frac{158.5 \times 2.2 - 165}{2.2 - 1} = \frac{349 - 165}{1.2} = 153$$

As a cross-check, substituting in equations (5) and (6)

$$\log_{10} \frac{234 - 206}{215 - 206} = 2 \times .046 \, (d_2 - d_1)$$

$$d_2 - d_1 = \frac{.49}{.092} = 5.3 \quad \text{ft.}$$

$$\log_{10} \frac{165 - 153}{158.5 - 153} = 2 \times .03 \, (d_2 - d_1)$$

$$d_2 - d_1 = \frac{.30}{.06} = 5.0 \text{ ft.}$$

Also
$$\gamma_{R/G} = \frac{\log_{10} \dfrac{234 - 206}{215 - 206}}{\log_{10} \dfrac{165 - 153}{158.5 - 153}} = \frac{.49}{.30} = 1.6$$

This result can now be compared to the value of $\gamma_{R/G}$ obtained by the previous method

$$\gamma_{R/G} = \frac{(\alpha + \beta)_R}{(\alpha + \beta)_G} = \frac{.046}{.03} = 1.53$$

The conformance of the "fit" to the various measures of validity appears to be good. In fact it is better than that of the average data from Boston Harbor. What is probably to be inferred is that this area chosen is quite free (within the flight path limits indicated) from fluctuations in bottom reflectance, water transparency and surface reflectance.

In regard to the possible fluctuations in parameters it should be noted that the radiance values in the "clear" portion of President Roads are about

148 in the green and 110 in the red. If an attempt were made to use these values as the K_G and K_R in the above illustration, it would be impossible to achieve a good fit. We conclude that in actuality the effective "deep-water" radiance (no bottom signature) does vary substantially over the harbor and that there must be a marked "surface" effect. It should particularly be noted that the fluctuation of K-values is most extreme in the red, indicating the probable presence of a prominent red-reflecting layer near the top, distributed non-uniformly.

Use of known depth profiles, or depth increments, for parametric fitting of photometric data has several limitations, one of which is that parameters extracted are good only over the depth range for which values were used. Thus in the example cited and illustrated in Fig. 38, the conclusion that the water is of usual clear coastal quality, described as $(\alpha + \beta)_R = .05$, only holds between the depths of 22 ft. and 32 ft. The water parameters in an area such as this frequently exhibit a marked "layering". The high red reflectance $(K_R = 206)$ probably indicates also a top layer of lower transparency. What lies below the 32 ft. depth may be quite variable. Certain areas are probably quite "muddy" as the result of the dynamics of the water and the transport of bottom sediment.

In the specific application of the analytic techniques described to Boston Harbor reference will be made to the flight path shown in Figs. 29 and 30 and the photometric and depth profiles shown in Figures 31, 32, and 33. For convenience in discussion various features have been identified by the following symbols:

N.I.	Nut Island
P	Offshore Peddocks Island
E	Sewer Outfall, Effluent
R	Offshore Rainsford Island
NC	Nubble Channel
PR	President Roads

S1, S2, S3, S4, S5, S6 - Shoal like areas where the depth is locally less than the surrounds. Some can be identified by name. For example S4 is Hospital Shoal. S6 is associated with Nixes Mate.

We associate Nubble Channel and President Roads in our data not only with

the depth contours with which they would normally be associated, but also with the surface evidence which are presented in our data for the location of these features. These evidences are rather spotty but they occur as pronounced "clearing" of the cloudy red-reflecting top layers by the current and reveal a more direct deep-water and bottom signature. This phenomenon is extremely pronounced in the case of President Roads and observable, but less pronounced for Nubble Channel. Reference is made particularly to the central profile Fig. 32 for the pronounced dip in measured radiant values in both the green and the red at President Roads.

One of the most prominent features of the profile is the photometric evidence of the sewer outfall, designated E, which extends over rather lengthy section of the profile near Peddocks Island. As has been pointed out previously this section is substantially more reflective than its environs particularly in the red where it has caused saturation of digital values. The effluent is so prominent that by combined reflection of sunlight and attenuation of the bottom signature it effectively masks the bottom signature. By the application of a multiple scatter photometric model the red DPM data in the area of the effluent has been reduced to a turbidity map as shown in Fig. 41. The details of the reduction of these data will be discussed separately.

An examination of the photometric data in the surrounds of the effluent reveals that it has not contaminated this water, e.g. between the depths of 20 ft. and 45 ft., to the extent that the bottom is obscured optically from our sensor. In fact a preliminary screening by use of a rough "sensitivity analysis" using data from Figures (35), (36), and (37) shows that the water (in depth) is not too far from the transparency of clear coastal water. Local, cloudy "spotting" at the top can be seen by comparing the value of K_R extracted from the center section (195) to the value (130) from the westermost (left) profile shown in Figure 33.

It should be realized that inaccuracies in the observed data, and in the depth information, taken together with probable non-uniformity of basic water and bottom parameters prevent a high order of analytic accuracy in our data. Increase in accuracy is quite possible by improvement of inputs and refinement of analytic technique. However, it can be shown by a number of illustrations that meaningful interpretation can be placed upon our data by use of the various

equations we have presented. Numerical illustrations will be presented beginning with the slopes off Nut Island at the beginning of the overflights as follows:

SUMMARY OF WESTERN (LEFT) PROFILE, UPPER SLOPE (Fig 33 Scan lines 315 - 345) 40 binary units for 2 ft. (0.6 meter) depth change at a mean depth of about 24 ft. and a mean radiance level of about 212 binary units 1% of 210 = 2.10 units, corresponding to $\frac{2.1}{40}$ x 24 = 1.3 in. From Figure 36 it is seen that the water must be quite clear; $(\alpha + \beta)_R \simeq .045 \log_{10}$ ft.$^{-1}$. In $\log_e$ metric units, $(\alpha + \beta)_{R_m} = .34$.

Applying the data to equation (24) assuming f = 1.1,

$$\frac{\Delta R}{\Delta d} = \frac{40}{.6} - 2f (\alpha + \beta)_{R_m} (R_d - K_R)$$

$$= 2.2 \ (.34) \ (212 - K_R)$$

$$K_R = 123$$

SUMMARY OF WESTERN (LEFT) PROFILE, LOWER SLOPE (Fig 33, scan lines 345-375) 24 binary units for 2 ft. (0.6 meter) depth change at a mean depth of about 24 ft. and a mean radiance level of 182 binary units 1% of 183 = 1.8 units, corresponding to $\frac{1.8}{24}$ x 24 = 1.8 in. From Figure 36, it is seen, again, that $(\alpha + \beta)_R \simeq .045 \log_{10}$ ft^{-1}. Applying lower slope data to equation (24)

$$\frac{\Delta R}{\Delta d} = \frac{24}{.6} = 2.2 \ (.34) \ (182 - K_R)$$

$$K_R = 129$$

Also applying equation (33) to the total slope changes (upper and lower) for the WESTERN (LEFT) DATA

$$R_1 = 234; \ R_2 = 194; \ R_3 = 170$$

$$\log \frac{234 - 194}{194 - 170} = 2 \times 1.1 \ (\alpha + \beta)_R \times 2$$

$$(\alpha + \beta)_R = .05$$

Computing K_R from equation (22)

$$K_R = \frac{R_2 Q - R_1}{Q - 1} = \frac{194 \times 1.67 - 234}{.67} = 135$$

As a further arithmetic cross-check equation (5) can be applied to
the computation of depth increment as follows:

$$\log \frac{R_1 - K_R}{R_2 - K_R} = 2f \ (\alpha + \beta)_R \ (d_2 - d_1)$$

$$\log \frac{234 - 130}{194 - 130} = 2.2 \ (.045) \ (d_2 - d_1)$$

$$d_2 - d_1 = 2.1 \text{ ft}$$

SUMMARY OF CENTER PROFILE UPPER SLOPE (Fig 32, scan lines 330 - 345)
18 binary units for 2 ft. (0.6 meter) depth change at a mean depth of
about 21 ft. and a mean radiance level of about 235 binary units. 1%
of 235 = 2.35, corresponding to $\frac{2.35}{18}$ x 24 = 3.2 in. From Fig. 36, it
is seen that the volume attenuation coefficient must lie in the region
of .045 $\log_{10}$ ft.$^{-1}$.
Substituting in equation (24), $\frac{\Delta R}{\Delta d} = \frac{18}{0.6} = 2.2 \ (.34) \times (235 - K_R)$

$$K_R = 195$$

SUMMARY OF CENTER SECTION LOWER SLOPE DATA (Fig. 32, scan lines 345 - 375)
12 binary units for 2 ft. (0.6 meter) depth change at a mean depth of
about 23 ft. and a mean radiance of about 220 binary units. 1% of 220 =
2.2, corresponding to $\frac{2.2}{12}$ x 24 = 4.4 inches. Again $(\alpha + \beta)_R \simeq .045$
$\log_{10}$ ft.$^{-1}$. Substituting in equation (24)

$$\frac{\Delta R}{\Delta d} = \frac{12}{0.6} = 2.2 \ (.34) \ (220 - K_R)$$

$$K_R = 193$$

Also applying equation (33) to the total slope changes (upper and lower) for the CENTRAL SECTION DATA

$$R_1 = 244; \quad R_2 = 226; \quad R_3 = 214$$

$$\log_{10} \frac{244 - 226}{226 - 214} = 2.2 \, (\alpha + \beta)_R \times 2$$

$$(\alpha + \beta)_R = .04$$

Computing K_R from equation (22)

$$K_R = \frac{R_2 Q - R_1}{Q - 1} = \frac{226 \times 1.5 - 244}{.05} = 190$$

Arithmetically checking by means of equation (5)

$$\log_{10} \frac{244 - 193}{226 - 193} = 2.2 \, (.045) \, (d_2 - d_1)$$

$$d_2 - d_1 = 1.9 \text{ ft}$$

Proceeding beyond the effluent area the rising slope immediately ahead of feature S_2 has been analysed as an illustration previously yielding a value of $(\alpha + \beta)_R$ of about .05 $\log_{10}$ ft^{-1} and a value of K_R equal to 206 in the CENTER SECTION. The depth is greater here than immediately off Nut Island. The slope immediately prior to S_2 is about 9 binary units for a depth of about 33 feet and a mean radiance level of about 207 binary units. 1% of 207 = 2.1 units, corresponding to $\frac{2.1}{9} \times 24 = 6$ in. From Figure 36 it appears that $(\alpha + \beta)_R < .045$. From the data it would appear that the depth may be several feet less than 33 ft.

Evidence of increasing "spotty" turbidity builds up as the trend of data between S_2 and S_3 is followed. Both the CENTER SECTION and the WEST SECTION show areas where the slope is not followed consistently by the radiance measurements. Ultimately over S_3 the red values (R) do not saturate until a shallow depth of about 12 ft. has been attained (contrasting with initial saturation of 16 ft.) In the CENTER SECTION UPPER SLOPE an increment of about 14 binary units is observed for a depth change of 10 ft. at a mean depth of 15 ft. and a

mean radiance of about 232 binary units. 1% of 232 = 2.3 units, corresponding to $\frac{2.3}{14}$ x 120 = 20 inches. From a comparison of data from Figures 36 and 37, it appears that $(\alpha + \beta)_R$ at about 15 ft. depth must be in the region of a value of .15 $\log_{10}$ ft^{-1}. Substituting in equation 24, it appears that $K_R \simeq 220$.

In the valley between shoal S_3 and off-shore Rainsford (R) the green radiance (G) continues to climb indicating that the heavy turbidity over S_3 is decreasing somewhat. However, using data from the WEST LEFT SECTION for analysis of the upward slope toward R:

25 binary units for about 10 ft. change of depth at a mean depth of about 16 ft. and a mean radiance of about 209.

1% of 209 = 2.1 binary units corresponding to $\frac{2.1}{25}$ x 120 = 18 in. From Figures 36 and 37, it appears that the value of $(\alpha + \beta)_R$ is about .10.

Again substituting in equation (24) the value of K_R over this slope in the WEST LEFT SECTION appears to be about 175.

In the CENTER SECTION slightly beyond the offshore area R, the green (G) data can be analyzed as follows on the down-slope:

44 binary units for a depth change of about 16 ft. at a mean depth of about 18 ft. and a mean (G) radiance level of 200.

1% of 200 = 2.0 units, corresponding to $\frac{2.0}{44}$ x 192 = 9 inches. From Figures 35 and 37, this appears to indicate $(\alpha + \beta)_G \simeq .08$, and, from equation (24), K_G = 174. From Figure 7 it appears that a corresponding value of $(\alpha + \beta)_R$ would be about .12 $\log_{10}$ ft^{-1}.

A computed value for K_G off Nut Island, corresponding to K_R = 190 is 149. It is assumed a proportion may be set up to approximate the value of K_R in the vicinity analyzed for K_G, as follows:

$$\frac{174}{149} = \frac{K_R}{190}$$

$$K_R = 222 \qquad \text{(a CENTER SECTION VALUE around scan line 1200)}$$

Red (R) data can be analyzed from the WESTERN (LEFT) SECTION AS follows:

15 binary units for 18 ft. drop at a mean depth of about 12 ft. and a mean radiance of about 220.

1% of 220 = 2.2 corresponding to $\frac{2.2}{15}$ x 216 = 32 inches. From Figure 37 it can be seen that $(\alpha + \beta)_R > .083$ and probably $.12 \log_{10}$ ft^{-1} is a reasonable value.

Substituting in equation (24)

$$\frac{\Delta R}{\Delta d} = \frac{1.5}{5.5} = 2.2 \ (.91) \ (220 - K_R)$$

$$K_R = 219.5$$

From off-shore Rainsford area toward Nubble Channel (NC) the Green (G) data in the CENTRAL SECTION reveals that the response to depth changes is spotty with occasional clearing of the water in local areas. The S_4 and S_5 features revealed by two successive spikes in the data are indicative of this clearing trend. In these data immediately beyond S_5 the water has cleared to the point where the far downward slope of S_5 can be analyzed. Analysis by means of equations (33) and (22) reveals $(\alpha + \beta)_G = .02 \log_{10}$ ft^{-1} and $K_G = 172$ binary units. Corresponding to $(\alpha + B)_G = .02$, in accordance with Figure 7, $(\alpha + \beta)_R = .04 \log_{10}$ ft . Using a ratio similar to that employed for green (G) data on the slope beyond Rainsford, we obtain $K_R = 215$. Partly because of the high red reflectance the red data is saturated (255) at 28 ft. instead of the 16 ft. (as in off-Nut Island area). However, the saturation also tends to confirm the calculated water clarity. It is difficult to calculate a number for $(\alpha + \beta)_R$ for the region near Nixes Mate (S6), but it can be guessed to be in the neighborhood of $.20 \log_{10}$ ft^{-1}. There appears to be a response of about 9 binary units in the CENTER SECTION to what seems a 2 ft. rise immediately prior to scan line 1830. The response itself is an indication of a clearing trend as the overflight progresses north of S_6. Substituting $(\alpha + \beta)_{R_m} = 1.5$ in equation (24)

$$\frac{\Delta R}{\Delta d} = \frac{9}{.6} = 2.2 \ (1.5) \ (240 - K_R)$$

$$K_R = 235$$

Beyond S_6 the depth increases rapidly. From previous trends in this analysis it would be anticipated that the water would clear up as it gets deeper. It

is evident that it does. The red data comes out of saturation at a depth of 16 ft. which is a rough indication that the water at 16 ft. depth scan line 1905 resembles that at scan line 330 at the beginning of the run. The detection of a small feature at scan line 2019 at a depth of 42 ft. places the values of $(\alpha + \beta)_R$ at about .04 $\log_{10}$ ft^{-1}, at this point. Immediately prior to this point in the WEST (LEFT) SECTION there is evidence of a "concave-up" radiance profile in fairly clear water at a mean depth of about 23 ft. The radiance slope is about 11 binary units for a 10 ft. drop at a mean radiance of about 195. 1% of 195 = 1.95, corresponding to $\frac{1.95}{11}$ x 120 = 21 inches. From Figures 35 and 36 it would seem that the data are fitted best by $(\alpha + \beta)_R$ = .06 $\log_{10}$ $ft.^{-1}$. Substituting in equation (24) we get K_R = 192.

There is a break in the profile followed by another uniformly concave-up slope of radiance. The radiance slope is about 22 binary units for a 22 ft. drop at a mean radiance level of 175 and at a mean depth of 44 ft.

Applying previous methods of analysis, 1% of 175 = 1.75 corresponding to $\frac{1.75}{22}$ x 264 = 21 inches. From an examination of Figure 36 it is seen, however, that this sensitivity at a depth of 44 ft. is not accountable by a within-reason low value of $(\alpha + \beta)_R$. The possible explanations include a decrease in water reflectance (K_R). Assuming the latter to be the case and the lowest conceivable value of $(\alpha + \beta)_R$, i.e. .038 $\log_{10}$ ft^{-1} equation (24) can be used to calculate a mean value of K_R.

$$\frac{\Delta R}{\Delta d} = \frac{22}{6.6} = 2.2 \left(\frac{.035}{.132}\right) (175 - K_R)$$

$$K_R = 169$$

Points may be selected on the profile as follows:

$$R_1 = 188 \quad d = 36$$

$$R_2 = 166 \quad d = 58$$

An attempt to apply equation (5) to a computation of depth change between these points involves at once the difficulty of a value of R_2 which is smaller than the value of K_R. Obviously this ambiguity can be resolved by assuming a new value of K_R to be associated with R_2. Calling this new value of K_R "x" a modified form of equation (5) can be set up assuming 169 is an appropriate

value of K_R for R.

$$\log_{10} \frac{188 - 169}{166 - \chi} = 2.2 \; (.035) \; 22$$

$$\chi = 165.6$$

Obviously at a depth of 58 ft. there is very little bottom signature remaining and the values of R and K_R are essentially one and the same. Beyond this point in President Roads (PR), there is a precipitous drop in the values of R, undoubtedly indicating a "washing out" of the top layers of high red reflectance, bringing the value of R (and K_R) tc a low of about 110. Presumably this is a value for deep clear coastal water, relatively homogeneous to the top with a value of $(\alpha + \beta)_R$ equal to .04 $\log_{10}$ ft $^{-1}$.

On the northern side of President Roads there is a recurrence of higher red reflectance. The fact that a feature at 40-44 ft. is detected leads to the assumption that the water is still clear coastal water, $(\alpha + \beta)_R = .04$, at substantial depth, but that an overlying layer of red-reflecting particulate-contaminated water is present. It is assumed that the value of K_R fluctuates in the range of 160-170 to account for the principal part of the signature in this region.
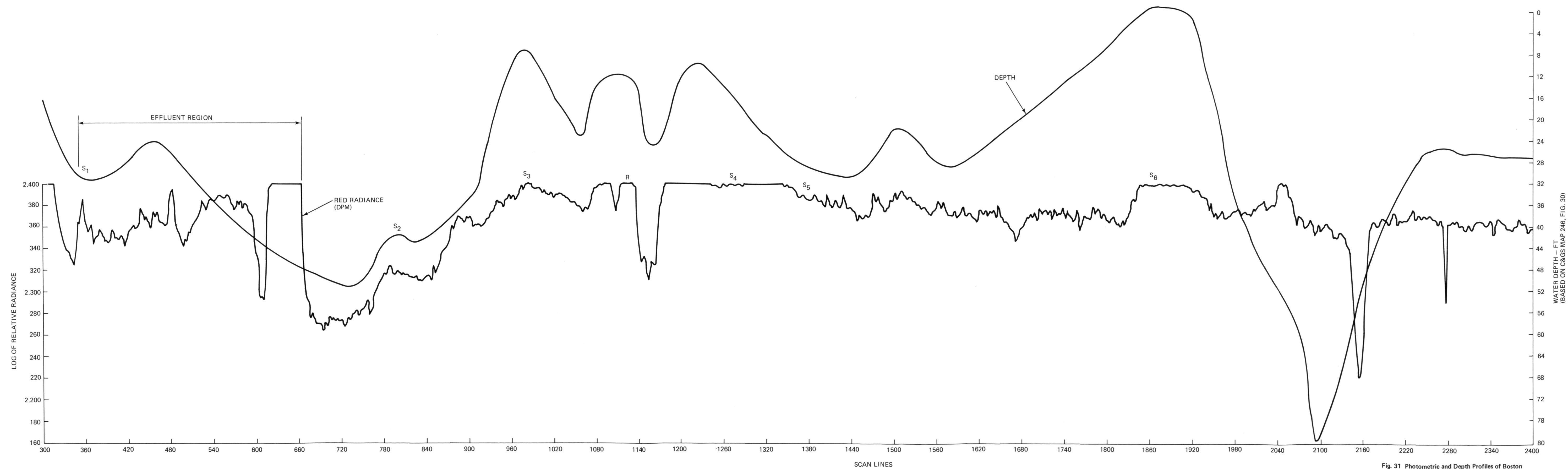
Fig. 31 Photometric and Depth Profiles of Boston Harbor; Overflight No. 3, East Edge of Swath (Right Side)
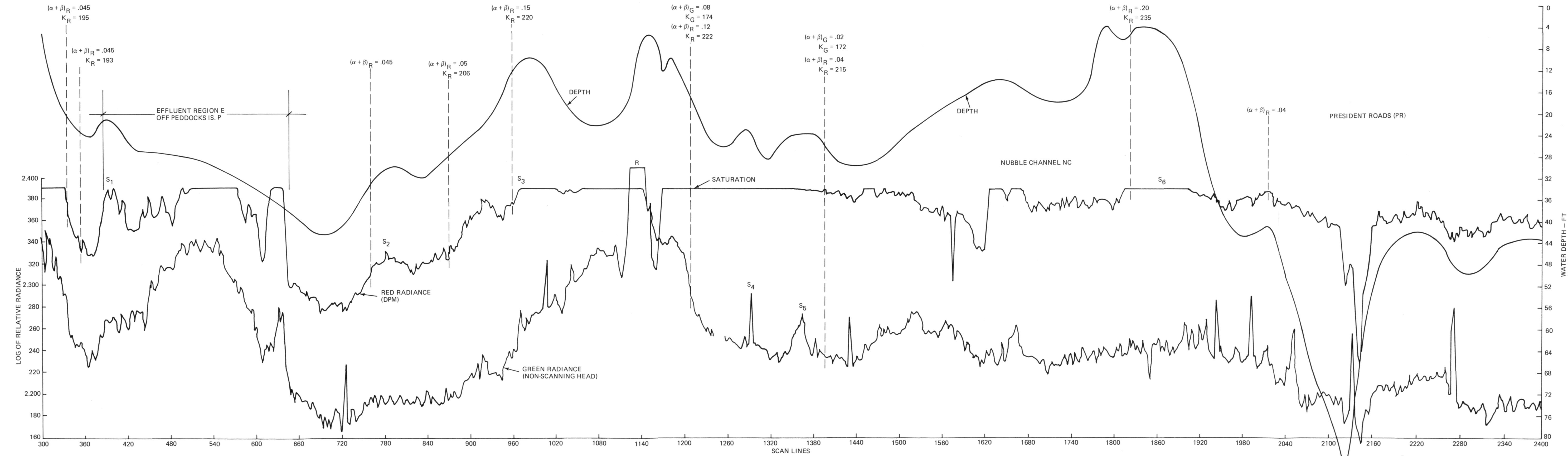
Fig. 32 Photometric and Depth Profiles of Boston Harbor; Overflight No. 3, Centerline of Swath

$(\alpha + \beta)_R = .045$
$K_R = 123$

$(\alpha + \beta)_R = .045$
$K_R = 129$

$(\alpha + \beta)_R = .10$
$K_R = 175$

$(\alpha + \beta)_R = .12$
$K_R = 219.5$

WEST PROFILES (LEFT EDGE OF SWATH)

$(\alpha + \beta)_R = .06$
$K_R = 192$

$(\alpha + \beta)_R = .04$
$K_R = 166-169$

$(\alpha + \beta)_R = .04$
$K_R = 110$

$(\alpha + \beta)_R = .04$
$K_R = 160-170$

2 FT

2 FT

DEPTH

WATER DEPTH – FT
(BASED ON C&GS MAP 246, FIG. 30)

LOG OF RELATIVE RADIANCE

EFFLUENT REGION

S_1

S_2

S_3

S_4

S_5

S_6

R

RED RADIANCE
(DPM)

SCAN LINES
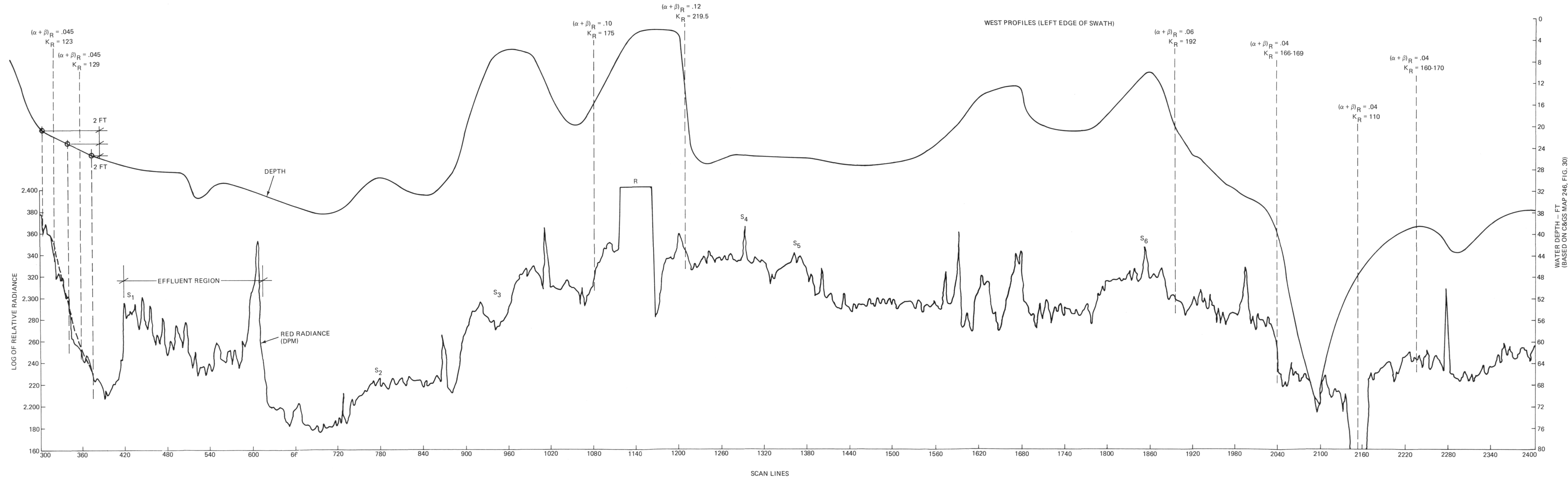
Fig. 33 Photometric and Depth Profiles of Boston
Harbor; Overflight No. 3, West Edge of
Swath (Left Side)

WEST TIP OF
PEDDOCKS ISLAND

EFFLUENT OFF PEDDOCKS ISLAND

GALLOPS ISLAND

Fig. 34 Tracking Camera Photographs of Boston Harbor Landmarks

Fig. 35 Sensitivity Analysis for Clear Coastal Water at 5300A Diffuse Attenuation Coefficient = .02 $Log_{10}Ft^{-1}$

Fig. 36 Sensitivity Analysis for Clear Water at 6250A Diffuse Attenuation Coefficient = .045 Log $_{10}$ Ft $^{-1}$

Fig. 37 Sensitivity Analysis for Coastal Water at 6800A Diffuse Attenuation Coefficient = .083 $Log_{10}Ft^{-1}$

Fig. 38 Case Study for Calculation of Water Parameters

4. Procedure For Effluent Plume Analysis

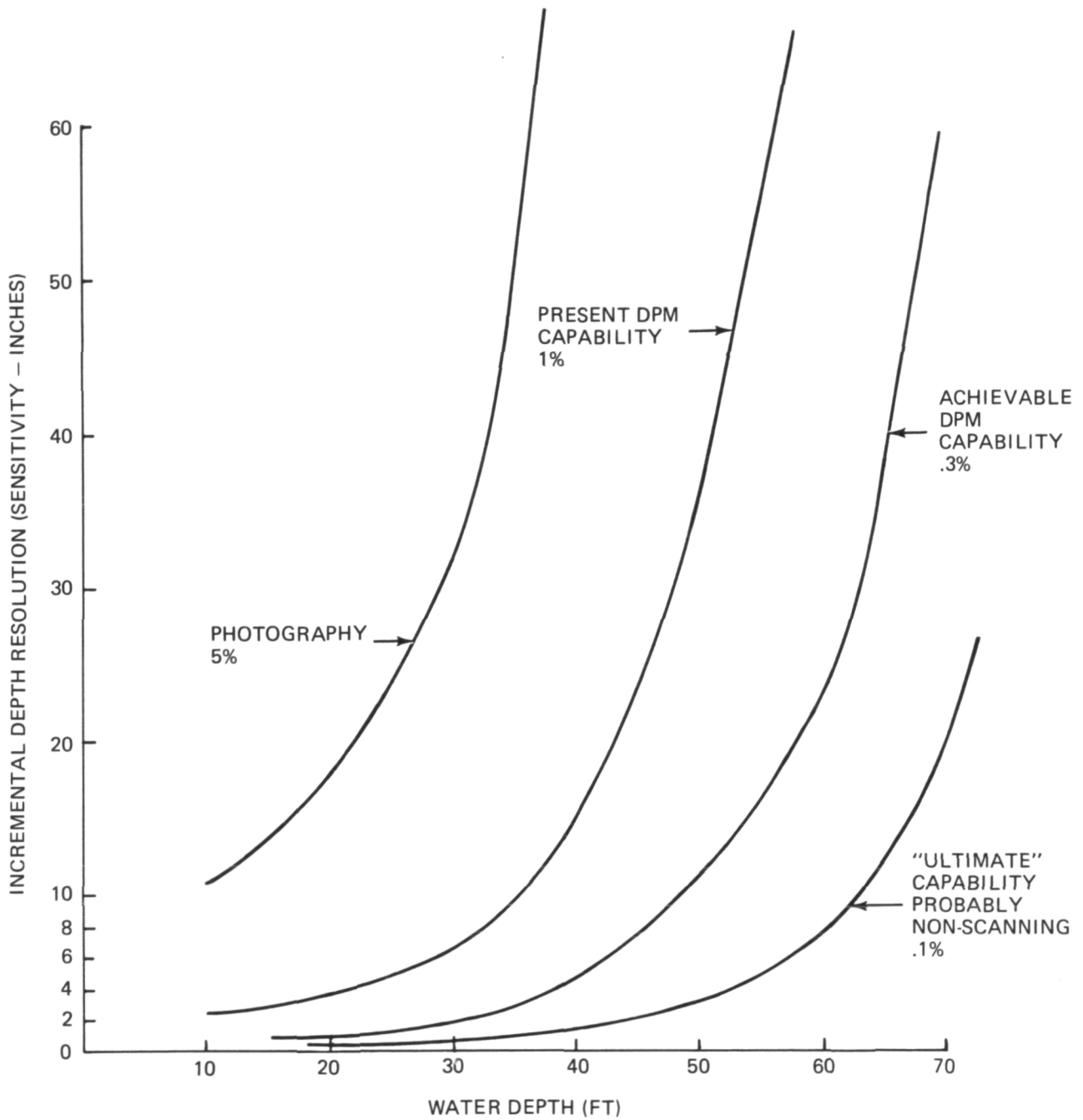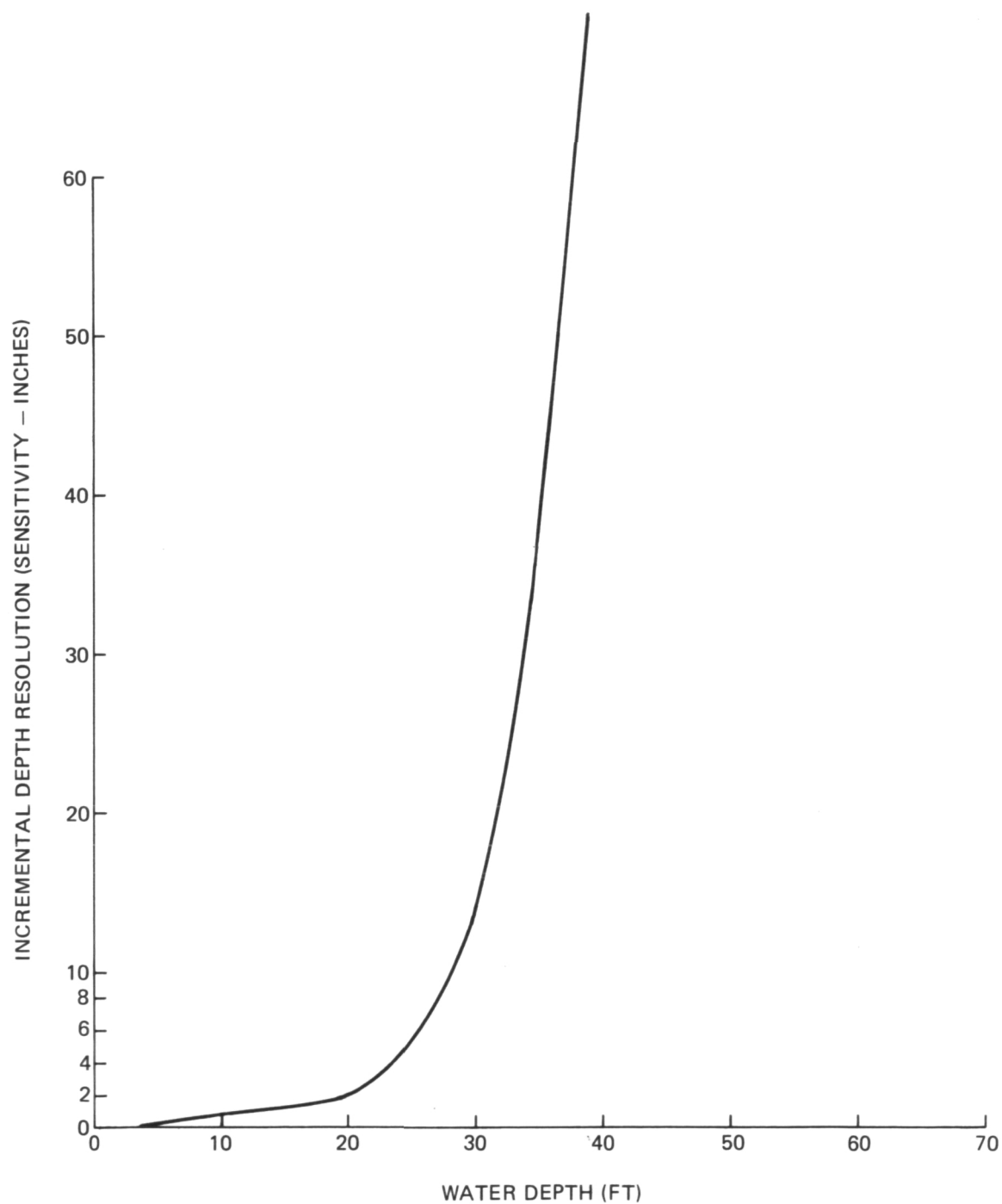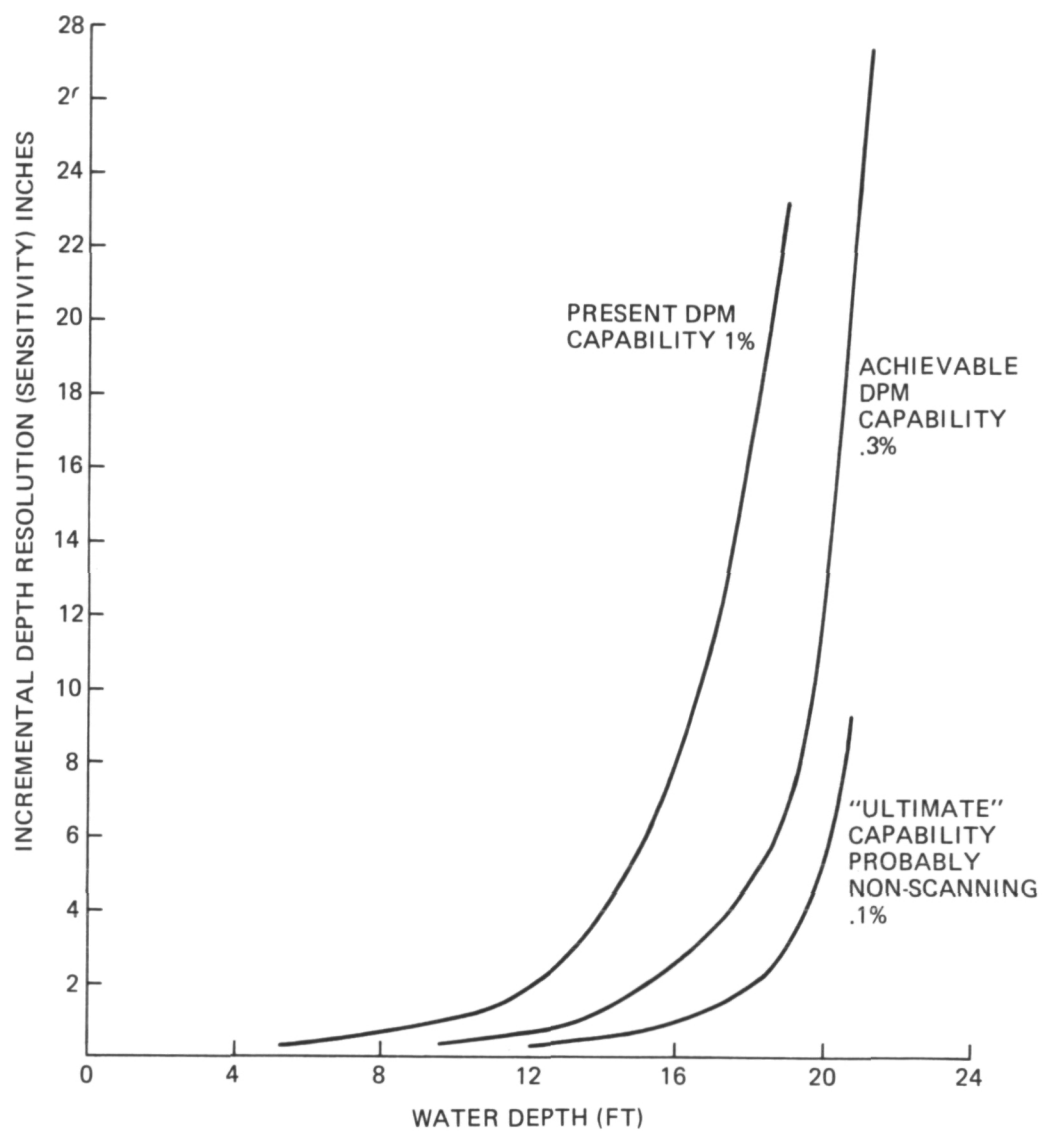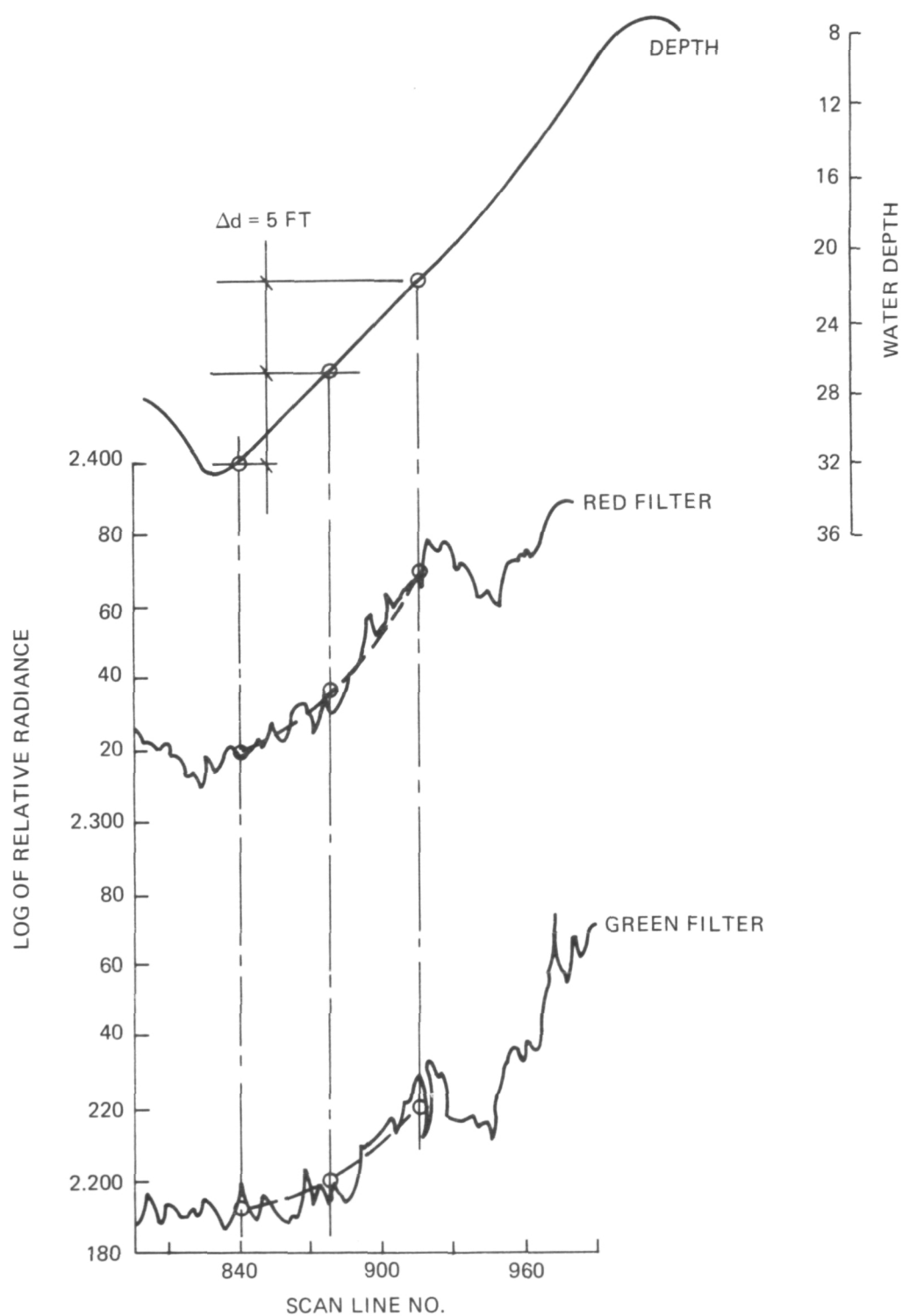We decided to analyze the red (R) data as probably providing a more reliable measure of effluent turbidity than the green. However, the most prominent part of the effluent plume, marked P and E in Fig. 32, shows much saturation in the red. In order to provide information on the saturated peak an extrapolation from the green (G) data is performed as shown in Fig. 39. Where the plume is dense the signature is apparently free of bottom signature at 25 to 40 ft depth because of strong attenuation. However, in order to check on less dense portions in which correction for bottom signature may be desirable, the bottom signature is interpolated from the edges of the plume. Parameters of $(\alpha + \beta)_R = .04$ and $K_R = 199$ are substituted in equation (5) since they are representative of the plume environs.

The evaluation of the plume in terms of Jackson Units was performed by use of equations (41) and (34). Equation (41) was fitted to the data by making use of one control point and one other point which is admittedly an estimate. The control is the data from Station No. 3 at the edge of the effluent as shown in Fig. 29. A summary of the measurements is given in Table II. At the time of our overflight this station was reading 4 to 5 Jackson Units. The other calibration input is the estimated turbidity of the clear part of President Roads where the evidence points to the existence of clear coastal water with probably only slight evidence of a turbid layer on the top. The binary values run between 100 and 110 for the radiance of this clear area.

Our photometric calibration, taken into account with the sky brightness data recorded as shown in Fig. 18, enables us to make allowance for specularly re-flected sky light (at .021 reflectance). Our calculations indicate the specular sky reflection was contributing 20 binary units.

We make the assumption that water of .8 Jackson Unit turbidity in the clear area would have a radiance of 100 binary units. One Jackson Unit is character-istic of water for which $(\alpha + \beta)_R$ has a value of .049 in accordance with equa-tion (34). While our data show effectively less than this value at a depth of 40 ft. or more, it is likely to be as high as .045 at the surface in terms of the measurements made with our relatively broad red "D" filter. This is due to the deep water acting as a spectral filter superimposed on the "D" characteristic curve.

Fitting equation (41) to these two points by adjusting the value of S we find a value of 0.75 to result in an adequate fit. Since we are largely concerned with the water near the surface we use a value of α_R corresponding to about 6250A which is .035. The equation adapted to our data is the following:

$$\text{Log}_{10}\frac{I_1}{I_2} = .75 \, (.035) \left[\frac{1}{(\alpha + \beta)_{R2}} - \frac{1}{(\alpha + \beta)_{R1}} \right] \qquad (41)$$

As an example, consider the substitution of values corresponding to $R_1 = 275$ and $R_2 = 100$ where R_1 is the peak value of the plume as shown in Fig. 39

$$I_1 = 275 - 20$$

$$I_2 = 100 - 20$$

$$\text{Log}_{10}\frac{255}{80} = .75 \, (.035) \left[\frac{1}{.045} - \frac{1}{(\alpha + \beta)_{R1}} \right]$$

$$(\alpha + \beta)_{R1} = .33$$

Making use of equation (34)

$$T = 60 \, (.33) - 1.9 = 17.9 \text{ Jackson Units}$$

A map of the binary values of the red (R) data across the most prominent part of the effluent is shown in Fig. 40. The data has been extrapolated as explained at the beginning of this section to a peak value of R = 275. Contour lines have been drawn for each decade of binary values (i.e., 270-280, 260-270, 250-260, 240-250, 230-240, 220-230, 210-220, 200-210, 190-200, 180-190 and 170-180). For each contour interval the turbidity in Jackson Units has been computed for the mid-values (e.g. 275, 265, 255, etc) and that value assigned to the whole contour interval.

We feel also that it is meaningful to compute a turbidity value for each computed value of K_R. This value of turbidity is associated with the top layers characterized by this amount of red reflectence. This has been done in the same manner as for the effluent plume and the results are shown in Figures 41 and 42.
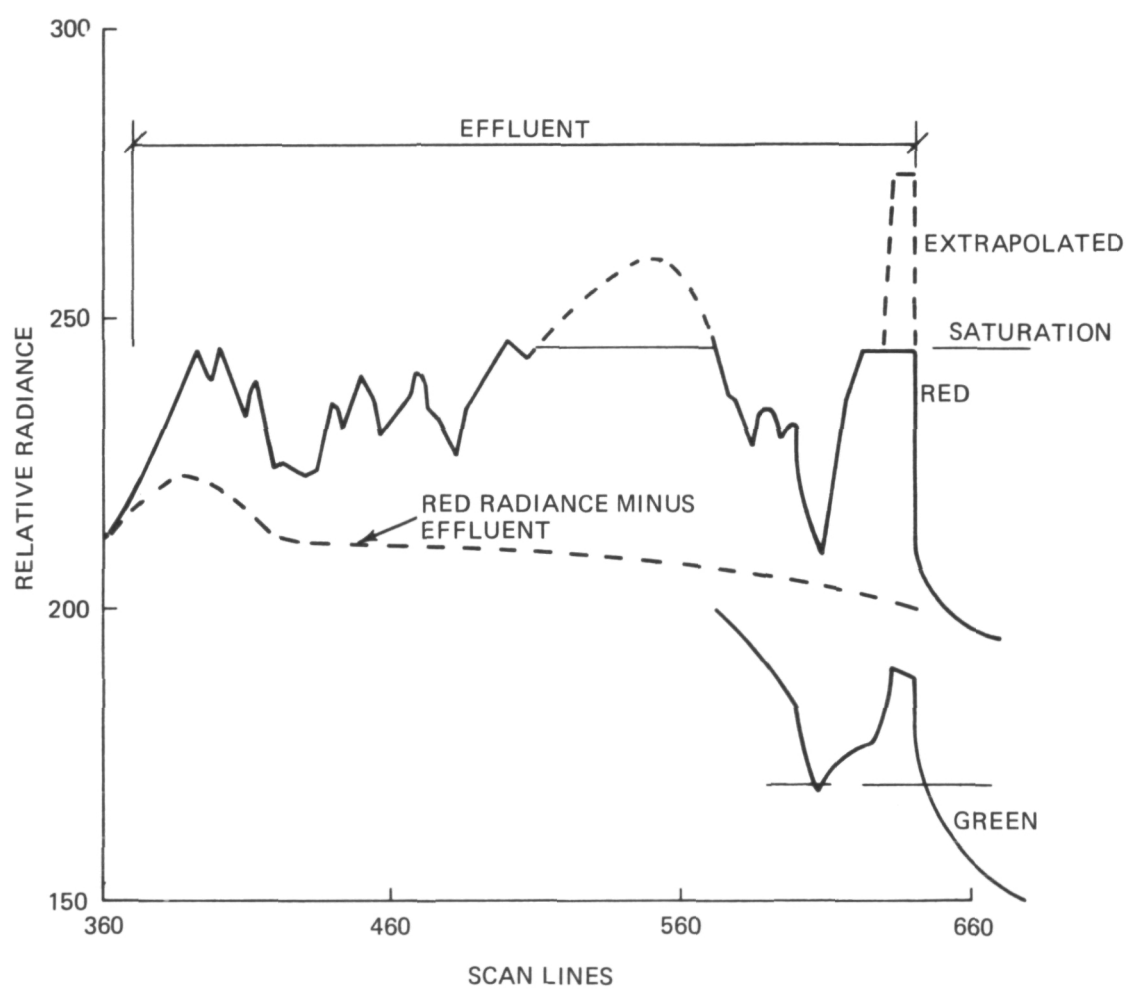
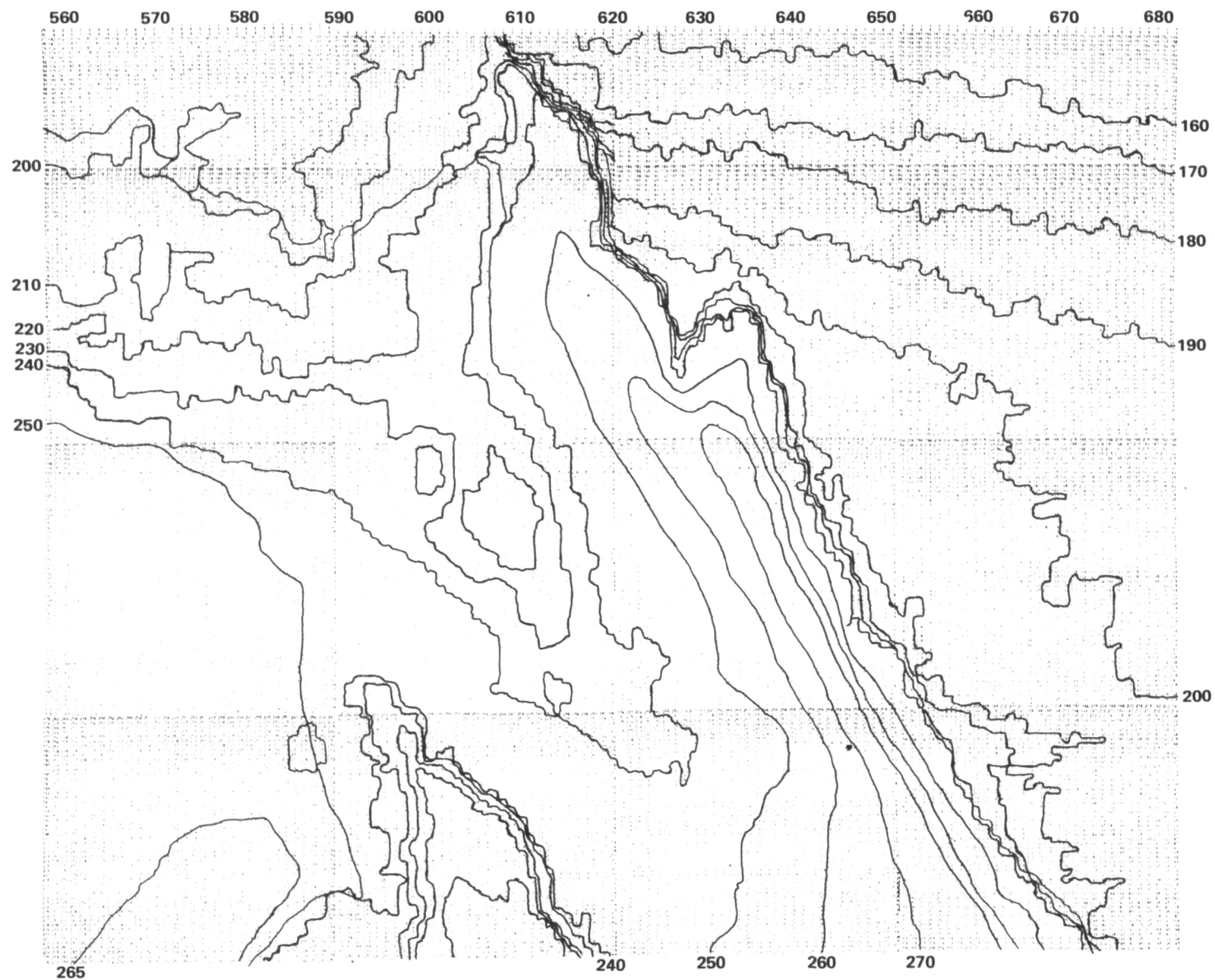Fig. 39 Extrapolation of Red Saturated Radiance Based on Green Unsaturated Radiance

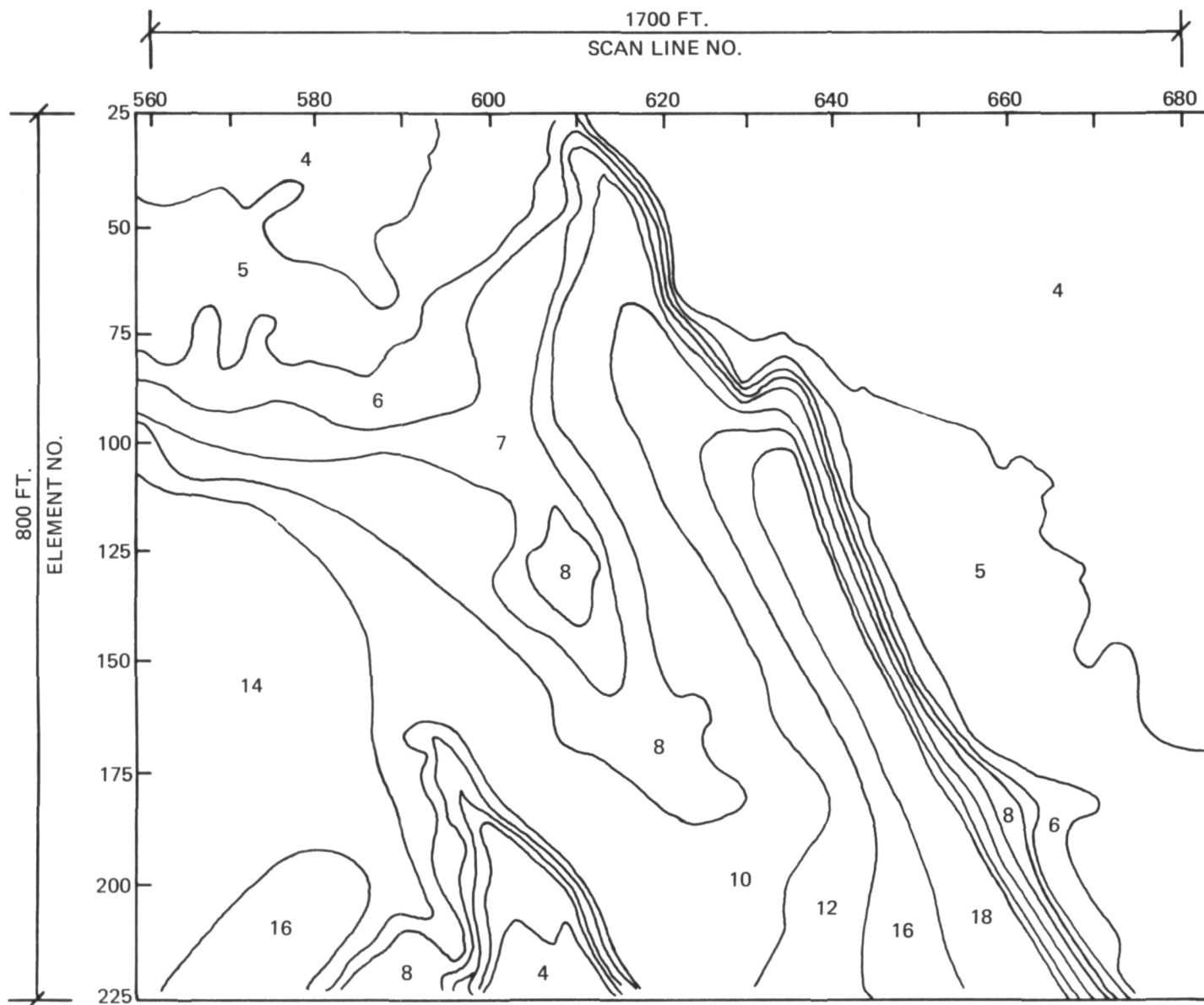Fig. 40 Radiance Contours in Binary Units in Prominent Part of Effluent

Fig. 41 Effluent Turbidity Contours in Jackson Units

The turbidity of the deeper water under these layers can be computed directly from equation (34) where the value of $(\alpha + \beta)_R$ has been calculated for the deeper water.

5. Summary of Results

The K_R and $(\alpha + \beta)_R$ parameters computed above are converted to Jackson Units (J.U.) according to Eqs. (34) and (41) and plotted in Figure 42 as surface and subsurface turbidity profiles along the survey path.

An inescapable conclusion that emerges from this analysis is that the waters of Boston Harbor in the area surveyed are quite turbid near the top (except for patches of "washed out" areas) and clear up towards the bottom reaching the clarity of typical coastal water. For example, President Roads (PR), the main harbor channel, where the water reaches a depth of 90 ft. is remarkably clear at the bottom probably due to the purging action of tidal currents. Where this action is impeded in shallow and enclosed areas, the turbidity is particularly high. The region between Rainsford Island (R) and S6 surrounded by islands and shoals (see Figure 30) is an example of this condition. In the very shallow areas the bottom is more turbid than the surface probably due to stirred-up sediments.

The analysis of K_R parameter reveals a high surface reflectance in the red which corroborates the high turbidity of the surface layer indicated independently by the trend of $(\alpha + \beta)$ values computed at various depths. The curve on the right side of Figure 42 illustrates this trend. Notice how the turbidity near the surface decreases from a value of 10 J.U. to 1 J.U. at a depth of 30 ft and below.

Within the effluent surface turbidity ranges from 18 J.U. near the source to 5 J.U. about one mile downstream in "West Gut" where samples were taken. Since the effluent was masking the bottom, sub-surface turbidity cannot be calculated from our data. However, judging from an analysis of the environs the water at 20 to 40 ft depth appears to be as clear as in President Roads.

The results of the laboratory analysis of water samples listed in Table II essentially corroborate our conclusions on the surface and sub-surface distribution of turbidity. For instance we agree with the ground truth data in the surprising fact that turbidity at Station 2 (where there are no visible effluent

plumes) is higher than at Station 3 located on the tail end of the effluent. This anomaly could be explained in terms of current action in West Gut (Station 3) and a stagnant condition around shoal S6 (Station 2). This shoal is on the path of effluents discharging from an outfall half a mile north. Also, notice in Figure 42 that both airborne and ground truth data exhibit a similar trend of increasing clarity with depth.
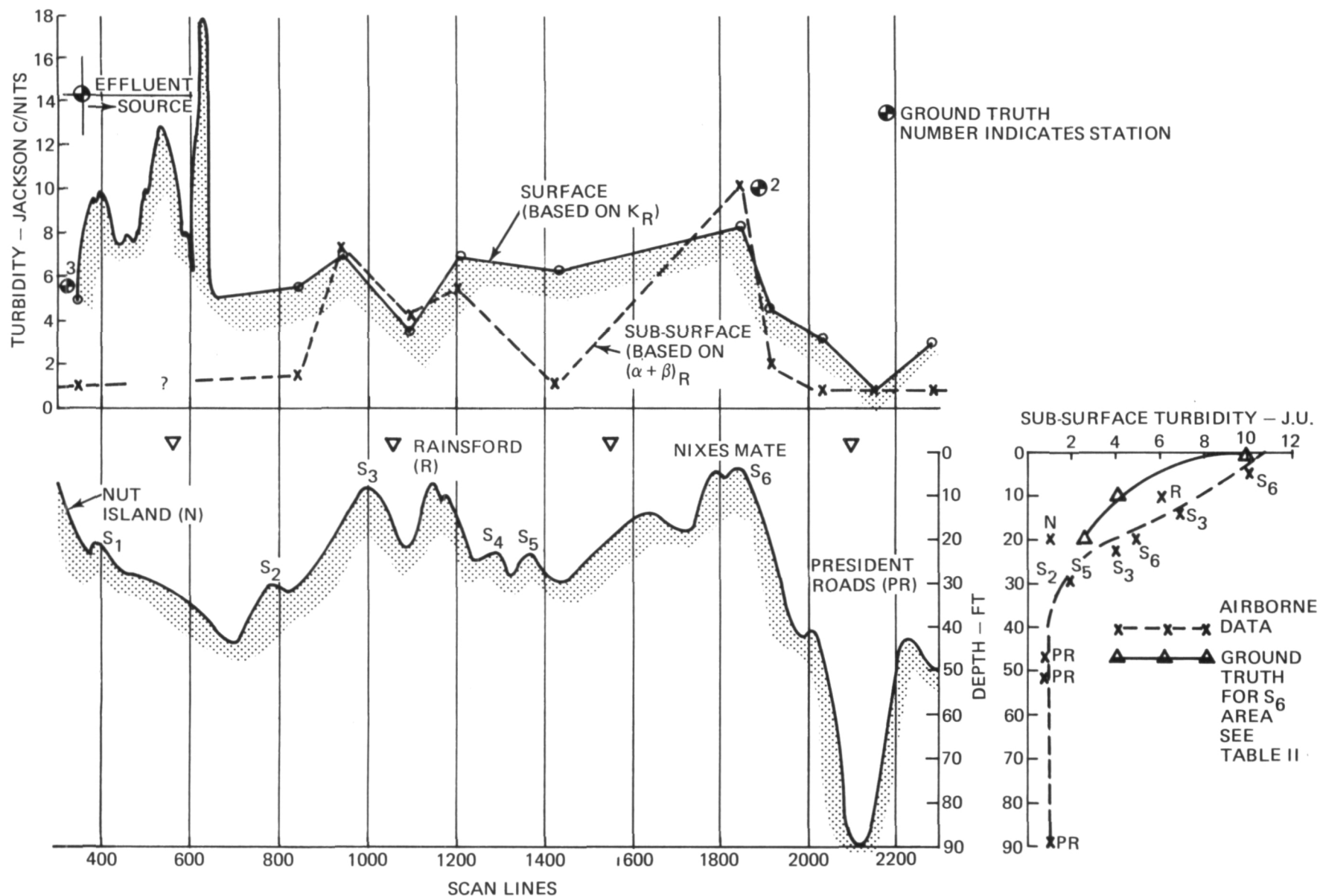
Fig. 42 Summary of Photometric Analysis of Boston Harbor

113

IIB. <u>POLARIMETRIC ANALYSIS OF LONG ISLAND SOUND</u>

<u>AND DERIVATION OF A TURBIDIMETRIC MAP</u>

On October 19, 1971, successive overflights of Long Island Sound from the Throgs Neck Bridge vicinity of the Bronx to Connecticut resulted in data summarized in Figure 43. The flight paths and filter data are shown in Figure 16 and Table I. For reasons previously explained it was elected to secure data in the red and far red. Again it should be mentioned that failure to choose exactly the same spectral bandpass in the DPM and its attached non-scanning head (NSH), made it impossible to extract valid central trace polarization from comparison of the measurements of the two heads. The spectral effects are too strong to permit concentration on polarization alone. Therefore, the polarimetric signature was extracted from successive DPM measurements.

Figure 43 shows the average of all the effective scanning steps measured across the DPM swath. Lateral spatial registration of the "V" and the "H" overflights was very good over most of the flight path. The exception was near the initiation of flight (Throgs Neck Bridge area).

Examination of the "H" and "V" radiance profiles in Fig. 43 shows the expected "concave-up" shape which is in small part due to the sensing of bottom signature at each end of the flight path. However, beyond 40 ft. depth the signature of the bottom in the red would be less than 3% of the total radiance while actual fluctuations in this depth range run to the order of 25%. It is believed, therefore, that most of the signature changes can be ascribed to changes in particulate content with the lowest values coinciding with the clearest water. This observation is commensurate with our deductions from Boston Harbor and other data in the red. The effect may be associated with particulates in buoyant layers.

Reduction of the overflight data to percent polarization results in the polarimetric profile also shown in Figure 43. Applying the methods associated with the use of equations (41) and (34) to these data a profile in terms of turbidity measured in Jackson Units is shown in Figure 43. Comparison of these data with typical water sampling data shown in Figure 44 for the area of Hempstead Harbor, L.I. Sound taken on the same day shows that the values are at least representative.

We introduce here the concept of the "polarimetric map" and the "polari-
metric picture" which we have presented at the Eighth International Symposium on
Remote Sensing of the Environment (17). To quote from our presentation: "A two-
dimensional matrix of numerical values of Stokes parameters, or of percent polar-
ization, arranged in map-like form to a definite scale, is defined as a polari-
metric map." Figure 45 is a polarimetric map of a portion of the DPM swath across
Long Island Sound in which the parameter is percent polarization.

By means of a digital tape-to-film conversion the numbers can be represented
by gray tones since the entire reduction is computerized and can, at any stage,
be read out. A gray tone rendition of this kind we call a polarimetric picture.
Pictorial data based upon percent polarization is shown for several portions of
the swath in Figure 46. We hold no brief for the linear fidelity of these
pictures at this time. They only show the possibilities. Technological status
is such that excellent presentation can be made.

A turbidimetric map prepared from, and superposed on a polarimetric map
in hand drawn contours is illustrated in Figure 45. This in turn could be
represented by a gray tone picture, if desired.

As can be seen from Figures 45 and 46 the polarimetric and turbidimetric
data appear to show a lot of detail. Actually, it is believed that most of
this detail is due to slight errors in spatial registration. Therefore, it is
the average gray level, not the spotty light and dark patches seen in Figure 46
which is probably significant. Again we stress that we are demonstrating poten-
tiality, not ultimate accuracy. It is assumed that data from a multichannel
DPM used as a polarimeter would look much more monotonous from over-water flights.
On the other hand, however there will be genuine anomalies which should be
picked up with good sensitivity.

The overall turbidity picture that emerges from this analysis is that the
waters of Long Island Sound in the area surveyed are most turbid near the New
York Shore; clear up considerably towards the middle of the Sound and then
turn slightly more turbid near the Connecticut shore. This variation is quanti-
tatively illustrated in Figure 45 in terms of Jackson Units and percent polar-
ization. In the pictorial rendition of percent polarization in Figure 46,
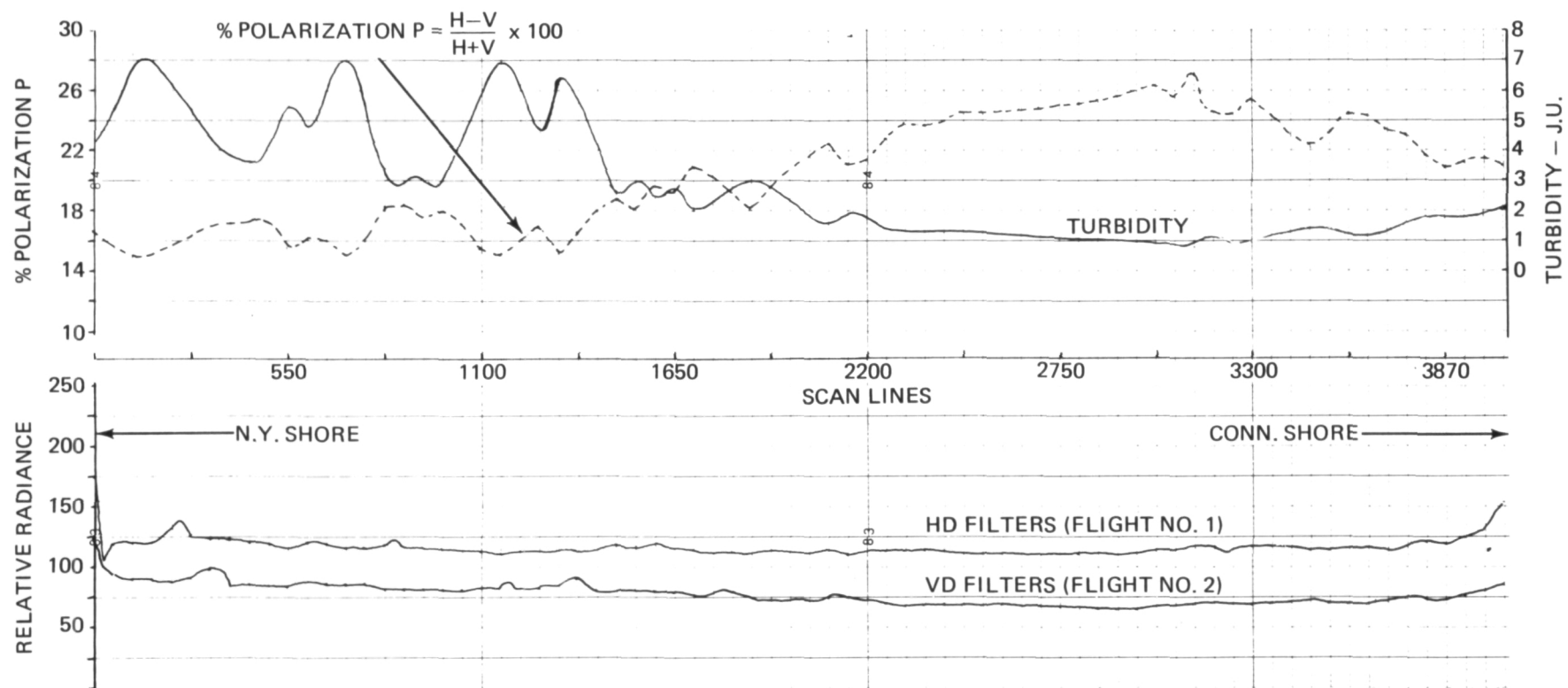darkening gray tones correspond to increasing levels of turbidity.

Fig. 43 Summary of Polarimetric Data of Long Island Sound and Computed Turbidity Profile, Site E
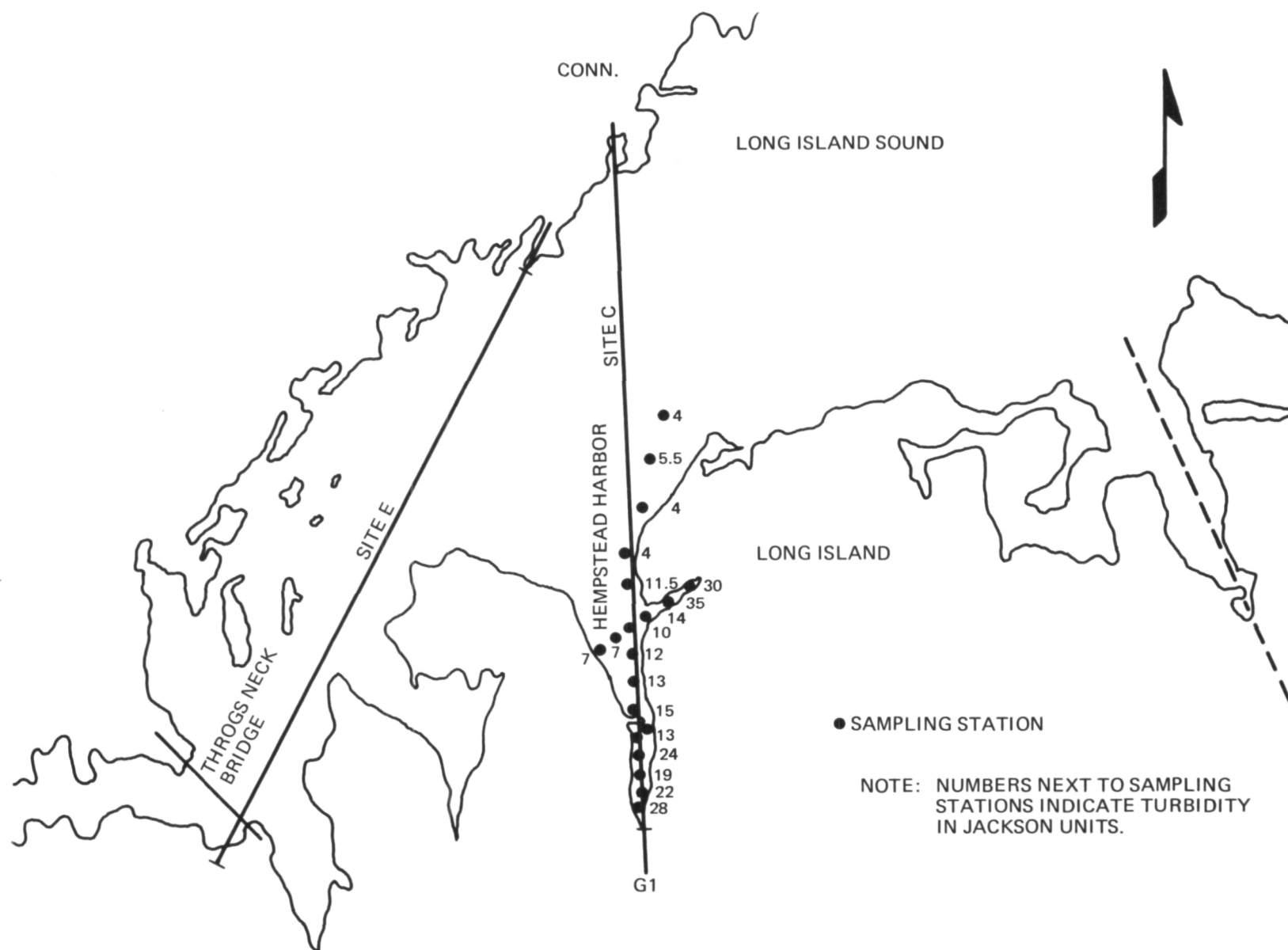
**Fig. 44 Turbidity of Hempstead Harbor, Oct. 19, 1971**

```
119 123 119 116 116 121 125 116 120 114 123 116 116 121
118 122 122 121 122 117 127 119 119 118 116 121 123 116
119 119 117 121 120 116 126 115 117 118 119 120 119 123
118 119 124 121 117 119 123 119 121 119 124 117 117 126
120 120 123 116 116 118 120 120 121 118 123 115 118 126
124 119 122 128 126 120 119 122 122 124 117 122 115 123
119 114 125 123 123 125 119 123 121 119 112 125 119 119
121 118 118 118 116 123 118 118 121 125 116 116 112 119
115 117 115 123 113 113 117 124 119 115 120 113 118 121
113 117 117 117 113 118 122 120 119 117 118 115 117 115
117 117 118 118 125 118 118 115 120 118 120 115 118 113
119 113 120 120 124 118 115 117 118 117 120 113 120 117
122 124 119 120 124 122 113 120 118 117 113 112 120 111
118 118 113 117 122 120 120 128 117 122 117 124 124 115
120 113 115 115 119 120 115 121 115 124 122 121 117 117
120 124 120 117 122 120 122 118 111 120 122 124 113 117
122 120 117 119 115 122 122 120 113 118 118 122 117 118
```

H — POLARIZATION (MEASURED)

```
76 79 75 74 75 76 86 79 79 80 79 77 79 75
75 78 73 76 79 76 76 77 99 74 93 78 76 77
73 78 74 78 75 85 76 76 117 75 133 75 75 80
84 79 74 78 75 77 76 80 77 82 103 73 73 80
84 72 78 75 77 77 78 83 74 93 79 75 82 80
76 73 72 79 76 74 76 87 77 86 75 76 74 79
73 70 73 76 78 76 73 89 77 73 73 78 76 78
78 76 75 75 71 72 73 78 71 75 75 73 73 75
77 76 78 75 71 72 77 80 71 75 75 75 71 73
73 76 71 77 76 76 81 74 90 77 81 75 75 73
78 76 75 80 76 76 83 74 90 82 78 73 77 78
74 71 80 73 76 78 82 74 92 79 78 75 73 73
73 76 78 78 74 75 81 71 77 78 75 80 78 76
75 73 84 73 76 73 71 76 78 80 72 77 71 71
77 74 80 78 71 71 78 73 75 76 71 80 71 71
77 77 80 75 76 73 75 73 75 76 77 77 73 73
71 77 75 71 71 77 75 71 73 75 78 78 71 77
```

V — POLARIZATION (MEASURED)

$$P = \frac{H - V}{H + V} \, 100$$
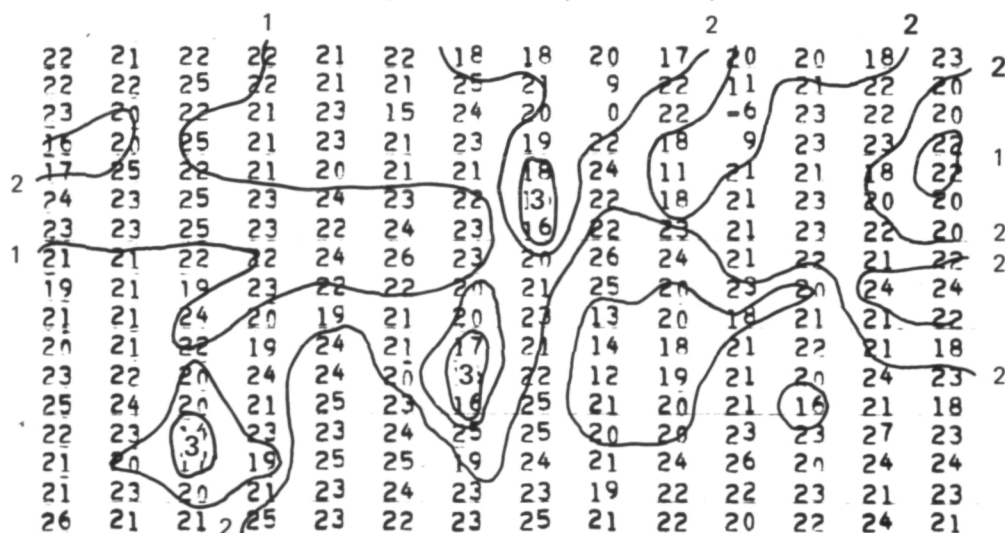
PERCENT POLARIZATION, P (COMPUTED) AND HAND DRAWN CONTOURS OF TURBIDITY IN JACKSON UNITS (J.U.)
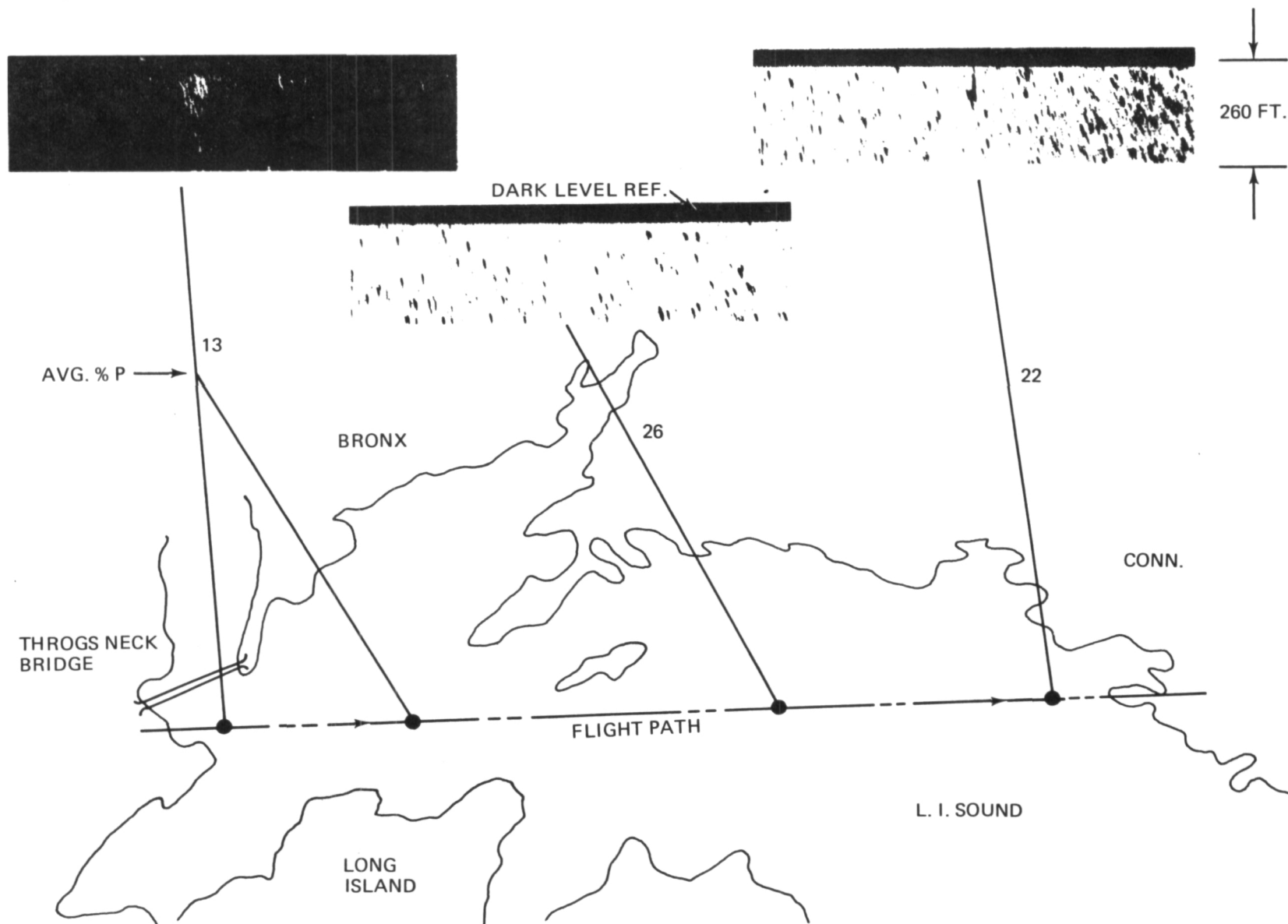
Fig. 45 Polarimetric Map of Long Island Sound Waters

Fig. 46 Tape-to-Film Converted Imagery of %P Values and their Variation Across Long Island Sound

PROBLEMS AND POTENTIAL SOLUTIONS IN PHOTOMETRIC REMOTE
MEASUREMENT OF WATER DEPTH AND TURBIDITY

The major problem in this technological area is the assessment of variable water parameters, particularly the attenuation coefficient, $(\alpha + \beta)$. An active method of depth measurement using the laser rangefinder has been suggested by several investigators. It appears that the active technique will work well in association with the passive methods such as have been reported in this study. The active method measures water depth by determining time lapse between pulsed signal return from the top of the water body and the bottom which is entirely independent of the degree of turbidity as long as the index of refraction is unaffected.

However, there are logistic problems with the active approach which can probably best be solved by limiting the active coverage to a single flight line trace of measured depth points and extrapolating to the sides to form a map by the passive approach using direct sunlight. In a sense the laser forms a means of calibrating the passively acquired data, making it possible to calculate the value of $(\alpha + \beta)$ from known values of d and measured radiance. This appears to be a very practical substitution of airborne remote sensing for ground control. The combination of an active system such as PLADS (8) and a multichannel DPM would appear to be of high potential.

It should be noted that some of the benefits of the passive system, such as multispectral sensing and polarimetric sensing cannot readily be achieved by the active system.

As far as merging the two capabilities is concerned it is suggested that the active system be provided with a digital output compatible with computer processing. Automation of mapping can be based on this commonality.

There are a number of problems with the present passive DPM, including inadequate dynamic range in the digital portion and inadequate sensitivity in the red. The first problem can be solved by proceeding to ten bit digital electronics; the second requires consideration of supplementary non-scanning photometers using the highly sensitive Ga As photomultiplier tubes. These non-scanning heads can acquire a central trace and possibly two side traces in the swath.

Of course we assume that the future combination of active and passive technology would involve a multichannel DPM, one capable of not only multispectral photometry, but also spectro-polarimetry.

A tabulation of PROBLEMS and SOLUTIONS is given as Table III. The common occurrence of LASER RANGING as a solution is to be noted.

TABLE III   PROBLEMS ASSOCIATED WITH CURRENT DPM SENSOR
AND POTENTIAL SOLUTIONS

Problems	Solutions
1. Accuracy of water clarity data	1a. Laser ranging 1b. Refinement of 2-color photometry
2. Changes in bottom reflectance	2. Laser ranging
3. Dynamic range	3. Ten bits (or more)
4. Surf and swells	4a. Short exposure 4b. Digital data processing 4c. Laser ranging
5. More turbid waters	5a. Laser ranging 5b. More S/N in red (e.g., GaAs photomultiplier tube)
6. Photogrammetric quality	6a. Laser ranging 6b. Gyro stabilization 6c. Precise navigation
7. Complex data processing	7a. Laser ranging 7b. Adequate software
8. Daylight limitation	8. Laser ranging

CONCLUSIONS

The objectives of this study are considered to have been met. Major results and conclusions include:

- A computer-generated numerical depth map of the waters off Fire Island Inlet, New York, superposed with a map of waves and swells. Depths down to 60 feet are shown. A depth sensing capability of one foot in about 35 feet of clear coastal water has been demonstrated. The airborne measurements agree closely with existing depth charts in the near-shore areas, but farther off shore they reveal a large topographic prominence at 30 ft. depth where existing charts indicate 50 ft. of water and a featureless bottom. The turbidity on the leeward side of the prominence is anomalously high. The wave pattern for the area suggests that the underwater prominence is damping large period swells approaching from the ocean. This action could conceivably account for the high turbidity revealed by two-color analysis.

- Quantitative profiles of surface and sub-surface turbidity of Boston Harbor including an effluent plume. It is found that the harbor water is generally quite turbid on top but clears up significantly towards the bottom. Ground truth measurements show a similar trend.

- A computer generated numerical map and tape-to-film converted picture of percent polarization of Long Island Sound. The numbers of gray tones in these displays correspond to levels of turbidity ranging from 1 to 8 Jackson Units. The results show higher levels of turbidity near the New York Shore (Throgs Neck Area) than the Connecticut Shore, the middle of the Sound being the least turbid.

To sum up, an airborne technique has been developed to map the bottom topography, surface roughness and sub-surface turbidity of coastal waters. The technique consists of precision measurements of optical signatures in digital form, arithmetic manipulation of the data and numerical, graphical, or pictorial display of the information. Theoretical models have been derived to relate relevant optical and physical properties of water and used as a guide in analyzing the inherently complex and subtle phenomena encountered in off-shore remote sensing.

Ultimately, the validity of the results depends upon the accuracy of the original data, close attention to details, and adequate computer software to do justice to the quantity and quality of data acquired by a DPM-type sensor.

RECOMMENDATIONS

We regard the present Digital Photometric Mapper as a means of exploring the remote sensing potential of very accurate photometry used in a geophysical mapping mode through use of the digital computer. It is our belief that we have demonstrated a strong potential for the diagnostic mapping of harbors and shallow coastal waters. Our recommendations deal firstly with the steps to be taken toward an eventual realization of the full benefits of this approach, not only for shallow water mapping, but for deeper water as well.

1. Refinement of the photometric and polarimetric models of water turbidity based upon reconciliation of theoretical models such as described by Plass, et al[10] with laboratory simulation and field data. For the field observations the use of the DPM with some improvements is recommended. The incorporation in these models of absorption and scattering parameters of chlorophyll-bearing particulates[14] and other substances of special interest should be considered.

2. Evaluation of the methods demonstrated in this report for the diagnosis of harbor water quality parameters by the bottom signature attenuation method. This involves the use of a previous fathometer survey for depth, or a concurrent depth measurement by laser rangefinder from the aircraft. It would appear that this approach is an economical substitute for a great quantity of water sampling for harbors and inland waters. Furthermore, the rate of coverage is good so that information could be updated frequently.

3. Evaluation of the methods demonstrated in this report for computerized water depth mapping. It is believed that there is a strong justification for frequent monitoring of certain portions of coastal shoreline where erosion and sedimentation are very dynamic. Here we refer to the purely passive approach which is now immediately available.

4.   The development of a combined DPM and laser rangefinder system for water depth mapping and also for the monitoring of water quality. The existing PLADS second harmonic Nd:YAG laser system can be flown in conjunction with our DPM to gain an operational feel for the feasibility. Of course a system combining improved models of both DPM and laser rangefinder should be developed if the program should materialize. The ultimate laser electronics should include range-gating to enable the best penetration of murky water, and also to furnish back-scatter information from successive layers in depth. It should be noted that comparison of reflected bottom signature with an accurate depth measurement furnishes a very direct way of measuring the water quality. While the laser system alone provides a nighttime capability, when used in daytime with a common digital interface the combination provides the capability of computerized mapping of a swath rather than a line trace. The laser capability and logistics do not have to be stretched to cover the whole swath.

5.   Whether in active, passive, or combination mode there is a common need for the development of computer programs for the smoothing out of surface roughness effects. Our experience seems to indicate that this approach is quite practical if the basic data are accurate. We initiated the development of such a program, but were unable to afford the completion of the effort.

6.   If the extraction of water depth and turbidity data from satellite systems is desired, the subject of atmospheric degradation of information is important. It would appear that if all inputs are accurately quantitative there is a good possibility of performing worthwhile observation from orbit. Meteor-ological data must be equally accurate to provide for the necessary computerized corrections. Investigations directed toward solving these problems and imple-menting computerized mapping are recommended.

7.   Specific investigation of the application of polarimetry to atmospheric monitoring appears to be in order. The application of a multichannel DPM to this task from orbit has been suggested previously by us. Preliminary studies includ-ing flight testing are recommended.

8.   While we have concentrated on water measurements in the present study
our previous recommendations in precise photometry and polarimetry of land areas
still hold true.[1]   There has been essentially no effort to capitalize on the
application of polarimetric mapping to land areas.[17]   We are certain that
strong advantages will be found for a combined polarimetric and multispectral
approach to generate thematic maps of high specificity for parameters such as
soil type, vegetation type, surface moisture, crop disease and wet land boundaries.
It is particularly important to register carefully the separate digital maps
taken in s-component and p-component for polarization maps. We can achieve this
registration with improved horizontal control using the present DPM. By under-
taking terrain polarimetry in this way by successive overflights we feel we can
strengthen the case for the ultimate development, - that of the multichannel
DPM. The use of several concurrent channels would eliminate registration diffi-
culties. As pointed out in Ref (17) other potential applications for precision
polarimetric mapping include oil slick detection and mapping.

REFERENCES

1. Halajian, J. and Hallock, H. B., "Digital Photometric and Polarimetric Surveys of Water and Land Areas," Grumman Advanced Development Report ADR 03-02-71-1, August, 1971.

2. Hallock, H. B., Halajian, J., and Skeels, S. "A Digital Electro-Optical Photometric Mapper," JOSA Vol. 60, No. 5, Paper FE 15, 1970.

3. U.S. Department of Commerce, NOAA, National Ocean Survey, Office of Marine Survey and Maps, "Photographic and Thermal Remote Sensing Survey of Boston Harbor Surface Currents," October, 1971.

4. Moore, J. Grange, "The Determination of the Depths and Extinction Coefficients of Shallow Water by Air Photography Using Colour Filters," Transaction of the Royal Philos. Soc., January 1947, Vol. 240.

5. Brown, W. L., Polcyn, F. C., and Stewart, S. R., "A Method for Calculating Water Depth, Attenuation Coefficients and Bottom Reflectance Characteristics" Proc. of the Seventh International Symposium on The Remote Sensing of the Environment, May, 1971.

6. Polcyn, F. C., Brown, W. L. and Settinger, I. J., "The Measurement of Water Depth by Remote Sensing Techniques," University of Michigan, Inst. of Science and Technology, Report 8973-26-F, October, 1970.

7. Hickman, G. D. and Hogg, J. E., "Application of An Airborne Pulsed Laser for Near Shore Bathymetric Measurements," Proc. of the Sixth International Symposium on Remote Sensing of the Environment, 1969.

8. Naval Oceanographic Office Technical Note 6620-102-72, Test Report on PLADS (Pulsed Light Airborne Depth Sounder) - 1972.

9. Piech, K. R., Silvestro, F. B. and Gray, R. J., "Industrial Effluent Diffusion in Rivers: A New Approach to Theory and Measurement," 15th Annual Technology Meeting, Inst. of Environmental Sciences, April, 1969.

10. Plass, G. N. and Kattawar, A. W., "Radiative Transfer in the Earth's Atmosphere-Ocean System, Paper TuI 11, OSA Spring Meeting, 1972.

11. Feinstein, D. L., and Piech, K. R., "A Light Transport Problem in Water Pollution," 16th Annual Technical Meeting Inst. of Environmental Sciences, April, 1970.

12. Granatstein, V. L., Rhinewine, M., Levine, A. M., Feinstein, D. L., Mazurowski, M. J. and Piech, K. R., "Multiple Scattering of Laser Light From a Turbid Medium," Applied Optics, Vol. 11, no. 5.

13. Silvestro, Frank B., "Quantitative Remote Sensing on Water Pollution," 15th Annual Technical Mfg., Inst. of Environment Science, April, 1969.

14. Clarke, G. L., Ewing, G. C. and Lorenzen, C. J., "Spectra of Backscattered Light from the Sea Obtained from Aircraft as a Measure of Chlorophyll Concentration," Science, 20 February 1970.

15. Herman, B. M., Browning, S. R. and Guiran, R., "The Effect of Atmospheric Aerosols on Scattered Sunlight," J. Atmospheric Sciences, Vol. 28, 1971.

16. Hallock, H. B. and Grusauskas, J., "The Polarimetric Signature of Natural Water Surfaces," JOSA Vol. 57, No. 4, Paper No. FE 12, 1968.

17. Halajian, J. and Hallock, H. B., "Principles and Techniques of Polarimetric Mapping," Eighth International Symposium on Remote Sensing of the Environment, University of Michigan, 1972.

18. "Standard Methods," American Waterworks Ass., Federation of Water Pollution Control and U.S. Public Health Service, 13th Edition, 1971.

19. James, H. R., and Birge, E. A., Trans. Wis. Acad. Sci. Arts Lett. V. 31, 1-154, 1938.

APPENDIX A

MODEL FOR THE SPECTRAL VARIATION

OF EXTINCTION COEFFICIENT OF NATURAL

WATERS

The extinction coefficient (or the volume attenuation coefficient) of natural waters depends in an intricate way on the amount and kind of particulate matter which is present. For the most accurate analysis of these natural waters physical models based upon actual measurements should be used, taking into account the nature of the most likely particulate types in the contamination of each local area. However, these data do not exist. The worldwide trends can be approximated by models used with reasonable success in the past. We have elected to use a model developed by J. Grange Moore (4), not because it is necessarily the best available, but because it is convenient and based upon a pragmatic philosophy. The principal underlying assumption is that the absorption component, the coefficient which we have designated to be α, is that of distilled water; and that the scattering coefficient (β) is due solely to Mie-type scattering by particles of the order of magnitude of the light wavelength. Thus molecular scattering, which follows the Rayleigh law, is ignored.

Molecular scattering cannot be ignored for many aspects of water analysis including the multispectral approach to the analysis of turbidity (10). However, for the analysis of effluent data in the red-green and for practical aspects of water depth-mapping we have adopted this model which ignores the molecular scattering.

The lower curve in Figure 6 extracted from Moore (4) shows his assumed spectral absorption coefficient which follows James and Birge (19). In order to compute the extinction coefficient beginning with these values, a value of β is assumed at a definite wavelength corresponding to a certain "class" of transparency. For this specific "class" of transparency the values of β at other wavelengths are obtained by means of the assumption that the scattering coefficient varies inversely as the first power of the wavelength. By the assumption of various "classes" corresponding to an arbitrarily chosen set of values of β, and adding these β - values to the α - values of distilled water a series of spectral extinction functions for the arbitrary "classes" can be generated as shown in Figure 6. It can be presumed that we would modify this model for further, more intensive analytical effort.

APPENDIX B

WATER TURBIDITY AND COLOR:

DEFINITION AND LABORATORY MEASUREMENTS

Turbidity is an expression of an optical property of the fine suspended matter in water which causes light to be scattered and absorbed. Because the size, shape and refractive index of the suspended particles are optically important, it is not practical to correlate turbidity with the weight concentration of the particles. The standard instrument used to measure turbidity is the Jackson candle turbidimeter which uses an arbitrary standard consisting of a silica of certain particle size suspended in distilled water such that one mg of the silica in one liter of water corresponds to one unit of turbidity commonly referred to as a Jackson Unit. The candle turbidimeter consists of a calibrated glass tube containing the standard suspension and a standard candle. The light path through the suspension which just causes the image of the flame to disappear when the flame is viewed through the suspension forms the basis of turbidity measurements (the longer the light path, the lower the turbidity). Today all instruments are copies of the original Jackson candle turbidimeter and the natural suspensions they measure are calibrated in conformity with the original data obtained with the Jackson candle turbidimeter (see Table 21 of "Standard Methods" Ref (18).

In this study the turbidity of the samples obtained in Boston Harbor were measured by a Bausch and Lomb Spectronic 20 turbidimeter. The procedure consisted of measuring the transmission of light through a one inch thick tube containing the sample and then converting the transmission values into Jackson Units by means of previously prepared turbidity standards which had been calibrated against a candle turbidimeter. These measurements are listed in Table II and the location of the samples are shown on the map of Boston Harbor in Fig. 29.

Similar methods of light transmission measurements were used in analyzing the water samples for color. The particulates were first removed by centrifuging the samples at 10,000 rpm for half an hour and the transmission of light was measured at .350 μm wavelength. The readings were then converted into "Chloroplatinate Units" by comparison with standard solutions. The standards

consist of 1.246 g of K_2 Pt Cl_6 and 1g of $CoCl_2$ dissolved in distilled water containing 100 ml concentrated HCl and diluted to 1000 ml with distilled water. This solution bears .5 g Pt and .25 g Co and has a color value of 500 CPU.

Color measurements of water samples from which the turbidity has been removed represent "true color" that is due to dissolved organic matter. "Apparent color" is due to both absorption by the dissolved substances and scattering by the particulates, and is correlated with the $(\alpha + \beta)$ parameter derived from the field data. Correlation of laboratory measurements of "true color" with field data would require a multispectral analysis of these data. We have such data in the blue and the green but have not had the opportunity to analyze them.

APPENDIX C

ANALYSIS OF PHOTOMETRIC SENSITIVITY

TO CHANGES IN WATER DEPTH

The purpose of this section is to analyze the capability of an optical instrument to sense a change in depth as a function of depth based on the attenuation of light in water and the photometric sensitivity of the instrument. The analysis is then applied to estimate the depth sensing capability of the DPM based on its present photometric sensitivity of 1%. Further improvement in depth resolution is also discussed based on higher photometric accuracy that is currently possible to achieve.

Let G_o and G_d be the radiance reaching the sensor from depth zero (shoreline) and depth d. According to equation (23) and terms previously defined

$$\log_e (G_d - K_g) = \log_e (G_o K_g) - 2f (\alpha + \beta)_m d \qquad (23)$$

This equation is expressed in terms of $\log_e$ for convenience in the analysis that follows. Also, the attenuation coefficient $(\alpha + \beta)$ is expressed in units of $\log_e$ per meter. The conversion from one unit to the other is made according to the expression.

$$(\alpha + \beta)_m = \frac{(\alpha + \beta)_f}{.132}$$

Differentiating Eq. (23) we get the rate of change of radiance with depth

$$\frac{1}{G_d - K_g} \cdot \frac{\Delta G_d}{\Delta d} = - 2 (\alpha + \beta)_m$$

For clear coastal water where $(\alpha + \beta)_m = .151 \ m^{-1} \log_e$

$$\frac{\Delta G_d}{\Delta d} = - .302 (G_d - K_g) \qquad (44)$$

At a depth of, say, 15 meters sunlight will be attenuated by a factor of

$$e^{-.302 \ x \ 15} = 10^{-2}$$

Let I_o be the irradiance of sunlight at sea level and 3×10^{-2} and 12×10^{-2} be the reflectance of the water surface and submerged sand respectively. Then

$$G_o = I_o (3 \times 10^{-2} + 12 \times 10^{-2}) = 15 \times 10^{-2} I_o$$

At 15 meters depth:

$$G_d = I_o \left[3 \times 10^{-2} + (12 \times 10^{-2} \times 10^{-2}) \right] = 312 \times 10^{-4} I_o$$

Let R_d be the photometric resolution at depth d.
At 1% photometric sensitivity, the DPM will resolve

$$R_d = 10^{-2} \; 312 \times 10^{-4} I_o = 3.12 \times 10^{-4} I_o$$

at 15 meters depth. The contribution of the bottom at this depth is

$$G_d - K_g = (312 \times 10^{-4} - 300 \times 10^{-4}) I_o = 12 \times 10^{-4} I_o \quad (45)$$

Combining Eqs. (44) and (45) and assuming application to a finite increment, ΔG_d, we find that a change in depth of one meter at 15 meters depths corresponds to an attenuation in radiance of

$$\Delta G_d = -.302 \times 12 \times 10^{-4} I_o = 3.6 \times 10^{-4} I_o$$

Since $\Delta G_d > R_d$ it is concluded that the DPM has adequate capability to detect a depth change of less than a meter at 15 meters depth.

Using the above assumptions and equations it is possible to construct graphical relationships between the least increment of depth which can be sensed and the depth. This has been done in Fig. 35 for the green spectral band centered at 5300A and clear coastal water. A separate curve may be drawn for each photometric accuracy assumption. As shown in Fig. 35 we believe that 1 percent is a fair representation of our present capability and that .3 percent is an achievable goal for a scanning DPM. Even better photometric accuracies may be predicted for non-scanning photometric heads of somewhat coarser resolution. These higher accuracies are worthwhile for relatively calm water conditions such as inland bodies of water.

The analysis can be extended into the red and far red. The reflectance of the water decreases and that of the wet sand bottom increases. These factors are favorable. However, the attenuation of the water becomes rapidly more severe as the spectral band shifts toward the far red. The analysis has been extended to the red (R) band centered at 6250A and a far red (FR) band centered at 6800A. The following assumptions as to basic reflectances have been made.

<div align="center">

6250A and 6800A

</div>

water reflectance	$.7 \times 10^{-2}$
wet sand bottom reflectance	15×10^{-2}

The results of the analysis using attenuation coeffients from the model described in Appendix A are shown in Fig. 36 applying to the "R" band and Fig. 37 applying to the "FR" band. The assumed volume attenuation coefficient at 6250A is $.34 \log_e m^{-1}$ and at 6800A, $.63 \log_e m^{-1}$.

It is again emphasized that "sensitivity" as analyzed here is not equivalent to accuracy. Sensitivity becomes accuracy only when methods of calibration based upon accurate water characteristics are used. These methods can be developed.

APPENDIX D

SPECTRAL INTEGRATION EFFECTS

In making a determination of the effective attenuation coefficient of
water over a spectral pass band of appreciable width it is necessary to perform
integration of several functions of wavelength. These functions include the
sunlight irradiance function $H_s(\lambda)$, the water transmission function $T_w(\lambda)$, the
spectral response of the broadband optical detector (and optics,) $S(\lambda)$, and the
spectral filter functions, such as $D(\lambda)$ for our DPM read (R) band.

The function $H_s(\lambda)$ varies with solar and atmospheric conditions, but may
be represented by Figure D-2 showing data for Air Mass 1 (sunlight vertically
through one atmosphere thickness) extracted from the Air Force Geophysics
Handbook. The data shown for water of various grades of clarity can be con-
verted to a function $T_w(\lambda)$ for any one specific depth of water, d, by use of
the equation,

$$T_w(\lambda) = 10^{-(\alpha + \beta)_\lambda d}$$

The spectral response of the DPM and that of its associated non-scanning
photometric head is S-20, shown illustrated in Figure D-1. Also shown in
Figure D-1 is the spectral filter transmission function for the green (G) data
of the report which is that of a Kodak Wratten 61. The red portion of the
Wratten 61 band is of very little consequence because of the low S-20 response
between 7500 and 8000 A.

Special green (Gr_1) and blue (Bl) filters designed for chlorophyll sensing
(see Figure 12) were used with the DPM. Although we have data in these bands
time has not permitted the reduction of the data. The only green data
reported herein are taken with the Wratten 61 (Gr_2) as shown.

Shown also in Figure D-1 is the effective response of the S-20 detector
looking through the Wratten 61 filter. The product $H_s(\lambda) Gr_2(\lambda)$ is identified
in Figure D-2 as the "effective response" of the system. The shape of this
response is what is important, not the scale which is purely relative in
ordinate.

Figure D-2 illustrates the method used for determining the effective
$(\alpha + \beta)$ values for the system in particular spectral pass bands. Following
through on the "effective response" with the Wratten 61 filter as shown in
Figure D-1 this relative response is normalized at its peak and multiplied by
the solar irradiance function $H_s(\lambda)$ as shown in Figure 49 and the product
$H_s(\lambda) \, S(\lambda) \, Gr_2(\lambda)$ is shown. Figure D-2 also depicts the spectral transmission
function $T_w(\lambda)$ of 10 ft of clear coastal water derived from the data of
Figure 6. Finally, the product $H_s(\lambda) \, S(\lambda) \, Gr_2(\lambda) \, T_w(\lambda)$ is illustrated. All
these products are plotted through the entire pass band which may be said to
be contained within the upper limit λ_2 and the lower limit λ_1.

$$\text{The ratio } \frac{\int_{\lambda_1}^{\lambda_2} H_s(\lambda) \, S(\lambda) \, Gr_2(\lambda) \, d\lambda}{\int_{\lambda_1}^{\lambda_2} H_s(\lambda) \, S(\lambda) \, Gr_2(\lambda) \, T_w(\lambda) \, d\lambda}$$

is the effective attenuation of the 10 ft of water for the detector system
over the spectral band. This ratio is determined to be .64. This value can
be converted to an effective value of $(\alpha + \beta)_G$ by means of the relationship,

$$.64 = 10^{-(\alpha + \beta)_G \times 10}$$

$$\text{or } (\alpha + \beta)_G = .019$$

In a similar manner the product $H_s(\lambda) \, S(\lambda) \, D(\lambda)$, which represents our
red (R) data, is computed and normalized at its peak to the solar irradiance
function $H_s(\lambda)$. As shown in Figure D-2 the product is multiplied also by the
water transmission function $T_w(\lambda)$. The integral of the final product is shown
to be peaked very sharply at the lower end of the pass band which is designated
λ_3. This peak becomes increasingly narrowed and the effective band reduced in
width as the depth of water increases. Due to the rapid loss in transmission
of water of the longer wavelengths the spectral band eventually becomes a
narrow spike near 6000 A. The effective $(\alpha + \beta)_R$ value thus becomes less for
deep water than for shallow water as has been noted in the study. The effect
is much less pronounced for the green (G) values. It is quite necessary to use
curves computed for pertinent depth ranges in the red as indicated in Figures
7 and 8.

Specifically in the data for 10 ft depth,

$$\frac{\int H_s(\lambda)\ S(\lambda)\ D(\lambda)\ d\lambda}{\int H_s(\lambda)\ S(\lambda)\ D(\lambda)\ T_w(\lambda)\ d\lambda} = .28$$

$$.28 = 10^{-(\alpha + \beta)_R \times 10}$$

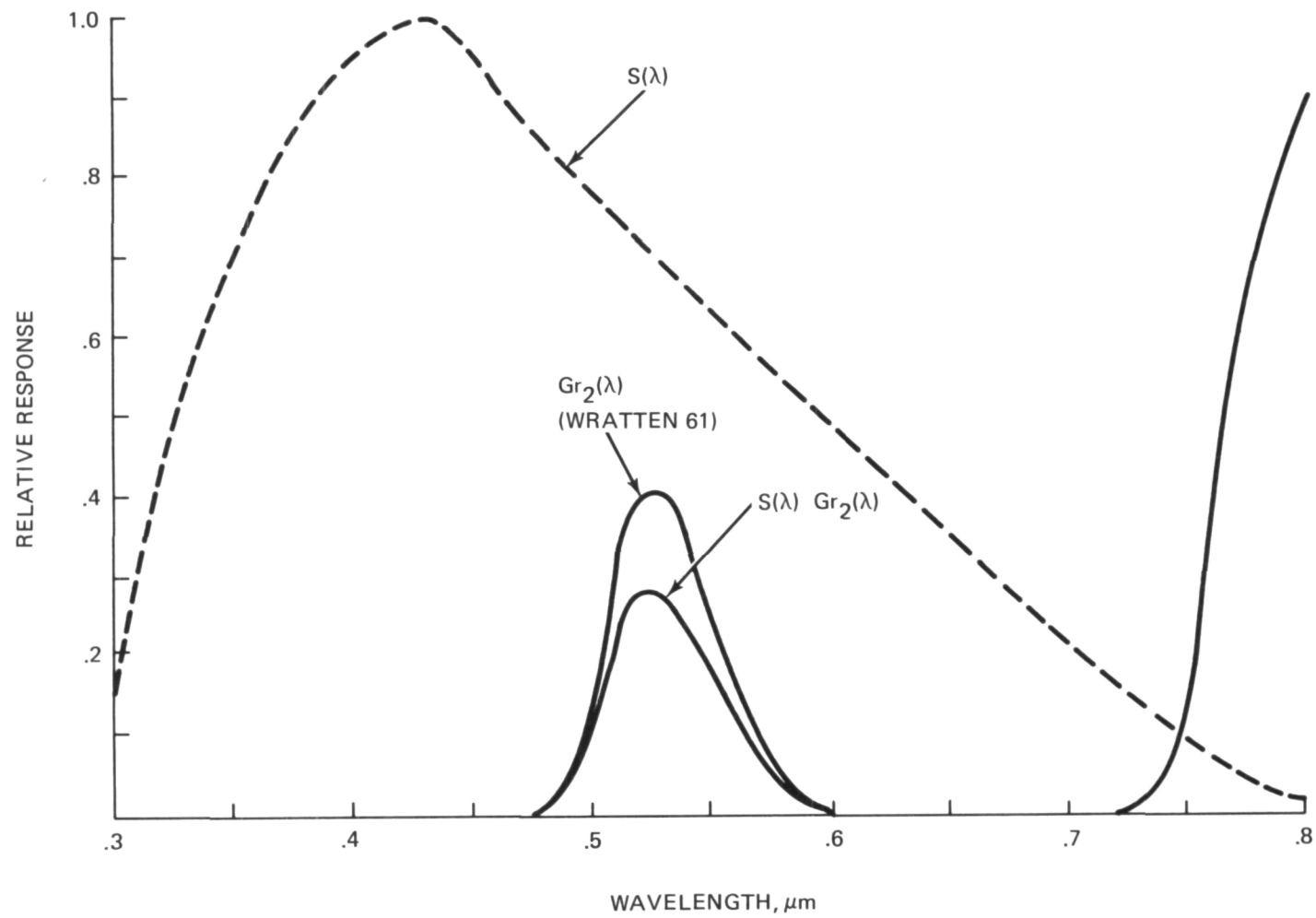$$\text{or } (\alpha + \beta)_R = .052$$
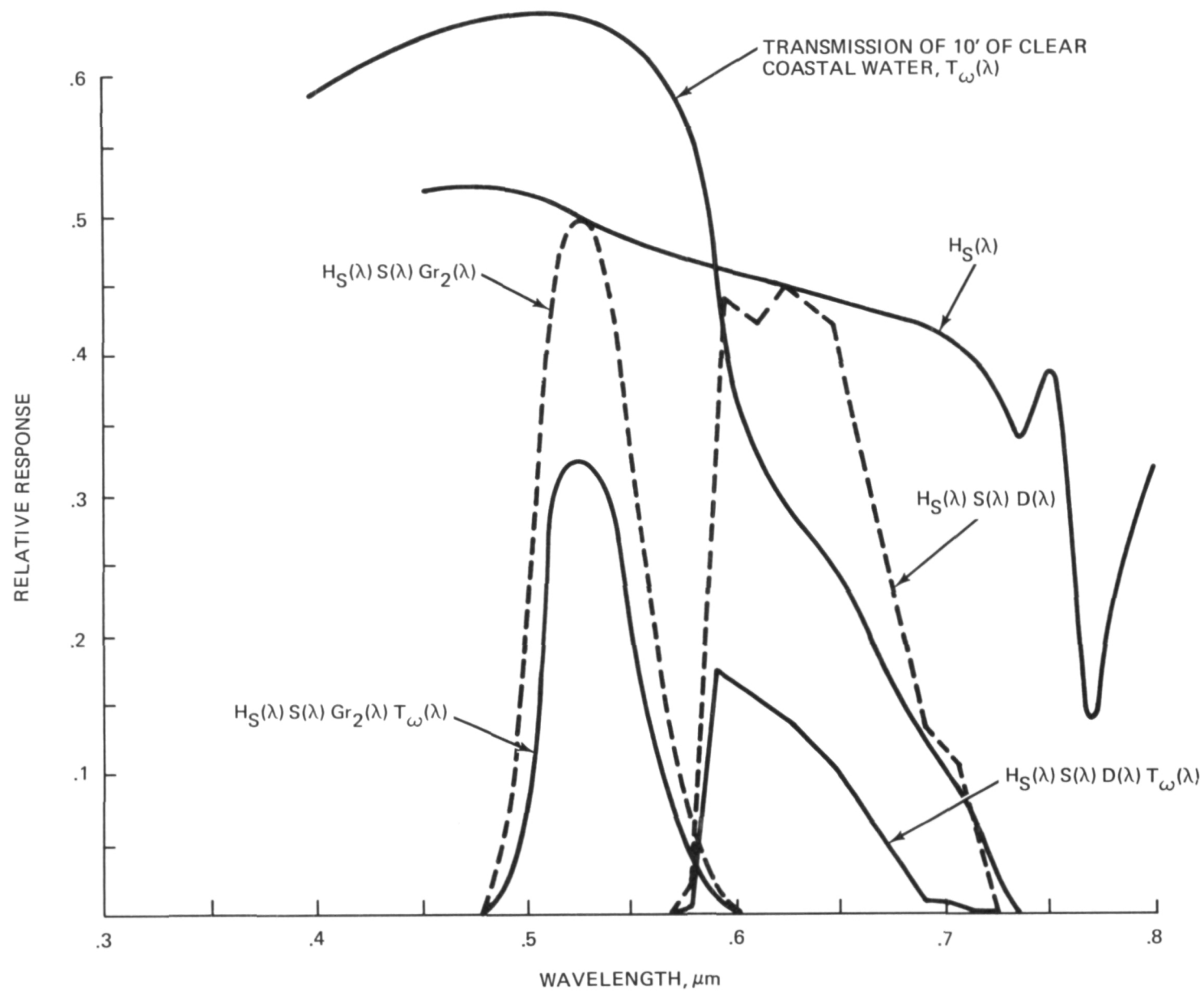
Fig. D-1 Non-Scanning Head Spectral Response with Wratten 61 Filter

Fig. D-2 Effective $(\alpha + \beta)$ for Clear Coastal Water